

BINARY NEUTRON STARS WITH ARBITRARY SPINS  
IN NUMERICAL RELATIVITY

by

Nicholas A. Tacik

A thesis submitted in conformity with the requirements  
for the degree of Doctor of Philosophy  
Graduate Department of Astronomy & Astrophysics  
University of Toronto

Copyright © 2016 by Nicholas A. Tacik

# Abstract

Binary Neutron Stars with Arbitrary Spins  
in Numerical Relativity

Nicholas A. Tacik

Doctor of Philosophy

Graduate Department of Astronomy & Astrophysics

University of Toronto

2016

We discuss spinning binary neutron stars in numerical relativity. Write a good abstract when done everything else.

# Dedication

Dedicated to lots of good people. Write a proper dedication.

“Something inspiringsg.”

Someone inspiring

# Acknowledgements

Thanks to my friends and family.

# Contents

<b>1</b>	<b>Introduction</b>	<b>1</b>
1.1	Timeline . . . . .	1
1.2	Thesis TDL . . . . .	1
1.3	Introduction . . . . .	2
1.4	The two-body problem in General Relativity . . . . .	6
1.5	The initial value problem in Numerical Relativity . . . . .	11
1.6	Binary Neutron Star Systems . . . . .	15
<b>2</b>	<b>Binary Neutron Stars with Arbitrary Spins in Numerical Relativity</b>	<b>21</b>
2.1	Chapter Overview . . . . .	21
2.2	Introduction . . . . .	22
2.3	Methodology . . . . .	25
2.3.1	Formalism for irrotational binaries . . . . .	25
2.3.2	Formalism for Spinning Binaries . . . . .	31
2.3.3	Solving the elliptic equations . . . . .	33
2.3.4	Construction of quasi-equilibrium initial data . . . . .	35
2.3.5	Quasi-Local Angular Momentum . . . . .	37
2.4	Initial Data Results . . . . .	39
2.4.1	Convergence of the Iterative Procedure . . . . .	39
2.4.2	Convergence of the Solution . . . . .	40
2.4.3	Convergence of the quasi-local spin . . . . .	45

2.4.4	Quasi-local Spin . . . . .	49
2.5	Evolution Results . . . . .	52
2.5.1	Evolution Code . . . . .	53
2.5.2	Eccentricity Removal . . . . .	56
2.5.3	Aligned spin BNS evolutions: NS Spin . . . . .	60
2.5.4	Precession . . . . .	66
2.5.5	Stellar Oscillations . . . . .	71
2.6	Discussion . . . . .	76
<b>3</b>	<b>Initial Data for Spinning Neutron Stars in Mixed Binaries</b>	<b>78</b>
3.1	Introduction . . . . .	78
3.2	Initial Data Formalism . . . . .	80
3.3	Numerical Methods . . . . .	86
3.4	Results . . . . .	91
3.4.1	Initial Data Set Parameters . . . . .	91
3.4.2	Convergence of the Initial Data Solver . . . . .	94
3.4.3	Other Initial Data Sequences . . . . .	101
3.5	Conclusion . . . . .	111
<b>4</b>	<b>Junk Radiation in Binary Black Hole Simulations</b>	<b>113</b>
4.1	Chapter Overview . . . . .	113
4.2	Chapter TDL . . . . .	113
4.3	Introduction . . . . .	114
4.4	Numerical Methods . . . . .	118
4.4.1	The Initial Value Problem . . . . .	118
4.4.2	Code . . . . .	119
4.4.3	Eccentricity Reduction . . . . .	120
4.4.4	Simulations . . . . .	121
4.5	Methodology . . . . .	121

4.5.1	Pulse in the Gravitational Waveform . . . . .	122
4.5.2	Uncertainty in $E_J$ . . . . .	126
4.5.3	Transient behaviour in Black Hole quantities . . . . .	130
4.6	Results . . . . .	135
4.6.1	Energy in Junk Radiation . . . . .	135
4.6.2	Mass Increase . . . . .	141
4.6.3	Spin Decrease . . . . .	142
4.7	Summary . . . . .	146
<b>5</b>	<b>Conclusions &amp; Future Work</b>	<b>147</b>
5.1	Conclusions . . . . .	147
5.2	Future Work and Directions . . . . .	147
	<b>Bibliography</b>	<b>148</b>

# List of Tables

1.1	The properties of known double neutron star systems . . . . .	5
2.1	Parameters for the initial data sets used in test the initial data solver. . .	40
2.2	Detailed information about our three evolutions. . . . .	53
2.3	Eccentricity removal data for our three main runs. . . . .	59
3.1	Initial data set parameters for series of 36 Bh-Ns initial data sets. . . . .	93



# List of Figures

1.1	Effect of $+$ and $\times$ polarized gravitational waves on a ring of particles. . .	8
1.2	<b>add caption</b> . . . . .	11
1.3	Evolutionary scenarios of a typical high-mass binary. . . . .	17
1.4	Comparison of iso-density contours of an equal mass system and a non- equal mass system. . . . .	20
2.1	Visualization of the initial data domain decomposition. . . . .	34
2.2	Iterative convergence of the Euler constant. . . . .	41
2.3	Convergence of the Hamiltonian and Momentum constraints. . . . .	43
2.4	Convergence of the location of the stellar surface. . . . .	44
2.5	Convergence of ADM-energy and of the ADM-angular momentum magni- tude. . . . .	46
2.6	Convergence of the quasi-local spin computation. . . . .	47
2.7	Stellar cross-section for a series of different spins. . . . .	48
2.8	Dimensionless angular momentum as a function of $\Omega$ . . . . .	50
2.9	Dimensionless spin measured as measured on different coordinate spheres. . . . .	52
2.10	Binary separation as a function of time. . . . .	57
2.11	The derivative of the binary orbital frequency at different levels of eccen- tricity reduction. . . . .	58
2.12	Convergence of the derivative of the binary orbital frequency. . . . .	61
2.13	The spin measured on multiple coordinate spheres for the <b>S.4z</b> run. . . . .	62

2.14	Neutron star spin during the two aligned-spin evolutions. . . . .	64
2.15	Accumulated orbital phase as a function of time for our aligned and anti-aligned runs. . . . .	65
2.16	The gravitational waveforms for our anti-aligned and aligned runs. . . . .	67
2.17	Spin-components of one of the neutron stars during the precessing simulation. . . . .	68
2.18	Components of the orbital frequency vectors during our evolutions. . . . .	69
2.19	Gravitational waveforms of our precessing run. . . . .	70
2.20	The normalized maximum density in each of our runs. . . . .	72
2.21	The Fourier transforms of the central density in all three of our runs. . . . .	73
2.22	Fourier transforms of several different quantities in the <b>S.4z</b> run. . . . .	75
3.1	Visualization of the Bh-Ns domain decomposition. . . . .	87
3.2	Convergence of the Euler constant for the R1460 $\uparrow$ . . . . .	95
3.3	Convergence of black hole spin and mass. . . . .	97
3.4	Hamiltonian and momentum constraints of the R14i60 $\uparrow$ ID set . . . . .	99
3.5	Neutron star surface and spin accuracy. . . . .	100
3.6	3d parameter space plot of Bh-Ns initial data sets. . . . .	102
3.7	Constraints for the $\chi_{\text{NS}}$ sequence. . . . .	104
3.8	$\chi_{\text{NS}}$ as a function of $\omega_{\text{NS}}$ for bh-ns binaries . . . . .	105
3.9	Hamiltonian and momentum for the sequence in $\chi_{\text{BH}}$ . . . . .	107
3.10	Measured neutron star spin plotted as a function of black hole spin. . . . .	108
3.11	Hamiltonian and momentum constraint for the $q$ sequence. . . . .	109
3.12	$\chi_{\text{NS}}$ as a function of mass ratio $q$ . . . . .	110
4.1	A typical run illustrating junk radiation. . . . .	116
4.2	Junk radiation profiles for CF and SKS initial data, and a comparison to high resolution SKS initial data. . . . .	123
4.3	The flux, $F(t)$ , and the computation of $E_J$ for CF and SKS initial data. . . . .	125
4.4	$E_J$ as a function of $\delta t_C$ . . . . .	128

4.5	$E_J$ as a function of $1_R/\text{ex}$ . . . . .	129
4.6	Normalized irreducible mass curves for CF and SKS data. . . . .	132
4.7	Convergence of $M_{\text{irr}}(t)$ for CF initial data. . . . .	133
4.8	Convergence of $M_{\text{irr}}(t)$ for SKS initial data. . . . .	134
4.9	$\delta S(t)$ for CF and SKS initial data. . . . .	136
4.10	Convergence test of $\delta S(t)$ for CF initial data. . . . .	137
4.11	Convergence test of $\delta S(t)$ for SKS initial data. . . . .	138
4.12	Energy in junk radiation as a function of $\chi$ at various initial separations, for conformally flat initial data (left panel) and SKS initial data (right panel). Within the uncertainty limit, there is virtually no dependence of $E_J$ on $\chi$ . . . . .	139
4.13	Log-log plot of the energy in junk radiation as a function of initial separation for binaries where $\chi = 0$ . The black circles and red squares denote conformally flat and SKS initial data, respectively. The dotted lines are power law fits, with indices of $\sim -2.79$ and $\sim -2.55$ respectively. . . . .	140
4.14	$\delta M_{\text{eq}}$ as a function of initial separation for CF initial data. The dotted lines are the best fits to a power law plus a constant offset. . . . .	141
4.15	$\delta M_{\text{eq}}$ as a function of black hole spin $\chi$ for CF initial data, evaluated at each different initial separation. . . . .	143
4.16	$\delta S_{\text{eq}}$ vs. $D$ for CF initial data. The dotted curves are the best fit power law plus constant offsets. . . . .	144
4.17	Semi-log plot of $\delta S_{\text{eq}}$ as a function of $\chi$ for CF data. The dotted lines are the best fit exponentials. . . . .	145

# Chapter 1

## Introduction

### 1.1 Timeline

- Jun 15 - Send Harald completed draft of thesis and begin editing
- Jul 15 - Submit thesis
- Aug 30 - Defend thesis
- Each of the above could reasonably be pushed back 2 weeks depending on when Harald gets back to Toronto

### 1.2 Thesis TDL

- Fix all short captions of ch 5
- Modify introduction of introduction to discuss detection of gravitational waves
- Add introduction section to discuss detection of gravitational waves
- Need introduction section on current status of NR
- Organize what papers to put into that section

- Fix  $\Omega$  driver section in the paper to use accurate equations
- Fix caption for 3+1 decomp text and add a sentence referencing it
- Read bunch of bh-ns papers to motivate the introduction of that section better.  
Log these papers in mendeley.
- Write up numerical methods section for bh-ns
- Add citation for dimensional reduction techniques
- fix table ref on page 33
- what does “appropriate averaging” mean on page 8?
- find a citation for PN results and methodology
- find a citation for the TT decomposition
- fix reference to fig binary evolution
- collaction misspelled in ch2

## 1.3 Introduction

Einstein’s theory of general relativity (GR) is now over a century old. One of its most striking predictions is the existence of gravitational waves (GWs) - ripples in space-time that propagate at the speed of light. One of the ways these gravitational waves are generated is through the inspiral of compact object binaries. In these binaries, a neutron star (NS) or a black hole (BH), orbits with a NS/BH companion about their common centre of mass. Over time, through the emission of GW, the orbit shrinks and eventually the objects merge. Although these GW have never been directly detected, their existence has been indirectly confirmed. Hulse and Taylor won the 1993 Nobel Prize for

their observations of the Hulse-Taylor pulsar (Hulse & Taylor (1975a)) - a binary pulsar system whose orbital decay was carefully measured and found to match perfectly with the predictions of general relativity. Further observations have since strengthened these findings; see Berti et al. (2015) for a detailed review of current and future tests of GR.

Ground-based interferometric gravitational wave detectors are poised to make direct detections of GWs. With Advanced LIGO (Harry (2010); Aasi et al. (2015)) recently beginning its first science run, and Advanced Virgo (The Virgo Collaboration (2010); Acernese et al. (2015)) and KAGRA (Somiya & the KAGRA Collaboration (2012)) to soon follow, the first direct detection may come soon. Advanced LIGO expect a realistic event rate  $\sim 30$  binary neutron star mergers per year at design sensitivity, with a horizon distance of  $\sim 200$  Mpc. Similarly, an event rate of  $\sim 10$  mergers per year is expected for binary black holes, and  $\sim 10$  for BH-NS binaries. These detectors are sensitive to frequencies of  $\sim 10\text{Hz} - 1\text{kHz}$ . Other detection methods, like pulsar timing arrays (see Joshi (2013)), are sensitive to very different frequency bands ( $300\text{pHz} - 100\text{nHz}$ ).

These ground-based detectors use the technique of matched filtering to make detections, in which the observed signal is matched against template waveforms to search for the astrophysical signal. These templates are generated either using an analytical, using, for example, Post-Newtonian theory, an perturbative expansion of GR, or by using numerical relativity (NR), in which the Einstein Field Equations are solved numerically on supercomputers. PN wave are cheap to produce but become increasingly inaccurate near merger, while NR waveforms are more accurate, but are costly to produce. Hybridization techniques “stitch” PN waveforms together with NR waveforms to get the best of both worlds.

The parameter space of numerical relativity simulations of black hole binaries is seven dimensional. Each black hole has a spin vector  $\vec{\chi}$  with three components, and their mass ratio  $q \equiv m_1/m_2$ , where  $m_1$  is the mass of the larger hole, is the 7th dimension. The total mass of the binary is scaled out of the numerical problem. Most compact object

systems are expected to circularize in their orbits before merger, so we do not regard orbital eccentricity as part of the parameter space. Spanning this parameter space is a difficult endeavour for numerical relativity collaborations and much of it remains uncovered. Various dimensional reduction techniques are used for Advanced LIGO template banks.

Once matter is added to simulations, through neutron stars, the parameter space increases significantly. In addition to the 7 parameters already present in the black hole binaries, the total mass of the system is now a parameter, as the maximum NS provides a natural physical mass scale. This can affect, for example, whether or not a hyper-massive neutron star is present after the merger or if direct collapse to a black hole occurs. In addition, the NS equation of state (EOS) becomes important to the system. Many research groups use a polytropic equation of state  $P = \kappa \rho^\Gamma$ , as a simple choice. Recently, more focus has been placed on using piece-wise polytropes or tabulated EOS to represent EOS motivated by nuclear theory. There is hope that detections by advanced LIGO will place constraints on the EOS of dense matter by measuring the orbital effect of tidal deformations of the NSs during the last stages of the orbit. Finally, the addition of matter adds additional physics to the problem. Numerical relativity simulations can investigate, for example, neutrino heating in the post-merger disk, or the growth of magnetic fields that are thought to power short gamma ray bursts (GRBs). The field of multi-messenger seeks to use GW observations together with electromagnetic and neutrino observations to learn more about merging NS systems.

NS-NS binaries, unlike BH-BH and BH-NS binaries, have been observed and studied within our galaxy, and therefore the expectations of Advanced LIGO for NS-NS binaries are more tightly constrained. The known binary neutron star population is summarized in table ?? . We report the spin periods, orbital periods, eccentricities, characteristic life-times ( $\tau_c = \dot{P}/2P$ ), time until merger, and the final spin periods of systems that will merge in a Hubble time. The system J0737-3039 is particularly interesting, as one of the

Table 1.1: The properties of known double neutron star systems

System	$P(ms)$	$P_{\text{orb}}(d)$	$e$	$\log_{10} \tau_c(yr)$	$\log_{10} \tau_g(yr)$	$P_f(ms)$
J0737-3039	22.7	0.102	0.088	8.3	7.9	26.8
J0737-3039	2770	0.102	0.088	7.7	7.9	4453
J1518+4904	40.9	8.6	0.25	10.3	12.4	—
B1534+12	37.9	0.32	0.27	8.4	9.4	126
J1756-2251	28.5	0.32	0.18	8.6	10.2	—
J1811-1736	104.2	18.8	0.83	9.0	13.0	—
B1820-11	279.8	357.8	0.79	6.5	15.8	—
J1829+2456	41.0	1.18	0.14	10.1	10.8	—
J1906+0746	144.1	0.17	0.085	5.1	8.5	7224
B1913+16	59.0	0.3	0.62	8.0	8.5	120
B2127+11C	30.5	0.3	0.67	8.0	8.3	52.6

NSs will merge with a spin period of 22.4ms. This is comparable enough to the orbital timescale near merger,  $P \sim 2ms$ , to be relevant to GW data analysis. NSs in binaries are spinning, and thus it is important to do NR simulations of spinning NS-NS binaries. For many years, spin was a largely unexamined dimension of the BNS parameter space, although there has been a significant interest lately. **Add a note on why we want to study bns binaries. Add a note on corotational vs. irrotational vs. spinning.**

This thesis is largely interested in spinning neutron stars in numerical relativity. The structure is as follows: In chapter 2, we discuss our work on initial data and evolutions of spinning NS-NS binaries using the SpEC code. In chapter 3, we discuss the extension of this initial data formalism to NS-BH binaries with a spinning NS. In chapter 4, we discuss the application of our initial data to studying spinning NS-NS binaries with interacting magnetic fields. In chapter 5, we shift focus and discuss work we have done on understanding the nature of “junk radiation” in Binary BH systems. Finally, in chapter



6 we conclude and summarize the thesis and discuss future possibilities.

The remainder of this introduction is structured as follows: In Section 1.4 we review the 2-body problem in GR and discuss some basic Post-Newtonian theory. In section 1.5, we review the initial value problem in NR. Finally, in section 1.6 we discuss some basic astrophysical properties of binary neutron star systems.

## 1.4 The two-body problem in General Relativity

In this section, we will review the basic scales and ideas that govern the two-body problem in general relativity. Specifically, when the bodies are of comparable masses (i.e., the mass ratio is not a perturbative parameter). Since the inspiral of two compact objects is driven by the emission of gravitational radiation, we begin by reviewing gravitational waves.

We consider a perturbation to a Minkowski background, so we write the full metric as

$$g_{\mu\nu} = \eta_{\mu\nu} + h_{\mu\nu} \quad |h| \ll 1. \quad (1.1)$$

It is easily verified that the inverse metric is

$$g^{\mu\nu} = \eta^{\mu\nu} - h^{\mu\nu}, \quad (1.2)$$

where

$$h^{\mu\nu} = \eta^{\mu\rho} \eta^{\sigma\nu} h_{\rho\sigma}, \quad (1.3)$$

as the assumption that  $|h|$  is small allows us to neglect terms that are higher than first order in  $h_{\mu\nu}$ . It is now helpful to consider the “trace-reversed” perturbation defined as,

$$\bar{h}_{\mu\nu} = h_{\mu\nu} - \frac{1}{2} h \eta_{\mu\nu}. \quad (1.4)$$

It is easily verified that  $\bar{h} = -h$ , hence the name “trace-reversed”. Next, we exploit our coordinate freedom and work in the Lorentz gauge, defined by

$$\nabla_\mu \bar{h}^{\mu\nu} = 0. \quad (1.5)$$

In this gauge, the Einstein tensor is simply

$$G_{\mu\nu} = -\frac{1}{2}\nabla_\rho\nabla^\rho\bar{h}_{\mu\nu}, \quad (1.6)$$

and so in vacuum, the Einstein field equations are a wave equation

$$\square\bar{h}_{\mu\nu} = 0. \quad (1.7)$$

Thus we see that gravitational waves propagate at the speed of light. Using further coordinate freedom, it is convenient to work in the traceless-transverse (TT) gauge, defined by

$$\bar{h}_{\mu 0}^{\text{TT}} = 0 \quad \bar{h}^{\text{TT}} = 0. \quad (1.8)$$

The first condition guarantees that the non-zero components of  $\bar{h}_{\mu\nu}^{\text{TT}}$  are purely spatial, while the traceless condition guarantees that  $\bar{h}_{\mu\nu}^{\text{TT}} = \bar{h}_{\nu\mu}^{\text{TT}}$ . For the rest of this section, we will work only in the TT gauge.

The Lorentz gauge condition, transverse condition, and traceless condition account for 8 of the 10 degrees of freedom in the gravitational field  $h_{\mu\nu}$ . The remaining two degrees of freedom correspond to the two polarization states of gravitational waves. These are known as the “+” and “ $\times$ ” polarizations, due to their particular distorting effects acting upon a ring of particles (see Fig. 1.1). We can thus decompose a gravitational wave as

$$h_{ij}^{\text{TT}} = h_+e_{ij}^+ + h_\times e_{ij}^\times. \quad (1.9)$$

When a matter source is present, the wave equation becomes

$$\nabla_\rho\nabla^\rho h_{\mu\nu} = -16\pi T_{\mu\nu}. \quad (1.10)$$

The solution to this equation can be written with the help of a Green’s function,

$$h_{\mu\nu}(t, x^i) = 4 \int d^3y \frac{1}{|x - y|} T_{\mu\nu}(t_r, y^i), \quad (1.11)$$

where  $t_r$  is the “retarded” time,  $t_r = t - |x - y|$ . This integral can be evaluated in terms of the quadrupole tensor  $I^{ij}$  defined by

$$I^{ij}(t) = \int d^3x x^i x^j T^{00}(t, x^i), \quad (1.12)$$

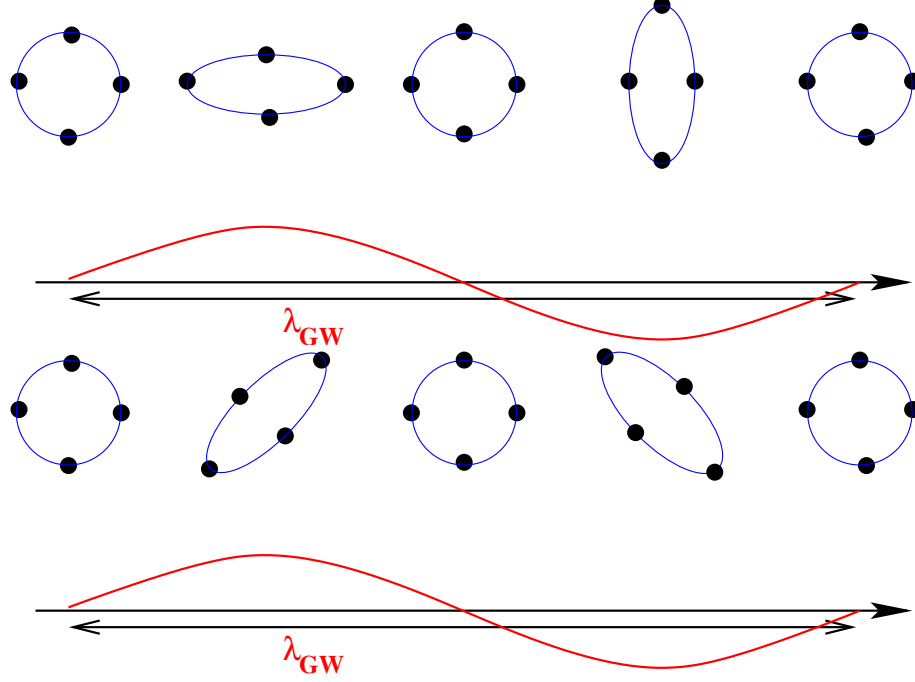


Figure 1.1: From Buonanno (2007). The top panel shows the effect of a + polarized gravitational wave passing through a ring of particles, in the direction perpendicular to the plane of the ring. The bottom panel shows the effect of a  $\times$  polarized gravitational wave.

and the reduced quadrupole moment

$$J_{ij} = I_{ij} - \frac{1}{3}\eta_{ij}I, \quad (1.13)$$

where  $I = I^\mu_\mu$ . The result is

$$h_{ij}(t, x^i) = \frac{2}{r}\ddot{J}^{\text{TT}}_{ij}(t_r) \quad (1.14)$$

In other words, linear gravitational waves are sourced by an oscillating quadrupole. To study the energy content of these gravitational waves, note that the effective stress-energy tensor of this spacetime is

$$T_{\mu\nu} = \frac{1}{32\pi} \langle \partial_\mu h_{ij} \partial_\nu h^{ij} \rangle. \quad (1.15)$$

where  $\langle \rangle$  denotes an appropriate averaging. This can be integrated to find the energy

output per unit time in gravitational waves,

$$L_{GW} = \frac{r^2}{16\pi} \oint \langle \dot{h}_\times^2 + \dot{h}_+^2 \rangle d\Omega \quad (1.16)$$

$$= \frac{1}{5} \langle \ddot{J}_{ij}^{\text{TT}} \ddot{J}^{\text{TT}ij} \rangle. \quad (1.17)$$

Let us now consider a circular binary with total mass  $M$ , reduced mass  $\mu$ , separation  $R$  and orbital frequency  $\omega$ . Direct computation of the quadrupole tensor gives the simple result

$$L_{GW} = \frac{32}{5} \mu^2 M^3 R^{-5}. \quad (1.18)$$

Using this, along with the Newtonian estimates  $\omega = M^{1/2} R^{-3/2}$ ,  $E = -\frac{\mu M}{2R}$ ,  $dE/dt = -L_{GW}$ , allows us to compute the characteristic inspiral scales. The binary shrinks at a rate

$$\frac{dR}{dt} = \frac{dE/dt}{dE/dr} = -\frac{64}{5} M^2 \mu R^{-3}. \quad (1.19)$$

Integrating this expression gives the time to coalescence where  $R = 0$  as

$$\tau_c = \frac{5}{256} M^{-2} \mu^{-1} R^4. \quad (1.20)$$

As the binary separation decreases, the orbital frequency increases. By integrating

$$\frac{df_{GW}}{dt} = \frac{1}{\pi} \frac{d\omega}{dt} = \frac{-3M^{1/2}}{2} R^{-5/2} \frac{dR}{dt}, \quad (1.21)$$

the frequency evolution is given by

$$f_{GW}(t) = \frac{\omega}{\pi} = \frac{1}{8\pi} \left( \frac{5}{\mu M^{2/3} (\tau_c - t)} \right)^{3/8}. \quad (1.22)$$

The number of gravitational waves cycles,  $N = \int f_{GW} dt$ , in a given frequency band  $df_{GW}$  is given by

$$\frac{dN}{d \log f_{GW}} = \frac{5}{96\pi} \frac{1}{(\pi \mathcal{M} f_{GW})^{5/3}}, \quad (1.23)$$

where the quantity  $\mathcal{M} = \mu^{3/5} M^{2/5}$  is called the “chirp mass”. The explicit radiation pattern is given by

$$h_+ = \frac{4}{r} \mathcal{M}^{5/3} (2\omega)^{2/3} \cos(2\omega t + \phi) \left( \frac{1 + \cos^2 \theta}{2} \right), \quad (1.24)$$

$$h_\times = \frac{4}{r} \mathcal{M}^{5/3} (2\omega)^{2/3} \sin(2\omega t + \phi) \cos \theta, \quad (1.25)$$

where  $r$  is the distance to the source,  $\theta$  is the angle between the observer and the axis normal to the orbital plane of the binary, and  $\phi$  is the arbitrary phase of the binary. Detectors are sensitive to the strain  $h$ , rather than the energy flux, and therefore a factor of  $x$  improvement in sensitivity results in a factor of  $x^3$  higher event rate (assuming a uniformly placed distribution of sources).

These estimates were all made for a circular binary. If the binary has some eccentricity,  $e$ , then equation 1.16 is modified to

$$L_{GW} = \frac{32}{5} \mu^2 M^3 R^{-5} \left( 1 + \frac{73}{24} e^2 + \frac{37}{96} e^4 \right) (1 - e^2)^{-7/2} \quad (1.26)$$

However, eccentricity is radiated away as the inspiral proceeds. The classic reference of Peters(1964) found that

$$\left\langle \frac{de}{dt} \right\rangle = -\frac{304}{15} e \frac{\mu M^2}{R^4 (1 - e^2)^{5/2}} \left( 1 + \frac{121}{304} e^2 \right). \quad (1.27)$$

Thus even a highly eccentric binary will radiate away its eccentricity and circularize before merger, provided the compact objects started far enough away from each other. Most numerical relativity simulations consider only circularized binaries and use techniques to attempt to get rid of any residual eccentricity.

The equations above in this section are valid only for a slowly-moving, weak-field system. As the system gets closer and closer to merger, these equations become increasingly inaccurate. Post-Newtonian theory, by expanding to higher order, allows us to consider binaries with higher orbital frequencies. It is typically written as an expansion in the dimensionless parameter

$$x = \left( \frac{GM\omega}{c^3} \right)^{(2/3)}. \quad (1.28)$$

The evolution of the orbital phase, for example, can be written as

$$\phi = \frac{-x^{-5/2}}{32\nu} \left( 1 + a_1 x + a_2 x^{3/2} + a_3 x^2 + a_4 x^{5/2} + a_5 x^3 + a_6 x^{7/2} + \mathcal{O}(1/c^8) \right) \quad (1.29)$$

where  $\nu$  is the symmetric mass ratio,  $\nu = \frac{m_1 m_2}{(m_1 + m_2)^2}$ , and each of the  $a_i$  are functions only of  $\nu$  and  $\log x$ . This expression is said to be known to 3.5 Post-Newtonian order.

Additional contributions come in at other PN orders, such as spin-orbit coupling at 1.5 PN order, spin-spin coupling at 2 PN order and tidal effects at 5 PN order. See [cite](#) for an overview of PN results and methodology.

## 1.5 The initial value problem in Numerical Relativity

From the point of view of numerical relativity, it is natural to use a 3+1 decomposition of space-time. In this section, we will review this process. Given a globally hyperbolic spacetime  $(M, g_{\mu\nu})$ . We foliate  $M$  by a set of  $t = \text{const}$  hypersurfaces  $\Sigma_t$ .

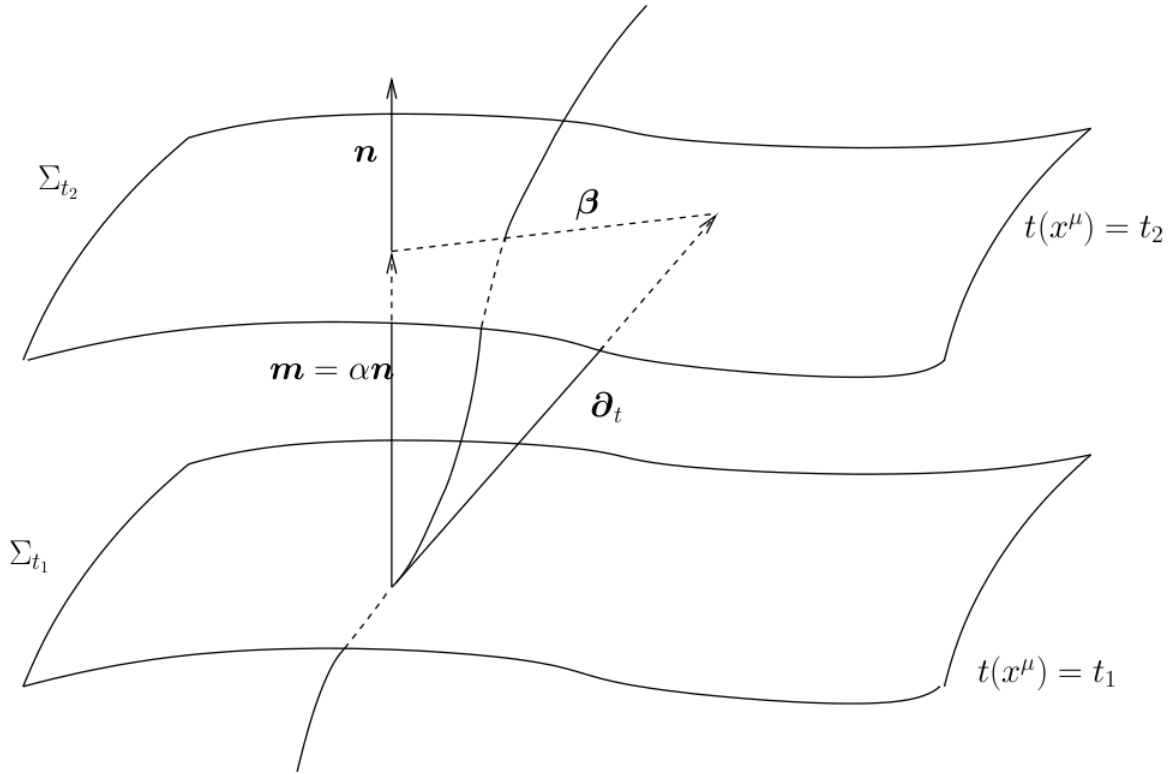


Figure 1.2: [add caption - from here http://relativity.livingreviews.org/Articles/lrr-2015-1/articlese6.html](http://relativity.livingreviews.org/Articles/lrr-2015-1/articlese6.html)

Each surface has a forward pointing unit normal

$$n^\mu = -g^{\mu\nu} \nabla_\nu t (g^{\mu\nu} \nabla_\mu t \nabla_\nu t)^{-1/2}, \quad (1.30)$$

induced metric

$$\gamma_{\mu\nu} = g_{\mu\nu} + n_\mu n_\nu, \quad (1.31)$$

and compatible derivative operator  $D$ . The induced metric measure curvature inside each hypersurface, while the extrinsic curvature  $K_{\mu\nu}$  measures how the hypersurface is curved inside the space-time manifold  $M$ . It is defined by

$$K_{\mu\nu} = -\frac{1}{2}\mathcal{L}_n g_{\mu\nu}, \quad (1.32)$$

where  $\mathcal{L}_n$  is the usual Lie derivative, along the direction of the vector field  $n^\mu$ . The space-time metric is written as

$$ds^2 = -\alpha^2 dt^2 + \gamma_{ij} (dx^i + \beta^i dt) (dx^j + \beta^j dt). \quad (1.33)$$

Here  $\alpha$  is known as the lapse function - it measures the proper time between neighbouring hypersurfaces.  $\beta^i$  is known as the shift - it measures the proper distance within a spatial hypersurface. The lapse and shift are both arbitrary - their choice amounts to a choice of coordinates.

Similar to how Maxwell's equations can be written as a set of constraint equations that do not contain any time derivatives,

$$D_i E^i - 4\pi\rho = 0, \quad (1.34)$$

$$D_i B^i = 0, \quad (1.35)$$

and evolution equations,

$$\partial_t E_i = \epsilon_{ijk} D^j B^k - 4\pi j_i \quad (1.36)$$

$$\partial_t B_i = -\epsilon_{ijk} D^j E^k, \quad (1.37)$$

(where  $E^i$  is the electric field,  $B^i$  is the magnetic field,  $\rho$  is the charge density,  $j^i$  is the current density, and  $\epsilon_{ijk}$  is the Levi-Civita symbol, and the equations are written in

Gaussian units), the same is true of Einstein's equations. The famous Hamiltonian and momentum constraints are

$$R + K^2 - K_{ij}K^{ij} = 16\pi\rho, \quad (1.38)$$

and,

$$D_j K_i^j - D_i K = 8\pi S_i \quad (1.39)$$

where  $\rho$  is the energy density measured by a normal observer,  $\rho = n_i n_j T^{ij}$ , and  $S_i$  is the momentum density measured by a normal observer  $S_i = -\gamma_i^j n^k T_{jk}$ . These are elliptic equations for the geometric quantities defined on the  $\Sigma_t$ . The general task of constructing initial data is to find  $(\Sigma, g_{\mu\nu}, K_{\mu\nu})$  that satisfy the constraint equations and represent well the physical situation at hand (e.g., the inspiral of a compact object binary). The evolution equations are

$$\partial_t \gamma_{ij} = -2\alpha K_{ij} + D_i \beta_j + D_j \beta_i \quad (1.40)$$

and

$$\partial_t K_{ij} = -D_i D_j \alpha + \alpha (R_{ij} - 2K_{ik} K_j^k + K K_{ij}) - 8\pi\alpha (S_{ij} - \frac{1}{2}\gamma_{ij}(S - \rho)) + \beta^k D_k K_{ij} + K_{ik} D_j \beta^k + K_{kj} D_i \beta^k \quad (1.41)$$

, where  $S_{ab}$  is the spatial stress,  $S_{ab} = \gamma_a^c \gamma_b^d T_{cd}$ , and  $S$  is its trace. Once constraint satisfying initial data has been constructed, the evolution equations determine the geometric quantities at all future times. Analytically, the evolution equations preserve the constraints, although numerically this may not always be the case.

There are many sets of data  $(g_{\mu\nu}, K_{\mu\nu})$  that will satisfy the constraint equations. The task remains, then, to choose this free data appropriately. To do so, one typically begins with a conformal decomposition of the metric,

$$\gamma_{ij} = \Psi^4 \tilde{\gamma}_{ij}. \quad (1.42)$$

Here,  $\Psi$  is called the conformal factor, and  $\tilde{\gamma}_{ij}$  is called the conformal metric. Next we break up the extrinsic curvature into its trace and trace-free parts,

$$K_{ij} = A_{ij} + \frac{1}{3}\gamma_{ij}K. \quad (1.43)$$



The Hamiltonian and Momentum constraints become

$$\tilde{D}^2\Psi - \frac{1}{8}\Psi\tilde{R} - \frac{1}{12}\Psi^5K^2 + \frac{1}{8}\Psi^{-5}\tilde{A}_{ij}\tilde{A}^{ij} = -2\pi\Psi^{-5}\rho. \quad (1.44)$$

$$D_j A^{ij} - \frac{2}{3}D^i K = 8\pi j^i, \quad (1.45)$$

$\tilde{A}^{ij} = \Psi^{-10}A^{ij}$ . We now proceed according to the extended conformal thin sandwich formalism. See [cite](#) for a review of the alternative traceless-transverse decomposition. We define

$$\tilde{u}_{ij} = \partial_t \tilde{\gamma}_{ij}, \quad (1.46)$$

and we introduce the scalings

$$\tilde{j}^i = \Psi^{10}j^i, \quad (1.47)$$

$$\tilde{\rho} = \Psi^8\rho \quad (1.48)$$

$$\tilde{A}^{ij} = \Psi^{10}A^{ij}. \quad (1.49)$$

The Hamiltonian and Momentum constraints can now be viewed as equations for the shift and conformal factor

$$\tilde{D}^2\Psi - \frac{1}{8}\Psi\tilde{R} - \frac{1}{12}\Psi^5K^2 + \frac{1}{8}\Psi^{-7}\tilde{A}_{ij}\tilde{A}^{ij} = -2\pi\Psi^{-3}\tilde{\rho}, \quad (1.50)$$

$$\tilde{D}_j \left( \frac{1}{2\tilde{\alpha}} (\mathbb{L}\beta)^{ij} - \tilde{D}_j \left( \frac{1}{2\tilde{\alpha}} \tilde{u}^{ij} \right) \right) - \frac{2}{3}\Psi^6\tilde{D}^i K = 8\pi\tilde{j}^i, \quad (1.51)$$

where

$$\tilde{\alpha} = \Psi^6\alpha \quad (1.52)$$

is the conformal lapse and

$$\left( \tilde{\mathbb{L}}\beta \right)^{ij} = \Psi^4 \left( D^i\beta^j + D^j\beta^i - \frac{2}{3}\gamma^{ij}D_k\beta^k \right) \quad (1.53)$$

is the conformal longitudinal operator. The lapse is given by the evolution equation of  $K$ ,

$$\begin{aligned} \tilde{D}^2 (\tilde{\alpha}\Psi^7) - (\tilde{\alpha}\Psi^7) \left[ \frac{1}{8}\tilde{R} + \frac{5}{12}\Psi^4 K^2 + \frac{7}{8}\Psi^{-8}\tilde{A}_{ij}\tilde{A}^{ij} \right. \\ \left. + 2\pi\Psi^{-2}(\tilde{E} + 2\tilde{S}) \right] = -\Psi^5 (\partial_t K - \beta^k D_k K). \end{aligned} \quad (1.54)$$

The free data are  $\tilde{\gamma}_{ij}, \tilde{u}_{ij}, K, \partial_t K$ . In a coordinate system corotating with the binary, it is natural to choose  $\tilde{u}_{ij} = 0, \partial_t K = 0$ . Common choices are conformal flatness,  $\tilde{\gamma}_{ij} = \delta_{ij}$  and maximal slicing  $K = 0$ . With appropriate boundary conditions, the system of equations can now be solved.

## 1.6 Binary Neutron Star Systems

To begin our discussion of the properties of binary neutron star binaries, we should first briefly review how these system forms. We follow the discussion outlined in Postnov & Yungelson (2014). The standard formation scenario is illustrated in figure ??, and goes as follows:

- We begin with two high mass OB main-sequence stars undergoing standard binary evolution. Eventually the more massive (primary) star burns its central hydrogen, and a helium core is left over.
- The primary star then rapidly expands, overflows its Roche lobe, and begins a period of mass transfer onto the secondary star. This period lasts until most of the primary's Hydrogen envelope has been transferred, leaving behind a naked helium core.
- The primary star eventually collapses as a core-collapse supernova, leaving behind a neutron star. It is likely that the explosion disrupts the binary, but let us assume that it survives. We then have a massive main sequence star in orbit with a neutron star.

- Eventually the secondary star evolves off the main sequence, expands, and overflows its Roche lobe. It will then begin accreting mass onto the primary. This accretion spins up the neutron star, thus “recycling” it. It also leads to strong x-ray emission.
- The secondary further expands and a common envelope stage ensues. Eventually the secondary explodes as a supernova, and becomes a neutron star.
- If the system is not disrupted, it can then become a binary that will eventually merge due to the continuous emission of gravitational waves.

As discussed earlier, such systems are expected to be quasi-circular once they enter the LIGO band. There are, however, other ways of forming systems that are highly eccentric while in the LIGO band. For example, the dynamical capture in a close two-body encounter in a dense cluster environment, or a binary in a hierarchical triple system whose eccentricity is enhanced by the Kozai mechanism. Nonetheless, quasi-circular binaries are expected to constitute the large majority of gravitational wave sources.

The end state of a binary neutron star merger depends strongly on the properties of the stars. For systems with a combined mass less than the maximum mass allowed by the EOS, the final result would be a more massive neutron star. Otherwise, the final result will be a single Kerr black hole. Simulations have shown that these black holes will have a spin on the order of  $\chi \simeq 0.6 - 0.8$ . The intermediate state is known as a hypermassive neutron star (HMNS). This is a NS whose mass is above the maximum mass allowed by the EOS, temporarily supported by differential rotation and thermal pressure. Over time, angular momentum is efficiently transported out of the system, and it collapses into a black hole. We can further subdivide these systems based on the timescale for collapse - prompt collapse or delayed collapse. In the prompt case, the pressure support is too low, and the system collapses on a  $\sim$  freefall timescale. This is expected in systems with a large total mass ( $\gtrsim 2.8M_{\odot}$ ), although the details depend, of course, on the EOS. In the delayed collapse case, the collapse timescale depends on

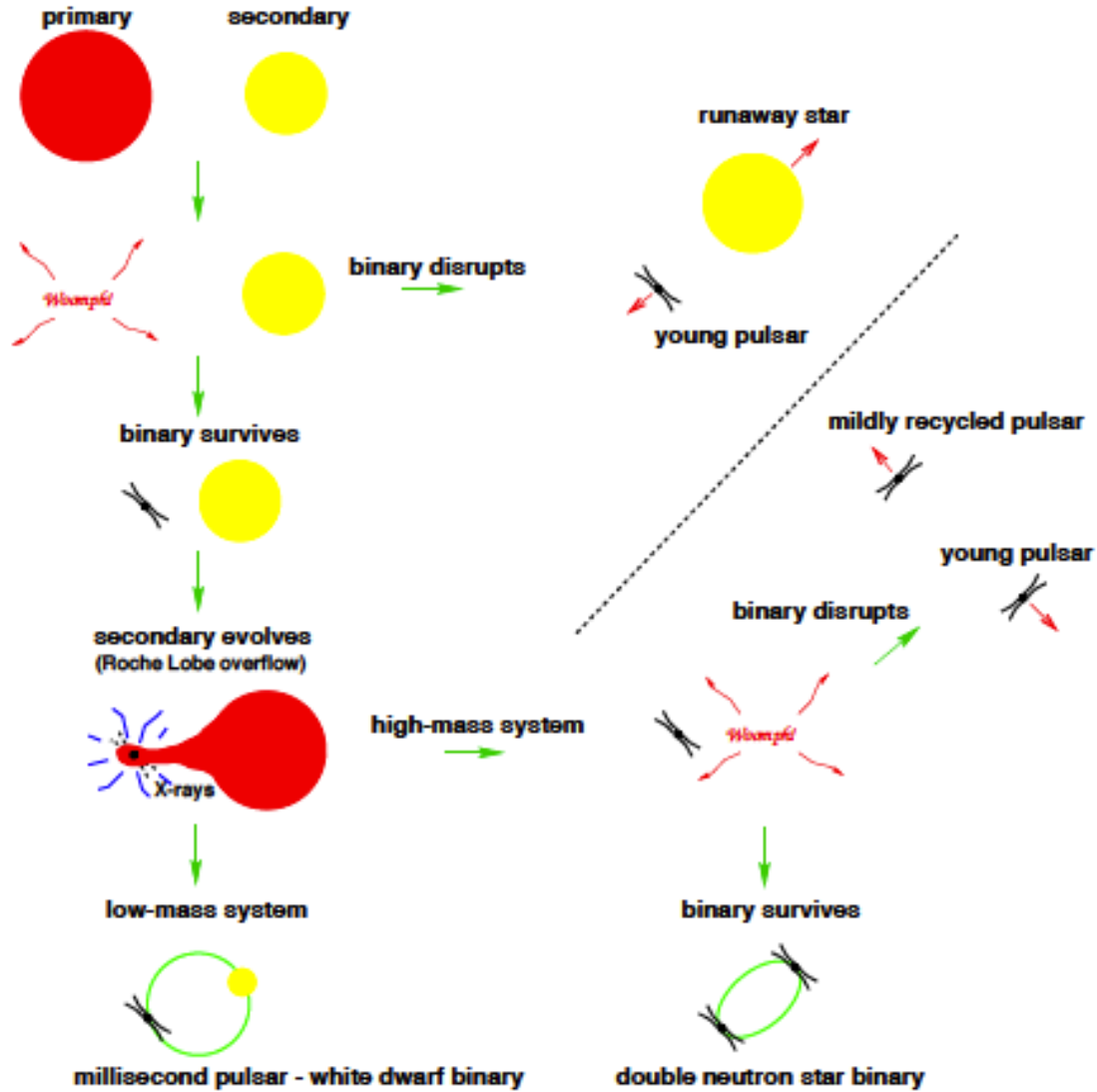


Figure 1.3: From Lorimer (2008). The possible evolutionary scenarios of a typical high mass binary are shown.

many factors. Angular momentum distribution by magnetic winding is an important factor - it operates on the Alfvén timescale  $\tau \sim R\sqrt{\rho}/B \simeq 10 - 100\text{ms}$ . Transport driven by magneto-rotational instability is also important. It is of the order  $\tau \sim 100\text{ms}$  for  $B \simeq 10^{15}\text{G}$ . Cooling by neutrino or electromagnetic emission is also important, as

it decreases thermal pressure, although it operates on a longer timescale,  $\sim$  seconds. An accretion disk around the eventual BH, lying beyond the ISCO, will form, with a mass of  $\simeq 0.01 - 0.3M_{\odot}$ . The amount of material in the disk depends on the time to BH formation, as there is more time to distribute angular momentum of the disk. HMNS systems emit gravitational waves at peak frequencies of approximately  $2 - 4\text{kHz}$ , unfortunately outside of the optimal frequency range of ground-based detectors. The mass ratio of the system is another important factor. Figure 1.4 shows the post-merger remnant of an equal-mass system, and of a system with mass ratio  $q \sim 1.38$ . The equal mass system shows a “dumbbell”-like structure, composed of two cores which, over time, turn into an ellipsoidal HMNS. The non-equal-mass case shows two asymmetric cores, which act like the smaller one orbiting the larger one. The stronger tidal forces in this case cause the outer layers of the smaller star to be stripped off and form an envelope around the HMNS. Higher disk mass correlates with higher deviations from  $q = 1$ , as well as with higher NS compactness.

The merger of two neutron stars is the site of the emission of a tremendous amount of electromagnetic energy. Their mergers are thought to be one of the most promising candidates to be the progenitors of short gamma ray bursts (SGRBs), although there is not yet definitive evidence of it. The engine of a rotating black hole, surrounded by a hot accretion torus and a collimated magnetic field contains the necessary ingredients thought to be needed for a SGRB. Apart from this, another promising candidate for electromagnetic signature is the “kilonova” - emission powered by the radioactive decay of r-process elements formed in the merger, lasting on the time-scale of  $\sim$  weeks. Multi-messenger astronomy (see Fan & Hendry (2015) for a review) seeks to combine information from gravitational waves, these electromagnetic events, and possible neutrino observations, to further elucidate the astrophysics of these mergers.

One of the most exciting prospects of the Advanced LIGO era is using gravitational wave observations to constrain the NS EOS. The EOS of dense nuclear matter is an open

question of tremendous interest to nuclear physicists and astrophysicists alike. Tidal effects are parameterized by the tidal deformability parameter  $\lambda$ , which relates the induced quadrupole field of one star,  $Q_{ij}$ , to the tidal field in which it is immersed,  $\mathcal{E}_{ij}$ :

$$Q_{ij} = -\lambda(m; \text{EOS}) \mathcal{E}_{ij}. \quad (1.55)$$

Or, likewise, by the second tidal Love number,

$$k_2 = \frac{3}{2} \frac{\lambda}{R^5}. \quad (1.56)$$

These enter the PN equations for binary phase at the very high 5PN order, but because of the large pre-factors, they are still very important in the late-stage inspiral dynamics. Much work has been done to estimate how well Advanced LIGO can measure these parameters (see Read et al. (2009); Hinderer et al. (2010); Damour et al. (2012); Lackey et al. (2012)). Del Pozzo et al. (2013) (further extended in Agathos et al. (2015)) used a Bayesian framework to show that  $\lambda$  could be constrained at the 10% level after a few tens of detections. There is also the question of more exotic NS matter. Chatziioannou et al. (2015) studied various possibilities and found, for example, that a detection with an SNR of  $\sim 20$  could provide good evidence of the existence or non-existence of strange quark stars. However, kaon condensates or hyperons in NS cores are much more difficult to confirm.

Numerical simulations of the mergers of binary neutron stars have been possible for at least fifteen years [cite](#). Since then, simulations have rapidly progressed, adding more resolution, more orbits, more detailed physics, and a better coverage of the available parameter space. [Cite a bunch of papers here, on those different things](#). With the great increase in simulation technology, and the coincident start of the Advanced LIGO era, it is truly an exciting time for this field.

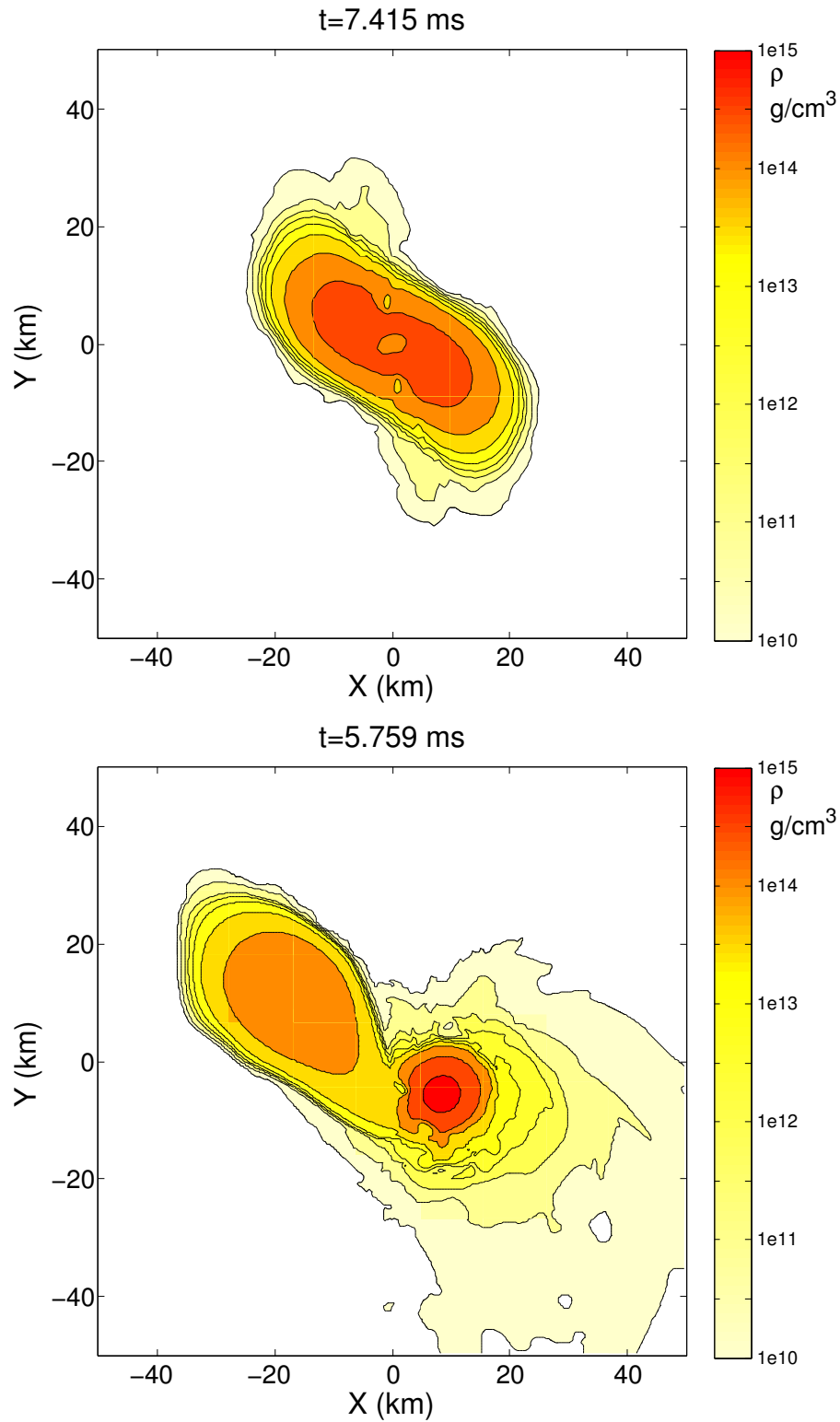


Figure 1.4: From Rezzolla et al. (2010). The top panel shows the iso-density contours of the HMNS from an equal mass system with baryon masses  $M_1 = M_2 = 1.643M_\odot$ . The bottom panel shows the iso-density contours of the HMNS from a system with baryon masses  $M_1 = 1.304M_\odot$  and  $M_2 = 1.805M_\odot$ .

# Chapter 2

## Binary Neutron Stars with Arbitrary Spins in Numerical Relativity

- Modify text based on changes from submitted paper
- Modify figures so that they fit on one page
- Modify figure captions so that they are small

### 2.1 Chapter Overview

We present a code to construct initial data for binary neutron star systems in which the stars are rotating. Our code, based on a formalism developed by Tichy, allows for arbitrary rotation axes of the neutron stars and is able to achieve rotation rates near rotational breakup. We compute the neutron star angular momentum through quasi-local angular momentum integrals. When constructing irrotational binary neutron stars, we find a very small residual dimensionless spin of  $\sim 2 \times 10^{-4}$ . Evolutions of rotating neutron star binaries show that the magnitude of the stars' angular momentum



is conserved, and that the spin- and orbit-precession of the stars is well described by post-Newtonian approximation. We demonstrate that orbital eccentricity of the binary neutron stars can be controlled to  $\sim 0.1\%$ . The neutron stars show quasi-normal mode oscillations at an amplitude which increases with the rotation rate of the stars.

## 2.2 Introduction

Several known binary neutron star (BNS) systems will merge within a Hubble time due to inspiral driven by gravitational radiation Lorimer (2008), most notably the Hulse-Taylor pulsar Hulse & Taylor (1975b). Therefore, binary neutron stars constitute one of the prime targets for upcoming gravitational wave detectors like Advanced LIGO Harry (2010); Aasi et al. (2015) and Advanced Virgo The Virgo Collaboration (2010); Acernese et al. (2015). The neutron stars in known binary pulsars have fairly long rotation periods Lorimer (2008). The system J0737-3039 Lyne et al. (2004) contains the fastest known spinning neutron star in a binary with a rotation period of 22.7ms. This system will merge within  $\sim 10^8$  years through gravitational wave driven inspiral. Globular clusters contain a significant fraction of all known milli-second pulsars Lorimer (2008), which through dynamic interactions, may form binaries Lee et al. (2010); Benacquista & Downing (2013). Gravitational wave driven inspiral reduces Peters & Mathews (1963); Peters (1964) the initially high eccentricity of dynamical capture binaries. Given the presence of milli-second pulsars in globular clusters, dynamically formed BNS may contain very rapidly spinning neutron stars with essentially arbitrary spin orientations. Presence of spin in BNS systems does influence the evolution of the binary. For instance, in order to avoid a loss in sensitivity in GW searches, one needs to account for the NS spin Brown et al. (2012). Furthermore, early BNS simulations Shibata & Uryu (2000) of irrotational and corotational BNS systems found that the spin of corotating BNS noticeably increased the size of accretion discs occurring during the merger of the two NS. The properties of accretion discs and unbound ejecta are intimately linked to electromagnetic

and neutrino emission from merging compact object binaries Metzger & Berger (2012). Understanding the behavior of rotating BNS systems is therefore important to quantify the expected observational signatures from such systems. These considerations motivated a recent interest in the numerical modeling of rotating binary neutron star systems during their last orbits and coalescence. Baumgarte and Shapiro Baumgarte & Shapiro (2009), Tichy Tichy (2011), and East et al East et al. (2012) presented formalisms for constructing BNS initial data for spinning neutron stars. Tichy proceeded to construct rotating BNS initial data Tichy (2012); and Ref. Bernuzzi et al. (2014) studies short inspirals and mergers of BNS with rotation rates consistent with known binary neutron stars (i.e. a dimensionless angular momentum of each star  $\chi = S/M^2 \lesssim 0.05$ ), and rotation axes aligned with the orbital angular momentum. Very recently, Dietrich et al. Dietrich et al. (2015) presented a comprehensive study of BNS, including a simulation of a precessing, merging BNS. East et. al. East et al. (2015) investigate interactions of rotating neutron stars on highly eccentric orbit. Kastaun et al. Kastaun et al. (2013) determine the maximum spin of the black hole remnant formed by the merger of two aligned spin rotating neutron stars. Tsatsin and Marronetti Tsatsin & Marronetti (2013) present initial data and evolutions for non-spinning, spin-aligned and anti-aligned data sets. Tsokaros et. al. Tsokaros et al. (2015) presented initial data and quasi-equilibrium sequences of spin-aligned and anti-aligned binaries with a nuclear equation of state.

Previous studies differ in the type of initial data used: Refs. Baumgarte & Shapiro (2009); Tichy (2011; 2012); Bernuzzi et al. (2014) construct and utilize constraint-satisfying initial data, which also incorporates quasi-equilibrium of the binary system. Refs. East et al. (2012; 2015) construct constraint-satisfying data based on individual TOV stars, without regard of preserving quasi-equilibrium in the resulting binary, but providing greatly enhanced flexibility in the type of configurations that can be studied, e.g. hyperbolic encounters. Refs. Kastaun et al. (2013); Tsatsin & Marronetti (2013), finally, only approximately satisfy the constraint equations. Previous studies also differ in the

rigor with which the neutron star angular momentum is measured. Ref. Tichy (2012) merely discusses the neutron stars based on a rotational velocity  $\omega^i$  entering the initial data formalism (cf. our Eq. (2.48) below), whereas Refs. Bernuzzi et al. (2014); Kastaun et al. (2013); East et al. (2015) estimate the initial neutron star spin either based on single star models or based on the differences in binary neutron star initial data sets with and without rotation, and thus neglecting the impact of interactions in the binary. All these studies measure the neutron star angular momentum in the initial data. Changes in the neutron star angular momentum that could happen during initial relaxation of the binary or during the subsequent evolution of the binary are not monitored.

In this paper we study the construction of rotating binary neutron star initial data and the evolution through the inspiral phase. We implement the constant rotational velocity (CRV) formalism developed by Tichy Tichy (2012), and construct constraint satisfying BNS initial data sets with a wide variety of spin rates, as well as different spin directions. We apply quasi-local angular momentum techniques developed for black holes to our BNS initial data sets; the quasi-local spin indicates that we are able to construct BNS with dimensionless angular momentum exceeding 0.4. Evolving some of the constructed initial data sets through the inspiral phase, we demonstrate that we can control and reduce orbital eccentricity by an iterative adjustment of initial data parameters controlling orbital frequency and radial velocity of the stars, both for non-precessing (i.e. aligned-spin binaries) and precessing binaries. When monitoring the quasi-angular momentum of the neutron stars during the inspiral, we find that its magnitude is conserved, and the spin-direction precesses in a manner consistent with post-Newtonian predictions.

This paper is organized as follows. Section 4.5 describes the initial data formalism and our numerical code to solve for rotating BNS initial data. In Sec. 2.4 we use this code to study a range of initial configurations, with a special emphasis on the behavior of the quasi-local spin diagnostic. We evolve rotating BNS in Sec. 2.5, including a discussion of eccentricity removal, the behavior of the quasi-local spin diagnostics, and a comparison

of the precession dynamics to post-Newtonian theory. A discussion concludes the paper in Sec. 2.6. In this paper, we work in units where  $G = c = M_\odot = 1$ .

## 2.3 Methodology

### 2.3.1 Formalism for irrotational binaries

To start, we will review a formalism commonly used for the construction of initial data for system of irrotational binary neutron stars. We will then discuss how to build upon this formalism to construct initial data for neutron stars with arbitrary spins.

We begin with the 3+1 decomposition of the space-time metric (see Gourgoulhon (2007) for a review),

$$ds^2 = -\alpha^2 dt^2 + \gamma_{ij} (dx^i + \beta^i dt) (dx^j + \beta^j dt). \quad (2.1)$$

Here,  $\alpha$  is the lapse function,  $\beta^i$  is the shift vector and  $\gamma_{ij}$  is the 3-metric induced on a hypersurface  $\Sigma(t)$  of constant coordinate time  $t$ . In this decomposition, the unit normal vector  $n^\mu$  to  $\Sigma(t)$  and the tangent vector  $t^\mu$  to the coordinate line  $t$  are related by

$$t^\mu = \alpha n^\mu + \beta^\mu, \quad (2.2)$$

with  $n_\mu = (-\alpha, 0, 0, 0)$  and  $\beta^\mu = (0, \beta^i)$ . The extrinsic curvature of  $\Sigma(t)$  is the symmetric tensor defined as

$$K_{\mu\nu} = -\nabla_\nu n_\mu - n_\nu \gamma^\lambda_\mu \nabla_\lambda (\ln \alpha) = -\frac{1}{2} \mathcal{L}_n \gamma_{\mu\nu}, \quad (2.3)$$

where  $\gamma_{\mu\nu} = g_{\mu\nu} + n_\mu n_\nu$  is the extension of the 3-metric  $\gamma_{ij}$  to the 4-dimensional spacetime, and  $g_{\mu\nu}$  is the 4-metric of that spacetime. By construction,  $K^{\mu\nu} n_\mu = 0$  and we can restrict  $K^{\mu\nu}$  to the 3-dimensional tensor  $K^{ij}$  defined on  $\Sigma \times \Sigma$ . The extrinsic curvature  $K^{ij}$  is then divided into its trace  $K$  and trace-free part  $A^{ij}$ :

$$K^{ij} = A^{ij} + \frac{1}{3} \gamma^{ij} K. \quad (2.4)$$

We treat the matter as a perfect fluid with stress-energy tensor

$$T_{\mu\nu} = (\rho + P) u_\mu u_\nu + P g_{\mu\nu}, \quad (2.5)$$

where  $\rho = \rho_0(1 + \epsilon)$  is the energy density,  $\rho_0$  the baryon density,  $\epsilon$  the specific internal energy,  $P$  the pressure, and  $u_\mu$  the fluid's 4-velocity. For the initial value problem, it is often convenient to consider the following projections of the stress tensor:

$$E = T^{\mu\nu} n_\mu n_\nu, \quad (2.6)$$

$$S = \gamma^{ij} \gamma_{i\mu} \gamma_{j\nu} T^{\mu\nu}, \quad (2.7)$$

$$J^i = -\gamma^i_\mu T^{\mu\nu} n_\nu. \quad (2.8)$$

We then further decompose the metric according to the conformal transformation

$$\gamma_{ij} = \Psi^4 \tilde{\gamma}_{ij}. \quad (2.9)$$

Other quantities have the following conformal transformations:

$$E = \Psi^{-6} \tilde{E}, \quad (2.10)$$

$$S = \Psi^{-6} \tilde{S}, \quad (2.11)$$

$$J^i = \Psi^{-6} \tilde{J}^i, \quad (2.12)$$

$$A^{ij} = \Psi^{-10} \tilde{A}^{ij}, \quad (2.13)$$

$$\alpha = \Psi^6 \tilde{\alpha}. \quad (2.14)$$

$\tilde{A}^{ij}$  is related to the shift and the time derivative of the conformal metric,  $\tilde{u}_{ij} = \partial_t \tilde{\gamma}_{ij}$  by

$$\tilde{A}^{ij} = \frac{1}{2\tilde{\alpha}} \left[ \left( \tilde{\mathbb{L}}\beta \right)^{ij} - \tilde{u}^{ij} \right], \quad (2.15)$$

where  $\tilde{\mathbb{L}}$  is the conformal longitudinal operator whose action on a vector  $V^i$  is

$$\left( \tilde{\mathbb{L}}V \right)^{ij} = \tilde{\nabla}^i V^j + \tilde{\nabla}^j V^i - \frac{2}{3} \tilde{\gamma}^{ij} \tilde{\nabla}_k V^k, \quad (2.16)$$

and  $\tilde{\nabla}$  is the covariant derivative defined with respect to the conformal 3-metric  $\tilde{\gamma}_{ij}$ .

In the 3+1 formalism, the Einstein equations are decomposed into a set of evolution equations for the metric variables as a function of  $t$ , and a set of constraint equations on each hypersurface  $\Sigma(t)$ . The initial data problem consists in providing quantities  $g_{\mu\nu}(t_0)$  and  $K_{\mu\nu}(t_0)$  which satisfy the constraints on  $\Sigma(t_0)$  and represent initial conditions with the desired physical properties (e.g. masses and spins of the objects, initial orbital frequency, eccentricity, etc.). We solve the constraint equations using the Extended Conformal Thin Sandwich (XCTS) formalism York (1999), in which the constraints take the form of five nonlinear coupled elliptic equations. The XCTS equations can be written as

$$2\tilde{\alpha}\left[\tilde{\nabla}_j\left(\frac{1}{2\tilde{\alpha}}(\tilde{L}\beta)^{ij}\right)-\tilde{\nabla}_j\left(\frac{1}{2\tilde{\alpha}}\tilde{u}^{ij}\right)-\frac{2}{3}\Psi^6\tilde{\nabla}^i K-8\pi\Psi^4\tilde{J}^i\right]=0, \quad (2.17)$$

$$\tilde{\nabla}^2\Psi-\frac{1}{8}\Psi\tilde{R}-\frac{1}{12}\Psi^5K^2+\frac{1}{8}\Psi^{-7}\tilde{A}_{ij}\tilde{A}^{ij}+2\pi\Psi^{-1}\tilde{E}=0, \quad (2.18)$$

$$\tilde{\nabla}^2(\tilde{\alpha}\Psi^7)-(\tilde{\alpha}\Psi^7)\left[\frac{1}{8}\tilde{R}+\frac{5}{12}\Psi^4K^2+\frac{7}{8}\Psi^{-8}\tilde{A}_{ij}\tilde{A}^{ij}+2\pi\Psi^{-2}(\tilde{E}+2\tilde{S})\right]=- \Psi^5(\partial_t K-\beta^k\partial_k K). \quad (2.19)$$

We solve these equations for the conformal factor  $\Psi$ , the densitized lapse  $\tilde{\alpha}\Psi^7$  and the shift  $\beta^i$ .  $\tilde{E}$ ,  $\tilde{S}$  and  $\tilde{J}^i$  determine the matter content of the slice. The variables  $\tilde{\gamma}_{ij}$ ,  $\tilde{u}_{ij}=\partial_t\tilde{\gamma}_{ij}$ ,  $K$  and  $\partial_t K$  are freely chosen.

If we work in a coordinate system corotating with the binary,  $\tilde{u}_{ij}=0$  and  $\partial_t K=0$  are natural choices for a quasi-equilibrium configuration. Following earlier work Taniguchi et al. (2007; 2006); Foucart et al. (2008), we also choose to use maximal slicing,  $K=0$ ,

and a conformally flat metric,  $\tilde{\gamma}_{ij} = \delta_{ij}$ . Maximal slicing is a gauge choice that determines the location of the initial data hypersurface in the embedding space time. Conformal flatness is used for computational convenience; rotating black holes are known to be not conformally flat Garat & Price (2000), and so this simplifying assumption should be revisited in the future.

In addition to solving these equations for the metric variables, we must impose some restrictions on the matter. In particular, the stars should be in a state of approximate hydrostatic equilibrium in the comoving frame. This involves solving the Euler equation and the continuity equation. For an irrotational binary, the first integral of the Euler equation leads to the condition

$$h\alpha\frac{\gamma}{\gamma_0} = C, \quad (2.20)$$

where  $C$  is a constant, hereafter referred to as the Euler constant, the enthalpy  $h$  is defined as

$$h = 1 + \epsilon + \frac{P}{\rho_0}, \quad (2.21)$$

and we have introduced

$$\gamma = \gamma_n \gamma_0 (1 - \gamma_{ij} U^i U_0^j), \quad (2.22)$$

$$\gamma_0 = (1 - \gamma_{ij} U_0^i U_0^j)^{-1/2}, \quad (2.23)$$

$$\gamma_n = (1 - \gamma_{ij} U^i U^j)^{-1/2}, \quad (2.24)$$

$$U_0^i = \frac{\beta^i}{\alpha}. \quad (2.25)$$

The 3-velocity  $U^i$  is defined by

$$u^\mu = \gamma_n (n^\mu + U^\mu), \quad (2.26)$$

$$U^\mu n_\mu = 0. \quad (2.27)$$

The choice of  $U^i$ , which is unconstrained in this formalism, is an important component in determining the initial conditions in the neutron star. For irrotational binaries (non-

spinning neutron stars), there exists a potential  $\phi$  such that

$$U^i = \frac{\Psi^{-4} \tilde{\gamma}^{ij}}{h \gamma_n} \partial_j \phi. \quad (2.28)$$

The continuity equation can then be written as a second-order elliptic equation for  $\phi$ :

$$\frac{\rho_0}{h} \nabla^\mu \nabla_\mu \phi + (\nabla^\mu \phi) \nabla_\mu \frac{\rho_0}{h} = 0. \quad (2.29)$$

Under the assumption of the existence of an approximate helicoidal Killing vector  $\xi$  Teukolsky (1998); Shibata (1998), this equation becomes

$$\begin{aligned} \rho_0 \left\{ -\tilde{\gamma}^{ij} \partial_i \partial_j \phi + \frac{h \beta^i \Psi^4}{\alpha} \partial_i \gamma_n + h K \gamma_n \Psi^4 \right. \\ \left. + \left[ \tilde{\gamma}^{ij} \tilde{\Gamma}_{ij}^k + \gamma^{ik} \partial_i \left( \ln \frac{h}{\alpha \Psi^2} \right) \right] \partial_k \phi \right\} \\ = \tilde{\gamma}^{ij} \partial_i \phi \partial_j \rho_0 - \frac{h \gamma_n \beta^i \Psi^4}{\alpha} \partial_i \rho_0. \end{aligned} \quad (2.30)$$

Another simple choice for  $U^i$  is to enforce corotation of the star, i.e.  $U^i = U_0^i$ . This would be the case if neutron star binaries were tidally locked. However, viscous forces in neutron stars are expected to be insufficient to impose tidal locking Bildsten & Cutler (1992), and the neutron star spins probably remain close to their value at large orbital separations.

Once we have obtained  $h$  from the metric and  $U^i$ , the other hydrodynamical variables can be recovered if we close the system by the choice of an equation of state for cold neutron star matter in  $\beta$ -equilibrium,  $P = P(\rho_0)$  and  $\epsilon = \epsilon(\rho_0)$ . Throughout this work, we use a polytropic equation of state,  $P = \kappa \rho_0^\Gamma$ , with  $\Gamma = 2$ . The internal energy,  $\epsilon \rho_0$ , satisfies

$$\epsilon \rho_0 = \frac{P}{\Gamma - 1}. \quad (2.31)$$

The boundary conditions of our system of equations are quite simple. At the outer boundary of the computational domain (which we approximate as “infinity” and is in practice  $10^{10} M_\odot$ ), we require the metric to be Minkowski in the inertial frame, and so in



the corotating frame we have

$$\boldsymbol{\beta} = \boldsymbol{\Omega}_0 \times \mathbf{r} + \dot{a}_0 \mathbf{r}, \quad (2.32)$$

$$\alpha = 1, \quad (2.33)$$

$$\Psi = 1, \quad (2.34)$$

with  $\boldsymbol{\Omega}_0$  the initial orbital frequency of the binary and  $\dot{a}_0$  the initial inspiral rate of the binary. We choose  $\boldsymbol{\Omega}_0 = (0, 0, \Omega_0)$ , with  $\Omega_0$  and  $\dot{a}_0$  as freely specifiable variables that determine the initial eccentricity of the binary.

At the surface of each star, the boundary condition can be easily inferred from the  $\rho_0 = 0$  limit of equation (2.30):

$$\tilde{\gamma}^{ij} \partial_i \phi \partial_j \rho_0 = \frac{h \gamma_n \beta^i \Psi^4}{\alpha} \partial_i \rho_0. \quad (2.35)$$

Finally, we discuss how a first guess for the orbital angular velocity  $\Omega_0$  can be obtained for a non-spinning system. The force balance equation at the centre of the NS is

$$\nabla \ln h = 0. \quad (2.36)$$

Neglecting any infall velocity, this condition guarantees that the binary is in a circular orbit. This is only an approximation as there is really some infall velocity, but this still leads to low eccentricity binaries with  $e \sim 0.01$ . From the integrated Euler equation, we can write this condition as

$$\nabla \ln h = \nabla \left( \ln \frac{\gamma_0}{\alpha \gamma} \right) = 0, \quad (2.37)$$

or, by using the definitions of  $\gamma_0$ , and  $\gamma$ ,

$$\nabla \ln (\alpha^2 - \gamma_{ij} \beta^i \beta^j) = -2 \nabla \ln \gamma. \quad (2.38)$$

If we decompose  $\beta^i$  in its inertial component  $\beta_0^i$  and its comoving component according to

$$\boldsymbol{\beta} = \boldsymbol{\beta}_0 + \boldsymbol{\Omega}_0 \times \mathbf{r} + \dot{a}_0 \mathbf{r}, \quad (2.39)$$

this can be written as a quadratic equation for the orbital angular velocity  $\Omega_0$  (neglecting the dependence of  $\gamma$  on the orbital angular velocity  $\Omega_0$ ). In practice, we solve for  $\Omega_0$  by projecting Eq. (2.38) along the line connecting the center of the two stars.<sup>1</sup>

The exact iterative procedure followed to solve in a consistent manner the constraint equations, the elliptic equations for  $\phi$ , and the algebraic equations for  $h$  (including on-the-fly computation of  $\Omega_0$  and of the constant in the first integral of Euler equation) is detailed in Section 2.3.4.

Once a quasi-equilibrium solution has been obtained by this method, lower eccentricity systems can be generated by modifying  $\Omega_0$  and  $\dot{a}_0$ , following the methods developed by Pfeiffer et al. (2007).

### 2.3.2 Formalism for Spinning Binaries

We will now discuss how to alter the formalism discussed above to incorporate spinning BNS. Although several formalisms have been introduced in the past Marronetti & Shapiro (2003) Baumgarte & Shapiro (2009), we will follow the work of Tichy (2011) Tichy (2011). A first obvious difference is that we can no longer write the velocity solely in terms of the gradient of a potential. Following Tichy, we break the velocity up into an irrotational part, and a new rotational part  $W$ :

$$U^i = \frac{\Psi^{-4} \tilde{\gamma}^{ij}}{h \gamma_n} (\partial_j \phi + W_j), \quad (2.40)$$

where it is natural, although not required, for  $W$  to be divergenceless.

Following the assumptions stated in Tichy (2011), the continuity equation be-

---

<sup>1</sup> Along the other directions, the enthalpy  $h$  is corrected so that force balance is enforced at the center of the star, according to the method described in Foucart et al. (2011)

comes

$$\begin{aligned} \rho_0 \left\{ -\tilde{\gamma}^{ij} \partial_i (\partial_j \phi + W_j) + \frac{h \beta^i \Psi^4}{\alpha} \partial_i \gamma_n + h K \gamma_n \Psi^4 \right. \\ \left. + \left[ \tilde{\gamma}^{ij} \tilde{\Gamma}_{ij}^k + \gamma^{ik} \partial_i \left( \ln \frac{h}{\alpha \Psi^2} \right) \right] (\partial_k \phi + W_k) \right\} \\ = \tilde{\gamma}^{ij} (\partial_i \phi + W_i) \partial_j \rho_0 - \frac{h \gamma_n \beta^i \Psi^4}{\alpha} \partial_i \rho_0. \end{aligned} \quad (2.41)$$

Eq. 3.29 then is the same as in the irrotational case, cf. Eq. 2.30, under the replacement  $\partial_i \phi \rightarrow \partial_i \phi + W_i$ .

Taking the limit  $\rho_0 \rightarrow 0$  in Eq. (3.29) yields the boundary condition at the surface of each star:

$$\tilde{\gamma}^{ij} (\partial_i \phi + W_i) \partial_j \rho_0 = \frac{h \gamma_n \beta^i \Psi^4}{\alpha} \partial_i \rho_0. \quad (2.42)$$

The solution of the Euler equation is no longer as simple as it was previously, in Eq. 2.20. As shown in Tichy(2011)Tichy (2011), the solution is now

$$h = \sqrt{L^2 - (\nabla_i \phi + W_i) (\nabla^i \phi + W^i)}, \quad (2.43)$$

where

$$L^2 = \frac{b + \sqrt{b^2 - 4\alpha^4 ((\nabla_i \phi + W_i) W^i)^2}}{2\alpha^2}, \quad (2.44)$$

and

$$b = (\beta^i \nabla_i \phi + C)^2 + 2\alpha^2 (\nabla_i \phi + w_i) w^i. \quad (2.45)$$

Finally, the method discussed previously of modifying the star's angular velocity is now no longer as simple. The equation is modified to

$$\nabla \ln (\alpha^2 - \gamma_{ij} \beta^i \beta^j) = -2\nabla \ln \Gamma, \quad (2.46)$$

where

$$\Gamma = \frac{\gamma_n \left( 1 - \left( \beta^i + \frac{W^i \alpha}{h \gamma_n} \right) \frac{\nabla_i \phi}{\alpha h \gamma_n} - \frac{W_i W^i}{\alpha^2 \gamma_n^2} \right)}{\sqrt{1 - \left( \frac{\beta^i}{\alpha} + \frac{W^i}{h \gamma_n} \right) \left( \frac{\beta_i}{\alpha} + \frac{W_i}{h \gamma_n} \right)}}. \quad (2.47)$$

Let us now discuss the choice of the spin term,  $W$ . This term is, in principle, freely chosen, and so we must choose it so as to best represent the physical situation at hand - namely a uniform rotation with constant angular velocity. As suggested by Tichy(2011)Tichy (2011) and Tichy(2012)Tichy (2012), a reasonable choice for  $W$  is

$$W^i = \epsilon^{ijk} \omega^j r^k, \quad (2.48)$$

where  $r^k$  is the position vector centered at the star's centre,  $\omega^j$  represents an angular velocity vector and  $\epsilon^{ijk} = \{\pm 1, 0\}$ . This leads to a vector field  $W^i$  with vanishing divergence in the conformal metric  $\tilde{g}_{ij} = \delta_{ij}$ . Alternatively, one might prefer a vector field  $V^i$  with vanishing divergence with respect to the physical metric  $g_{ij} = \Psi^4 \delta_{ij}$ . Owing to the conformal transformation properties of the divergence operator,  $V^i$  is given by

$$V^i = \Psi^{-6} W^i. \quad (2.49)$$

Here, we generally use  $W^i$  as we have found that it leads to initial data which is closer to being in equilibrium, as we will further discuss in section 2.5.5.

### 2.3.3 Solving the elliptic equations

In the previous sections, we have reduced the Einstein constraints, Eqs. (3.17)–(3.19), as well as the continuity equation (3.29) to elliptic equations. We solve these equations with the multi-domain pseudo-spectral elliptic solver developed in Pfeiffer et al. (2003), as modified in Foucart et al. (2008) for matter. The computational domain is subdivided into individual subdomains as indicated in Fig. 2.1: The region near the center of each star is covered by a cube, overlapping the cube is a spherical shell which covers the outer layers of the star. The outer boundary of this shell is deformed to conform to the surface of the star. This places all surfaces at which the solution is not smooth at a subdomain-boundary, which preserves the exponential convergence of spectral methods. Another spherical shell surrounds each star. The inner shells representing the stars and their

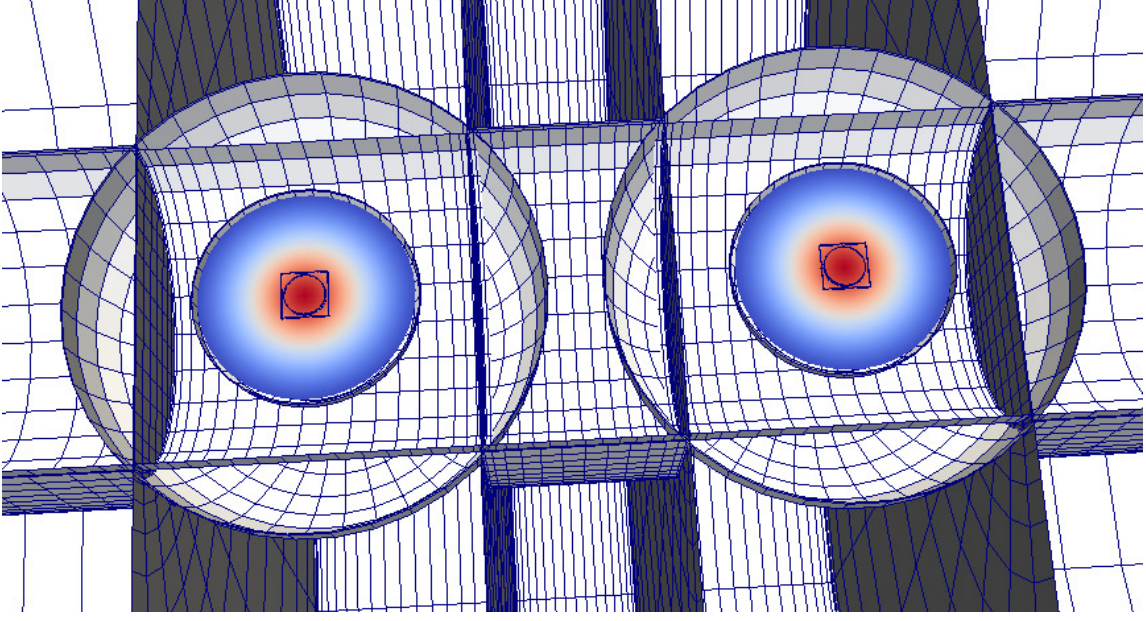


Figure 2.1: Visualization in the x-y plane of the domain decomposition used in our initial data solve. The colour map represents the density of the stars.

vicinity are embedded into a structure of five concentric cylinders with three rectangular blocks along the axis connecting the centers of the neutron stars, which overlap the inner spherical shells. The cylinders/blocks in turn are overlapped at large radius by one further spherical shell centered half-way between the two neutron stars. Using an inverse radial mapping, the outer radius of the outer sphere is placed at  $10^{10}$ .

All variables are decomposed on sets of basis functions depending on the subdomain. The resolution of each domain (i.e., the number of collocation points used) is chosen at the start of the initial data solve, and then subsequently modified several times using an adaptive procedure described below. In this paper, when discussing the total resolution of the domain, we use the notation

$$N^{1/3} = \left( \sum N_i \right)^{1/3}, \quad (2.50)$$

with  $N_i$  the number of collocation points in the  $i$ th subdomain.  $N^{1/3}$  is thus the cube root of the total number of collaction points in all subdomains.

### 2.3.4 Construction of quasi-equilibrium initial data

Construction of initial data for rotating binary neutron stars begins with selecting the physical properties of the system: the equation of state of nuclear matter, the coordinate separation  $d$  between the neutron stars, the baryon masses  $M_1^b$  and  $M_2^b$  of the two stars, and their spin vectors  $\boldsymbol{\omega}_{\text{rot},1}$  and  $\boldsymbol{\omega}_{\text{rot},2}$ . We also choose the orbital angular frequency  $\Omega_0$  and the initial inspiral rate  $\dot{a}_0$ .

We generally begin by setting  $\Omega_0$  to the value for the orbital frequency of a similar ir-rotational BNS (where  $\Omega_0$  is determined by the condition of quasi-circularity, Eq. (2.36)), and  $\dot{a}_0 = 0$ . These values are then adjusted following the eccentricity reduction method developed by Pfeiffer et al. (2007). Finally, we use a flat conformal metric,  $\tilde{\gamma}_{ij} = \delta_{ij}$ , and maximal slicing,  $K = 0$ .

Once all these quantities are fixed, we need to solve self-consistently Eqs. (3.17)–(3.19) for the Einstein-constraints, the continuity equation Eq. (3.29), while simultaneously satisfying conditions to enforce the desired masses of the stars. To do so, we follow an iterative procedure developed originally for black hole-neutron star binaries Foucart et al. (2012).

First, we choose initial guesses for the conformal metric and hydrodynamical variables, using an analytical superposition of two isolated boosted neutron stars.

We then obtain constraint-satisfying initial conditions by applying the following iterative procedure, where  $n$  represents the iteration number:

1. Solve the nonlinear XCTS system for the set of metric variables  $X = (\beta^i, \Psi, \alpha\Psi)$ , assuming fixed values of the conformal source terms  $(\tilde{E}, \tilde{S}, \tilde{J}^i)$ . The new value  $X^{n+1}$  of the metric variables is obtained from their old value  $X^n$  and, following the relaxation scheme used in Foucart et al. (2008), the solution of the XCTS equations  $X^*$ , using

$$X^{n+1} = 0.3X^* + 0.7X^n. \quad (2.51)$$

2. Locate the surface of each star. Representing the surface in polar coordinates centered on each star as  $R_s^n(\theta, \phi)$ , we determine  $R_s^n$  to satisfy Foucart et al. (2008)  $h(R_s^n(\theta, \phi), \theta, \phi) = 1$ . To ensure that the grid-boundary  $R_b$  converges to the surface of the star, we occasionally modify the numerical grid such that  $R_b(\theta, \phi) = R_s^n(\theta, \phi)$ . Because this requires a re-initialization of the elliptic solver, the grid is only modified if the stellar surface has settled down, specifically, if

$$\|R_s^n - R_s^{n-1}\| < 0.1\|R_s^n - R_b\|. \quad (2.52)$$

Here  $\|\cdot\|_2$  denotes the L2-norm over the surface.

3. For each neutron star, fix the constant in Euler's first integral so that the baryon mass of the neutron star matches the desired value. We compute the baryon mass as a function of the Euler constant  $C$  through

$$M_{\text{NS}}^b = \int_{\text{NS}} \rho_0 \Psi^6 \sqrt{\frac{1}{1 - \gamma_{ij} U^i U^j}} dV, \quad (2.53)$$

and utilize the secant method to drive the mass to the desired value.

4. If desired, adjust the orbital frequency to ensure force-balance at the center of each star by solving Eq. (2.38). This step is skipped if the orbital frequency is fixed through iterative eccentricity removal, cf. Sec. 2.5.2.
5. Solve the elliptic equation for the velocity potential  $\phi$ , and obtain the next guess for  $\phi$  using the same relaxation method shown in Eq. 3.49.
6. Check whether all equations are satisfied to the desired accuracy. If yes, proceed. If no, return to Step 1.
7. Compute the truncation error of the current solution by examining the spectral expansion of the XCTS variables. If this truncation error is undesirably large (typically, if it is  $> 10^{-9}$ ), then adjust the number of grid-points in the domain-decomposition and return to Step 1. The adjustment is based on the desired target

truncation error and the measured convergence rate of the solution, cf. Szilágyi (2014).

### 2.3.5 Quasi-Local Angular Momentum

The goal of the present paper is to construct spinning BNS initial data and to evolve it. Therefore, we need diagnostics to measure the NS spin, for which we use techniques originally developed for black holes. It is common to discuss the spins of black holes in terms of their dimensionless spin  $\chi$ ,

$$\chi = \frac{S}{M^2}. \quad (2.54)$$

Here,  $S$  is the angular momentum of the black hole, and  $M$  is its Christodoulou mass Christodoulou (1970),

$$M^2 = M_{\text{irr}}^2 + \frac{S^2}{4M_{\text{irr}}^2}. \quad (2.55)$$

The irreducible mass  $M_{\text{irr}}$  is defined based on the area of the hole's apparent horizon,  $M_{\text{irr}} = \sqrt{A/16\pi}$ . The angular momentum is computed with a surface integral over the apparent horizon Brown & York (1993); Ashtekar et al. (2001); Ashtekar & Krishnan (2003),

$$S = \frac{1}{8\pi} \oint_{\mathcal{H}} \phi^i s^j K_{ij} dA \quad (2.56)$$

where  $\mathcal{H}$  is the black hole's apparent horizon,  $s^j$  is the outward-pointing unit-normal to  $\mathcal{H}$  within the  $t = \text{const}$  hypersurface, and  $\phi^i$  is an azimuthal vector field tangent to  $\mathcal{H}$ . For spacetimes with axisymmetry,  $\phi^i$  should be chosen as the rotational Killing vector. In spacetimes without an exact rotational symmetry (e.g. the spacetime of a binary black hole system), one substitutes an approximate Killing vector Cook & Whiting (2007); Lovelace et al. (2008) (AKV). Ref. Lovelace et al. (2008) introduces a minimization principle to define  $\phi^i$ , resulting in an Eigenvalue problem. The three eigenvectors with the lowest eigenvalues (i.e. smallest shear) are taken and used to compute the three components of the spin.



In this paper, we explore the application of quasi-local spin measures to neutron stars. In the absence of apparent horizons  $\mathcal{H}$ , we need to choose different surface(s) to evaluate Eq. (2.56).

When constructing initial data, the stellar surface  $\mathcal{S}$  is already determined, so one obvious choice is to integrate over the stellar surface  $\mathcal{S}$ . To estimate the ambiguity in quasi-local spin, we furthermore compute  $S$  by integrating over coordinate spheres with radii ranging from just outside  $\mathcal{S}$  to larger by about 70%. During the evolution, the stars change shape and may even loose mass in tidal tails. Because of these complications, the SpEC evolution code does not track the location of the stellar surface during the evolution, and we shall only monitor  $S$  on coordinate spheres.

It is useful to compute a dimensionless spin  $\chi$ , for instance, for post-Newtonian comparisons. In the absence of a horizon, Eq. (2.55) is meaningless and we need a different choice for the mass-normalization. Instead, we normalize by each star's ADM mass,  $M_{\text{ADM}}$ , i.e.

$$\chi \equiv \frac{S}{M_{\text{ADM}}^2}. \quad (2.57)$$

The ADM mass is determined by computing the ADM mass of an equilibrium configuration of a single uniformly rotating polytrope in isolation with the same baryon mass and angular momentum as those measured in our binary systems.

The results of the quasi-local spin measures are described in section 2.4.4, which shows that this procedure is numerically robust.

Finally, let us discuss, from an order of magnitude perspective, how the star's dimensionless spin is related to its more commonly used physical properties. We start with the Newtonian relation  $S = 2\pi I/P$  between angular momentum  $S$ , moment of inertia  $I$ , and rotational period  $P$ . Writing further  $I = f R^2 M$ , with the dimensionless constant

$f$  depending on the stellar density profile, we have

$$\begin{aligned}\chi &\sim \frac{2\pi c}{G} \frac{f R^2}{PM} \\ &= 0.48 \left(\frac{f}{0.33}\right) \left(\frac{R}{12\text{km}}\right)^2 \left(\frac{M}{1.4M_\odot}\right)^{-1} \left(\frac{P}{1\text{ms}}\right)^{-1}.\end{aligned}\tag{2.58}$$

The factor  $c/G$  arises from the transition to geometric units.

This –quite simplistic– estimate shows that millisecond pulsars will have appreciable dimensionless spin  $\chi$ . Centrifugal breakup of rapidly rotating neutron stars happens at a dimensionless spin in the range  $0.65 - 0.70$  Lo & Lin (2011), with only small dependence on the equation of state and neutron star mass. Ansorg et al (2003) studied in detail  $\Gamma = 2$  polytropes, the equation of state we use here. Ref. Ansorg et al. (2003) finds a dimensionless spin at mass-shedding of  $\chi = 0.57$ .

## 2.4 Initial Data Results

In this section, we will demonstrate that our code can robustly construct constraint-satisfying initial data for BNS systems with arbitrary spins. As discussed in section 2.3.4, our code consists of a solver that runs for a number of iterations at constant resolution, and then the resolution is increased and this process restarts. We will therefore demonstrate that appropriate quantities converge with both the iterations of iterative scheme described above in Section 2.3.4 and with resolution as the resolution increases.

### 2.4.1 Convergence of the Iterative Procedure

At each step of the iterative procedure, the Euler constant of each star is modified to achieve a desired stellar baryon mass, based on the current matter distribution inside the star. We expect that the Euler constant converges during the iterations at a fixed resolution. Figure 2.2 shows the behavior of the Euler Constant during iterations at the lowest initial data resolution, R0. We show three runs of interest, one with large aligned

Name	$M_{\text{NS}}^b$	$\omega$	$D_0$	$\Omega_0 \times 10^3$	$\dot{a}_0 \times 10^5$	$M_{\text{ADM}}$	$\vec{\chi}$
S.4z	1.7745	$0.01525\hat{z}$	47.2	5.09594	-1.75	1.648	$0.3765\hat{z}$
S-.05z	1.7745	$-0.00273\hat{z}$	47.2	5.11769	-1.71	1.640	$-0.05018\hat{z}$
S.4x	1.7745	$0.01525\hat{x}$	47.2	5.10064	-2.36	1.648	$0.3714\hat{x}$

Table 2.1: Parameters for the initial data sets used in testing the initial data solver:  $M_{\text{NS}}^b$  and  $\omega^i$  are baryon mass and rotational parameter for either neutron star (the same values are used);  $D_0$ ,  $\Omega_0$  and  $\dot{a}_0$  represent coordinate separation between the centers of the stars, the orbital frequency, and the radial expansion;  $\vec{\chi}$  is the dimensionless spin vector computed from the initial data set. In each case we use a polytropic equation of state,  $P = \kappa \rho_0^\Gamma$ , with  $\Gamma = 2$  and  $\kappa = 123.6$ .

spins (S.4z), one with large precessing spin (S.4x), and one with small anti-aligned spins (S-.05z). The properties of these configurations are shown in table 2.1. In all three cases we see agreement between neighboring iterations at the  $10^{-5} - 10^{-6}$  level by the end of iterating at this resolution. At the highest resolutions, these differences are down to, typically, the  $10^{-9} - 10^{-10}$  level. This can be compared to Fig. 3 of Gourgoulhon et al. (2001). Although not shown here, other free quantities converge similarly to the Euler constant.

### 2.4.2 Convergence of the Solution

Having established that our iterative procedure converges as intended, we now turn our attention to the convergence of the solution with resolution. To demonstrate it, we will look at the Hamiltonian and momentum constraints, and the differences between measured physical quantities - the ADM energy and ADM angular momentum, and the surface fitting coefficients of the stars. As our initial data representation is fully spectral, we expect that these quantities should converge exponentially with resolution. Note that when we discuss the value of a quantity at a certain resolution, we are referring to the

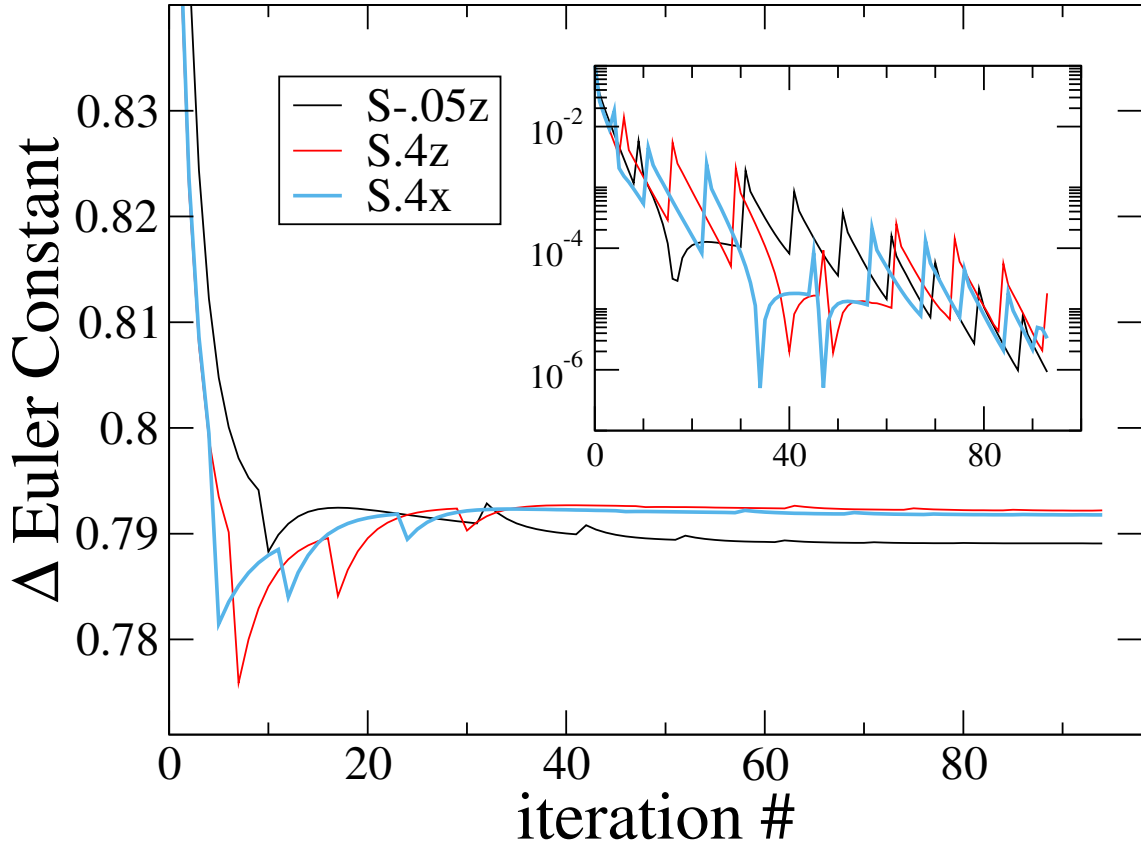


Figure 2.2: Convergence of the Euler constant during iteration at the lowest resolution R0. The inset shows the difference between values at subsequent iterations.

value of that quantity after the final iterative step at that resolution.

Figure 3.4 shows the convergence of the Hamiltonian constraint and the Momentum constraint for our three runs of interest. These are computed during the last iterative solve at each resolution. The data plotted are computed as

$$H = \left\| \frac{R_\Psi}{8\Psi^5} \right\|, \quad (2.59)$$

$$M = \left\| \frac{R_\beta}{2\alpha\Psi^4} \right\|. \quad (2.60)$$

Here  $R_\Psi$  and  $R_\beta$  denote the residuals of Eqs. (3.18) and (3.17), respectively, and  $\|\cdot\|$  represents the root-mean-square value over grid-points of the entire computational grid. This plot demonstrates that our initial data solver converges exponentially with resolution, even for very high spins, which gives confidence that we are indeed correctly solving the Einstein Field Equations.

The surface of the star is represented by a spherical harmonic expansion:

$$R_s(\theta, \phi) = \sum_{l,m}^{l_{\max}, m_{\max}} c_{lm} Y_{lm}(\theta, \phi), \quad (2.61)$$

where  $l_{\max} = m_{\max} = 11$ , unless stated otherwise. The stellar surface is located by finding a constant enthalpy surface, cf. Sec. 2.3.4, and the spherical subdomains that cover the star are deformed to conform to  $R_s(\theta, \phi)$ . To establish convergence of the position of the stellar surface we introduce the quantity

$$\Delta c(i) = \frac{1}{l(l+1)} \sqrt{\sum_{l,m}^{l_{\max}, m_{\max}} (c_{lm}(i) - c_{lm}(N))^2}. \quad (2.62)$$

Here  $i$  refers to the  $i^{\text{th}}$  resolution in the initial data, and  $N$  refers to the final resolution. Figure 2.4 plots  $\Delta c(i)$  vs. resolution. The surface location converges exponentially to better than  $10^{-8}$ .

Finally, we assess the overall convergence of the solution through the global quantities  $E_{\text{ADM}}$  and  $|J_{\text{ADM}}^i|$ . The surface integrals at infinity in these two quantities are recast using

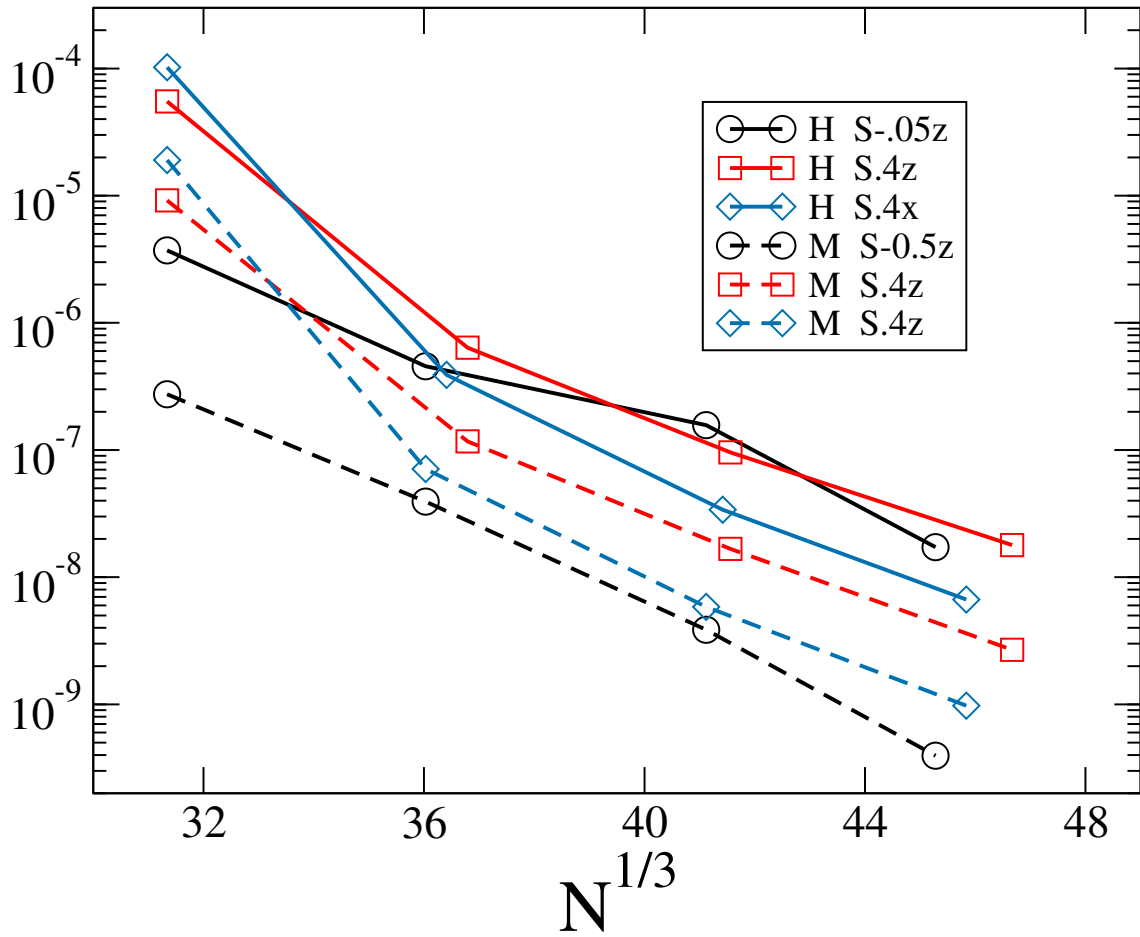


Figure 2.3: Hamiltonian and Momentum constraints as a function of resolution  $N$ . We see exponential convergence in all cases.

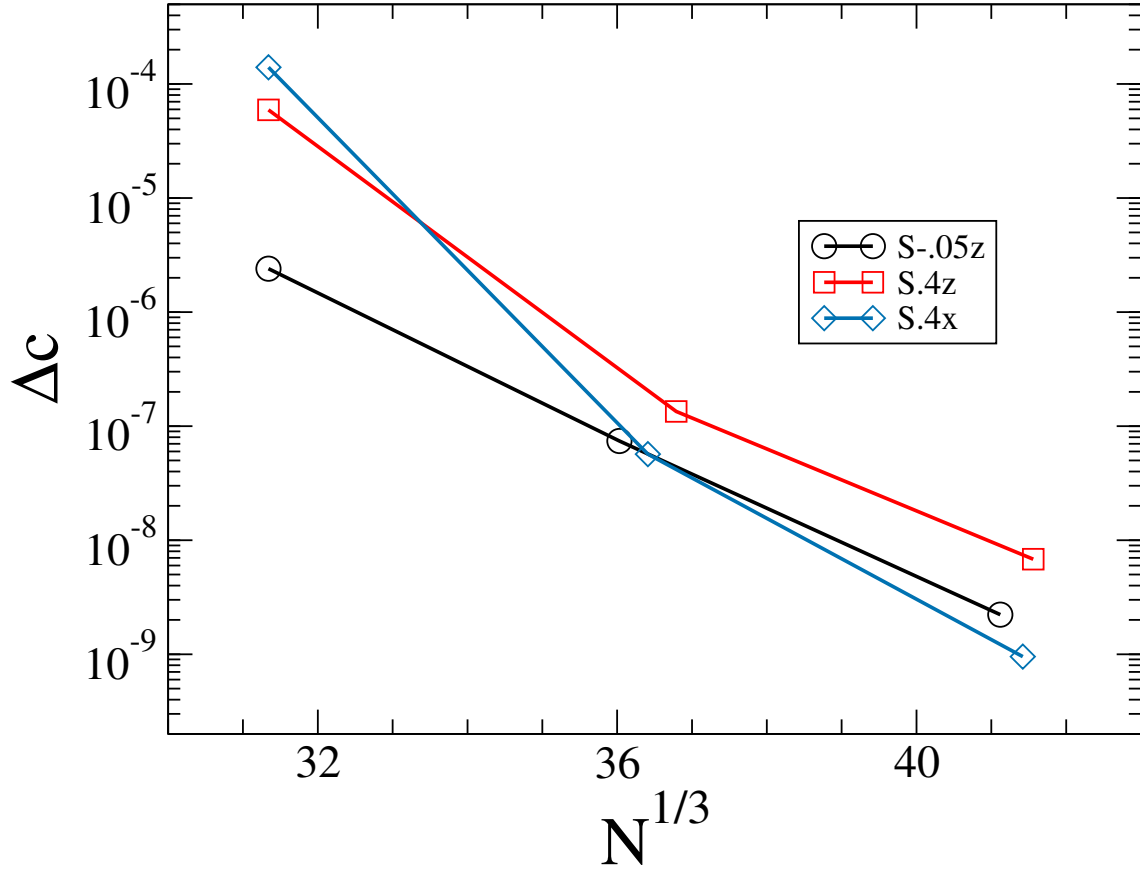


Figure 2.4: Convergence of the location of the stellar surface. Plotted is  $\Delta c$  as defined in Eq.( 2.62), for three representative configurations.

Gauss' law (cf. Foucart et al. (2008)):

$$\begin{aligned} E_{\text{ADM}} &= -\frac{1}{2\pi} \oint_{S_\infty} \delta_j^i \partial_i \Psi dS_j \\ &= -\frac{1}{2\pi} \oint_S \delta_j^i \partial_i \Psi dS^j + \frac{1}{2\pi} \int_{\mathcal{V}} \delta^{ij} \partial_i \partial_j \Psi dV, \end{aligned} \quad (2.63)$$

and

$$\begin{aligned} J_{\text{ADM}}^z &= \frac{1}{8\pi} \oint_{S_\infty} (xK^{yj} - yK^{xj}) dS_j \\ &= \frac{1}{8\pi} \oint_S (xK_{yi} - yK_{xi}) \delta^{ij} \Psi^2 dS_j. \end{aligned} \quad (2.64)$$

Here  $\mathcal{V}$  is the volume outside  $S$ , and the integrals are evaluated in the flat conformal space. To obtain the other components of  $J_{\text{ADM}}^i$ , cyclically permute the indices x,y,z. We define the quantities  $\Delta E$  and  $\Delta J$  as the absolute fractional difference in these quantities between the current resolution and the next highest resolution. These are plotted in figure 2.5. In general, we find agreement at the  $10^{-7} - 10^{-8}$  level by the final resolution.

### 2.4.3 Convergence of the quasi-local spin

We now turn to the angular momentum of the neutron stars, as measured with quasi-local angular momentum integrals on the stellar surface. We will discuss dimensionless spins  $\chi$ , which depend on two distinct numerical resolutions: First, the resolution of the 3-dimensional grid used for solving the initial value equations. This resolution is specified in terms of  $N$ , the total number of grid-points. Second, the resolution used when solving the eigenvalue problem for approximate Killing vectors on the 2-dimensional surface, as given by  $L$ , the expansion order in spherical harmonics of the surface-parameterization  $r_S(\theta, \phi) = \sum_{l=0}^L \sum_m r_{lm} Y^{lm}(\theta, \phi)$ .

Throughout this paper, we use  $L = 11$ . The top panel of Fig. 2.6 shows convergence of  $\chi$  with grid-resolution  $N$ , at fixed  $L = 11$ . We find near exponential convergence.

The influence of our choice  $L = 11$  is examined in the lower panel by computing the quasi-local spin at lower resolution  $L = 8$  and at higher resolution  $L = 14$ . Changing



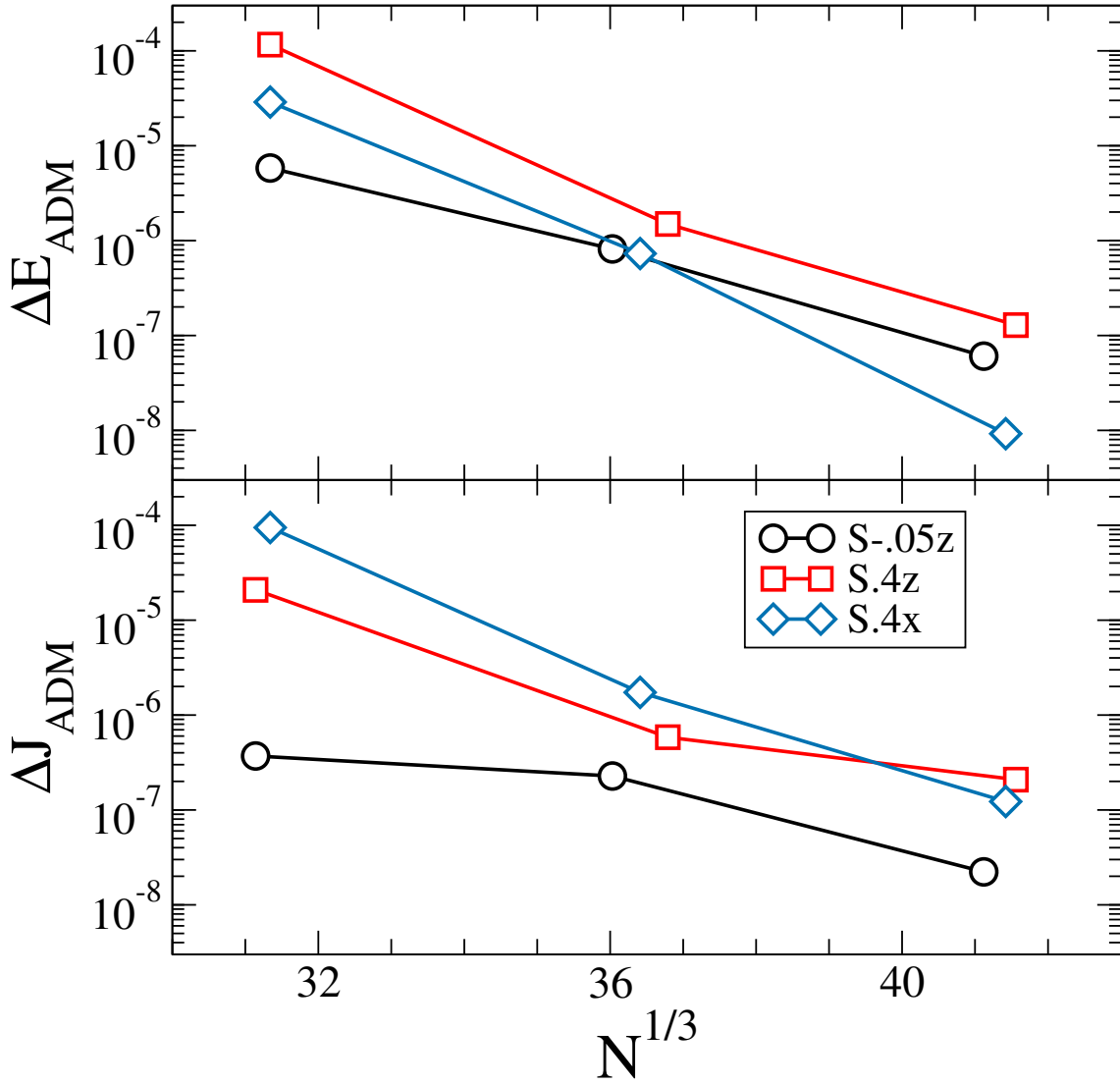


Figure 2.5: Convergence of ADM-energy and the magnitude of the ADM-angular momentum. Shown are the fractional differences between neighboring resolutions, as a function of the lower resolution.

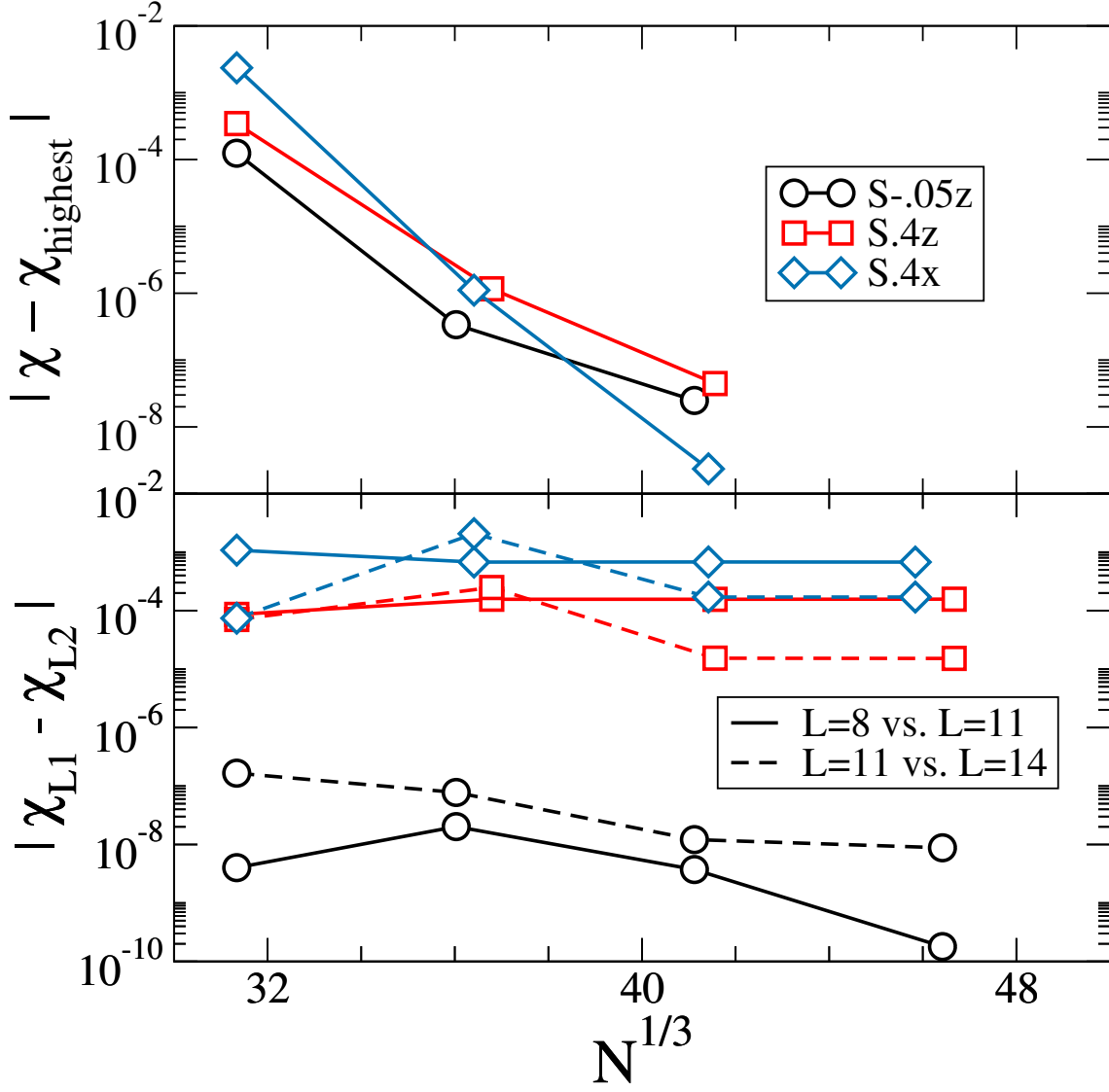


Figure 2.6: Convergence of the quasi-local spin computation. **Top panel:** difference of spin computed at resolution  $N$  with the spin computed at the highest resolution. **Bottom panel:** Difference between spins computed at different resolution  $L$  of the spin-computation. For S-.5z, we achieve an accuracy of  $\sim 10^{-7}$ , whereas for S.4z and S.4x, the accuracy is  $\sim 10^{-4}$  due to finite  $L$ .

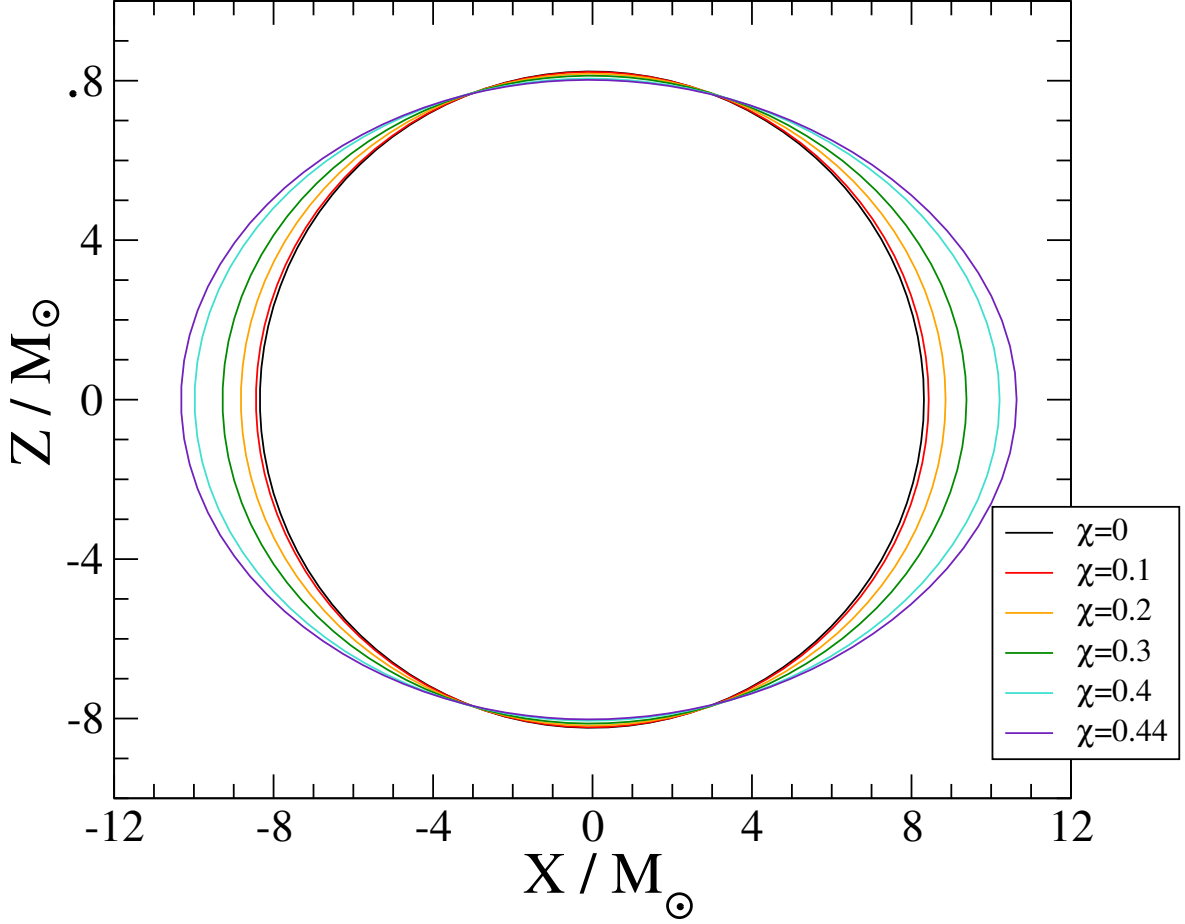


Figure 2.7: Stellar cross-sections in the  $X$ - $Z$  plane for a series of different spins, aligned with the  $\hat{z}$  axis, demonstrating that they bulge at the equator in the expected way with increasing spin.

$L$  impacts  $\chi$  by  $\sim 10^{-8}$  for the low-spin case **S-.05z**, and by  $\sim 10^{-4}$  for the high-spin cases **S.4z** and **S.4x**. For the high-spin cases, the spin measurement is convergent with increasing  $L$ , and the finite value of  $L$  dominates the error budget. For the low-spin case, numerical truncation error dominates the error budget and convergence with  $L$  is not visible. High NS spin leads to a more distorted stellar surface, and so a fixed  $L = 11$  yields a spin result of lower accuracy. However, in all cases the numerical errors of our spin measurements are still negligible for our purposes.

### 2.4.4 Quasi-local Spin

As discussed in section 2.3.5, we use a quasi-local spin to define the angular momentum carried by each neutron star. To our knowledge, this is the first application of this method to neutron stars in binaries.

In this section, we explore properties of the rotating BNS initial datasets and the employed quasi-local spin diagnostic.

To explore the spin-dependence of BNS initial data sets, we construct a sequence of equal-mass, equal-spin BNS binaries, with spins parallel to the orbital angular momentum. We fix the initial data parameters  $M_{\text{NS}}^b$ ,  $D_0$ ,  $\Omega_0$  and  $\dot{a}_0$  to their values for a configuration that we will also evolve below (specifically, **S.4z - Ecc1**)

Figure 2.7 shows cross-sections through one of the neutron stars in the xz-plane, i.e. a plane orthogonal to the orbital plane which is intersecting the centers of both stars. With increasing spin, the stars develop an increasing equatorial bulge, an expected consequence of centrifugal forces.

Figure 3.8 presents the dimensionless spin of either neutron star as a function of  $\omega$ .  $\chi$  increases monotonically with the rotation parameter  $\omega$ . The spin  $\chi$  increases linearly with  $\omega$  for small  $\omega$ . For larger  $\omega$ , the dependence steepens, as the increasing equatorial radius of the stars increase the moment of inertia Worley et al. (2008).

For  $\omega = 0.01625M_{\odot}^{-1}$  we achieve  $\chi = 0.432$ , the largest spin we are able to construct. This is reasonably close to the theoretical maximum value for  $\Gamma = 2$  polytropes,  $\chi \sim 0.57$  Ansorg et al. (2003). Above  $\omega = 0.01625M_{\odot}^{-1}$ , the initial data code fails to converge. The steepening of the  $\chi$  vs.  $\omega$  curve is reminiscent of features related to non-uniqueness of solutions of the extended conformal thin sandwich equations Lovelace et al. (2008); Pfeiffer & York Jr. (2005); Baumgarte et al. (2007); Walsh (2007), and it is possible that our failure to find solutions originates in an analogous break-down of the uniqueness of solutions of the constraint equations.

While the focus of our investigation lies on rotating NS, we note that for  $\omega = 0$  our

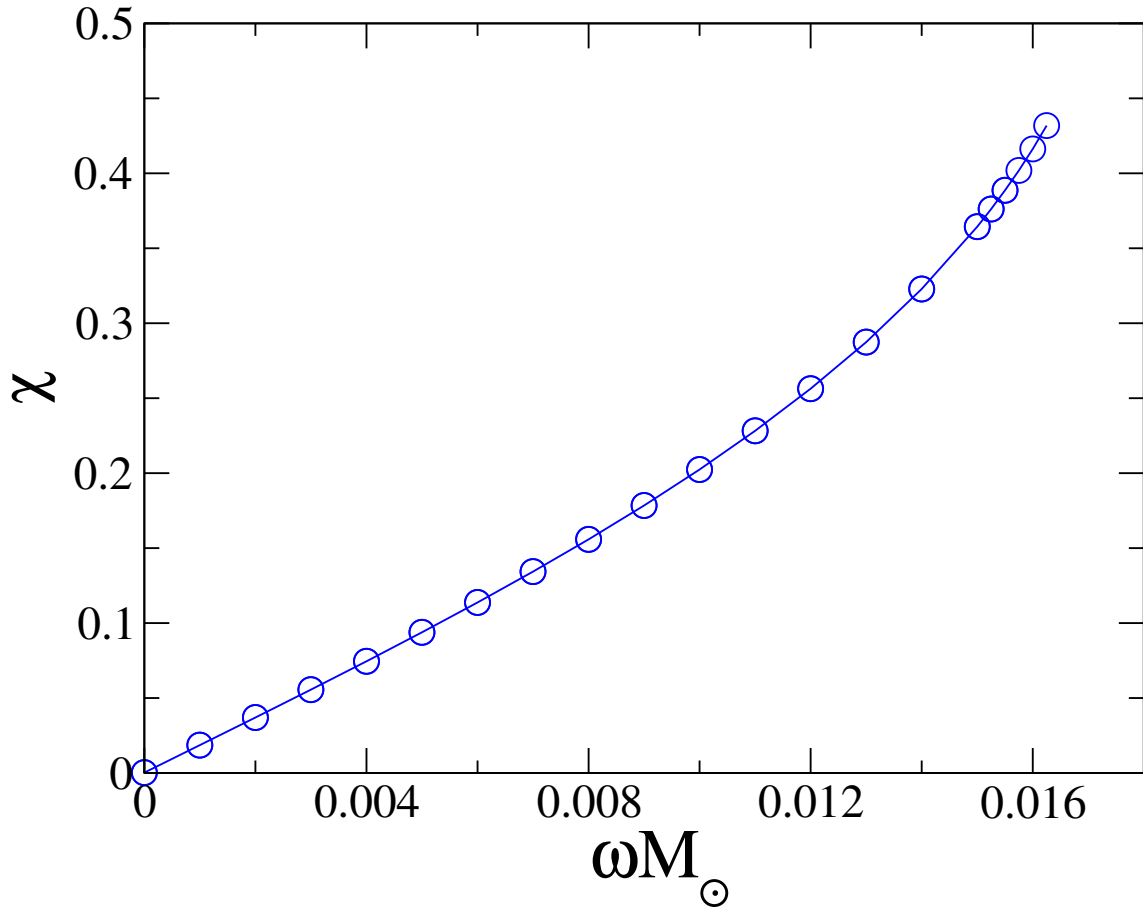


Figure 2.8: Dimensionless angular momentum  $\chi$  as a function of  $\Omega$  for a series of spin-aligned initial data sets with the same physical parameters as our runs of interest. We see, as expected, a linear relation between  $\chi$  and  $\Omega$  at low-spins, which eventually becomes non-linear at higher spins.

data-sets reduce to the standard formalism for irrotational NS. For  $\omega = 0$ , we find a quasi-local spin of the neutron stars is  $\chi = 2 \times 10^{-4}$ . This is the first rigorous measurement of the residual spin of irrotational BNS. Residual spin is, for instance, important for the construction and validation of waveform models for compact object binaries. The analysis in Ref. Boyle et al. (2007) indicates that spins of order  $10^{-4}$  lead to a dephasing of about 0.01 radians during the last dozen of inspiral orbits. This value is significantly smaller than the phase accuracy obtained by current BNS simulations, and so the residual spin is presently not a limiting factor for studies like Bernuzzi et al. (2015); Baiotti et al. (2011); Baiotti et al. (2010).

Finally, we demonstrate that the surface on which we compute the quasi-local spin, does not significantly impact the spin we measure: We choose coordinate spheres centered on the neutron star with radius  $R$ , and compute the quasi-local spin using these surfaces, rather than the stellar surface.

In Fig. 2.9, we plot the spin measured on various  $R = \text{const}$  surfaces, for three different values of  $\omega$ , from the same sequences shown in Fig. 3.8.

The circles denote spins extracted on coordinate spheres. The asterisks indicate the spins computed on the stellar surface. The asterisk is plotted at  $R = R_{\text{eq}}$ , the equatorial radius of the neutron star under consideration. We find good agreement between spins extracted on coordinate spheres and the spin extracted on the stellar surface, as long as  $R \geq R_{\text{eq}}$ . The maximum disagreement is seen in the high spin curve, where the two spins differ by  $\sim 10^{-2}$ .

For  $R < R_{\text{eq}}$ , the coordinate extraction sphere intersects the outer layers of the neutron star and no longer encompasses the entire matter and angular momentum of the star. Therefore,  $\chi(R)$  shows a pronounced decline for  $R < R_{\text{eq}}$  for each of the three initial-data sets considered in Fig. 2.9. For  $R > R_{\text{eq}}$ ,  $\chi(R)$  continues to increase slightly, for instance, for the middle curve,  $\chi(R = 9) = 0.202$  whereas  $\chi(R = 11) = 0.204$ .

In summary, Fig. 2.9 shows that the quasi-local spin extracted on coordinate spheres can serve as a good approximation of the quasi-local spin extracted on the stellar surface

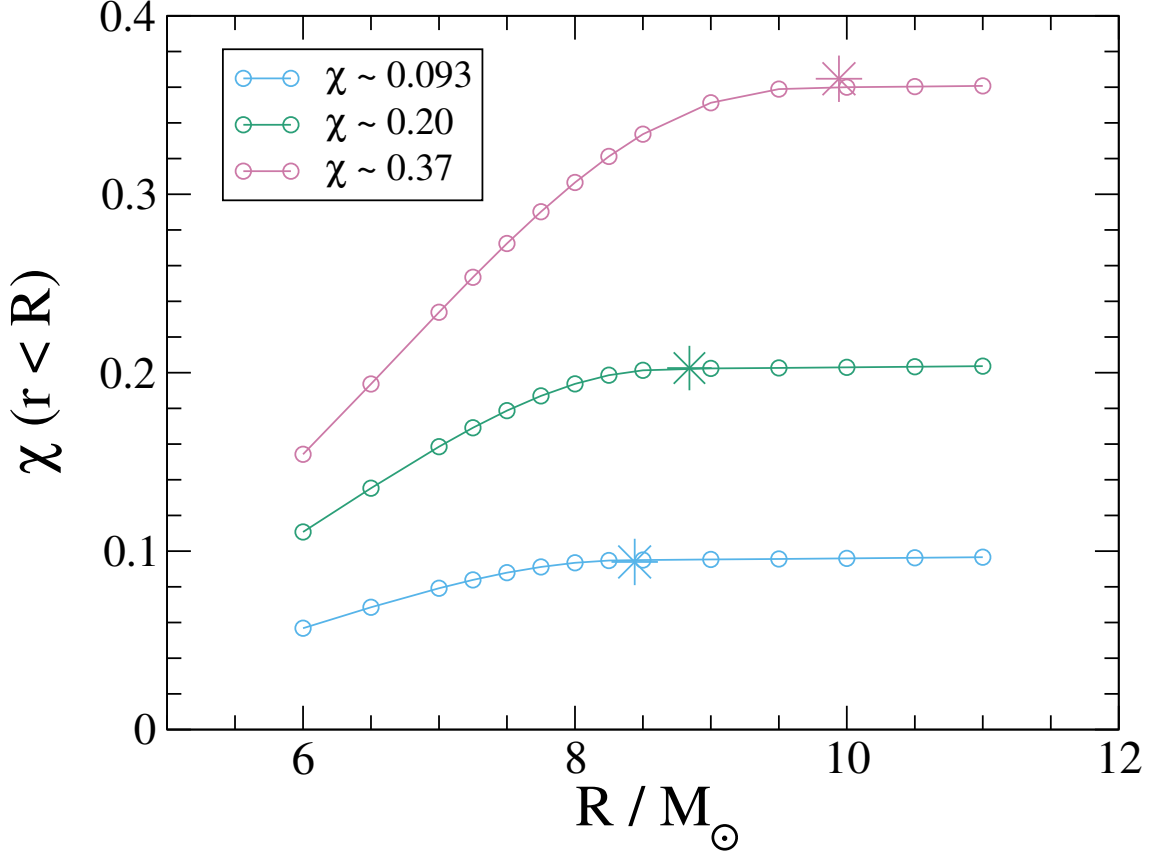


Figure 2.9: Dimensionless spin  $\chi$  measured on coordinate spheres with radius  $R$  for three different aligned spin BNS systems. The asterik denotes the spin measured on the (non-spherical) stellar surface. Circles to the right of the asterik represent coordinate spheres entirely outside the neutron star, and circles on the left of the asterik indicate spin measurement surfaces that intersect the star or are entirely located inside the star.

(as long as the coordinate sphere is outside the star, of course).

This is important because during evolutions of the binary, we do not track the surface of the star. Instead, we will compute the spin on coordinate spheres, similarly to Fig. 2.9.

## 2.5 Evolution Results

We now evolve the three configurations discussed in Sec. 2.4. As indicated in Table 2.1, all three configurations are equal-mass binaries, with individual ADM masses  $M_{\star}$  (in

Name	$k$	$e$	$\vec{\chi}$	$f_0(Hz)$	$N_{\text{orb}}$	$t_f(\text{ms})$
S.4z	0,1,2	$\lesssim 0.001$	$0.381\hat{z}$	167.7	11.8	56.0
S-.05z	0,1,2	0.0006	$-0.050\hat{z}$	165.4	12.5	56.3
S.4x	0,1	$\lesssim 0.002$	$0.375\hat{x}$	164.8	9.1	45.7

Table 2.2: Information about our three evolutions.  $k$  indicates the numerical resolutions on which a simulation is performed,  $e$  indicates the smallest achieved orbital eccentricity.  $\vec{\chi}$  and  $f_0$  are the dimensionless spins at  $t = 0$  and the initial orbital frequency. Finally,  $N_{\text{orb}}$  and  $t_f$  represent the number of orbits the configuration was evolved for, and the evolution time.

isolation) of  $1.64M_\odot$  or  $1.648M_\odot$  at initial separation of  $D = 47.2M_\odot$ , and using a polytropic equation of state with  $\Gamma = 2.0$  and  $\kappa = 123.6$ . Both stars have equal spins, and the three configurations differ in spin magnitude and spin direction. Configuration S-0.05z has spin-magnitudes  $\sim 0.05$  anti-aligned with the orbital angular momentum, and the configurations S.4z and S.4x have spin magnitudes near 0.4, along the z-axis and x-axis, respectively.

Each configuration is evolved through  $\gtrsim 10$  orbits, into the late-inspiral. In this paper we focus on the inspiral of the neutron stars. Table 2.2 summarizes parameters for these runs.

### 2.5.1 Evolution Code

In our evolution code, SpEC Buchman et al. (2012); Lovelace et al. (2012); M. A. Scheel, M. Boyle, T. Chu, L. E. Kidder, K. D. Matthews and H. P. Pfeiffer (2009); Kidder et al. (2000); Lindblom et al. (2006); Scheel et al. (2006); Szilágyi et al. (2009); Lovelace et al. (2011); Hemberger et al. (2013); Ossokine et al. (2013), we use a mixed spectral – finite-difference approach to solving the Einstein Field Equations coupled to general relativistic hydrodynamics equations. The equations for the space-time metric,  $g_{\mu\nu}$  are solved on a spectral grid, while the fluid equations are solved on a finite difference grid, using a



high-resolution shock-capturing scheme. We use a WENO Jiang & Shu (1996); Liu et al. (1994) reconstruction method to reconstruct primitive variables, and an HLL Riemann solver A. Harten (1983) to compute numerical fluxes at interfaces. Integration is done using a 3rd order Runge-Kutta method with an adaptive stepsize. We interpolate between the hydro and spectral grids at the end of each full time step, interpolating in time to provide data during the Runge-Kutta substeps (see Duez et al. (2008); Foucart et al. (2012); Foucart et al. (2013); Muhlberger et al. (2014) for a more detailed description of the method).

Each star is contained in a separate cubical finite difference grid that does not overlap with that of the other star. The sides of the grids are initially 1.25 times the stars' diameters. We use grids that contain  $97^3$ ,  $123^3$  and  $155^3$  points for resolutions  $k = 0, 1, 2$ , respectively<sup>2</sup>. These resolutions correspond to linear grid-spacing of 340 m, 268 m and 213 m respectively for the **S.4z** case. The precessing evolution **S.4x** uses similar grid-spacing, whereas the anti-aligned run **S-.05z** has a slightly smaller grid-spacing because the stars themselves are smaller. The region outside the NS but inside the finite difference grid is filled with a low density atmosphere with  $\rho = 10^{-13} M_{\odot}^{-2}$ . The motion of the NSs is monitored by computing the centroids of the NS mass distributions

$$X_{\text{CM}}^i = \int x^i u^0 \rho_0 \sqrt{-g^{(4)}} d^3x \quad (2.65)$$

for each of the grid patches containing a NS.

The grids are rotated and their separation rescaled to keep the centers of the NS at constant grid-coordinates Scheel et al. (2006); Hemberger et al. (2013); Scheel et al. (2015). As the physical separation between the stars decreases, the rescaling of grid-coordinates therefore causes the size of the stars to increase in grid-coordinates. In order to avoid the stellar surfaces expanding beyond the geometric size of the finite difference grid, we monitor the matter flux leaving this grid along the x, y, and z-direction. If the

---

<sup>2</sup>For aligned-spin configurations **S-.05z** and **S.4z**, we take advantage of, and enforce, z-symmetry, which halves the number of grid-points along the z-axis.

matter flux is too large along a certain axis, we expand the grid in that direction. This procedure allows us to dynamically choose the optimal grid-size that limits matter loss to a small, user-specified level. When changing the size of the hydro grid, the number of grid-points is kept constant, so this process changes the effective resolution during the evolution.

The Einstein field equations are solved on a spectral grid using basis-functions appropriate for the shape of each subdomain. For rectangular blocks, Chebyshev polynomials are used along each axis; for a spherical shell (i.e. where the center is excised), spherical harmonics in angles, and Chebyshev polynomial in radius are employed; and for an open cylinder (i.e. with the region near the axis excised), Chebyshev polynomials and a Fourier series. For full spheres and filled cylinders, multi-dimensional basis-functions respecting the continuity conditions at the origin/axis are employed Matsushima & Marcus (????); Verkley (1997). For more details see Muhlberger et al. (2014).

More specifically, our spectral grid, the central region of each star is covered by a filled sphere located at the center of the star. These have spherical harmonic modes up to  $L = 12 + 2k$ . The radial basis-functions are one-sided Jacobi polynomials with  $7 + k$  collocation points. The filled spheres are surrounded by eight other spherical shells with the same radial and angular resolutions. At the start of the evolution, the stellar surface is generally located inside the third shell. The far field region is covered by 20 spherical shells starting at 1.5 times the initial binary separation and going out to 40 times that separation. These shells have angular resolution  $L = 9 + 2k$  and radial resolution  $6 + k$ . The region between the innermost shell and the stars is covered by a set of cylindrical shells and filled cylinders.

We use a generalized harmonic evolution system Pretorius (2006; 2005); Lindblom et al. (2006) with coordinates  $x^\mu$  such that they satisfy a wave equation

$$\nabla^\nu \nabla_\nu x^\mu = H^\mu, \quad (2.66)$$

for some freely-specifiable source function  $H^\mu$ . The initial source function  $H^\mu_{\text{initial}}$  is

determined by the initial data, assuming that the time derivatives of the lapse and shift functions initially vanish in the corotating frame. We then transition to a pure harmonic gauge,  $H^\mu = 0$  by using a transition function, i.e.

$$H^\mu = e^{-(t/\tau)^4} H_{\text{initial}}^\mu. \quad (2.67)$$

The timescale  $\tau$  is determined by  $\tau = 2\sqrt{d^3/(2M_\star)}$ . This is slow enough to avoid numerical gauge artifacts in the simulations.

### 2.5.2 Eccentricity Removal

Gravitational wave emission reduces orbital eccentricity rapidly during a GW-driven inspiral Peters & Mathews (1963); Peters (1964). Therefore inspiraling binary neutron stars are expected to have essentially vanishing orbital eccentricity in their late inspiral, unless they recently underwent dynamical interactions. Our goal is to model non-eccentric inspirals. In this subsection we demonstrate that we can indeed control and reduce orbital eccentricity, using the techniques developed for BH-BH binaries Pfeiffer et al. (2007); Boyle et al. (2007); Buonanno et al. (2011) and also applied to BH-NS binaries Foucart et al. (2008).

For fixed binary parameters (masses, spins), and fixed initial separation  $D_0$ , the initial orbit of the binary is determined by two remaining parameters: The initial orbital frequency  $\Omega_0$ , and the initial radial velocity, which we describe through an expansion parameter  $\dot{a}_0 = \dot{r}/r$ . These two parameters will encode orbital eccentricity and phase of periastron, and our goal is to determine these parameters to reduce orbital eccentricity. We accomplish this using an iterative procedure first introduced for binary black holes Boyle et al. (2007); Buonanno et al. (2011). An initial data set is evolved for a few orbits, the resulting orbital dynamics are analyzed, and then the initial data parameters  $\Omega_0$  and  $\dot{a}_0$  are adjusted.

For binary neutron stars, we initialize the first iteration of eccentricity removal, with  $\dot{a}_0 = 0$  and use  $\Omega_0$  determined from irrotational BNS initial data, based on the equilibrium

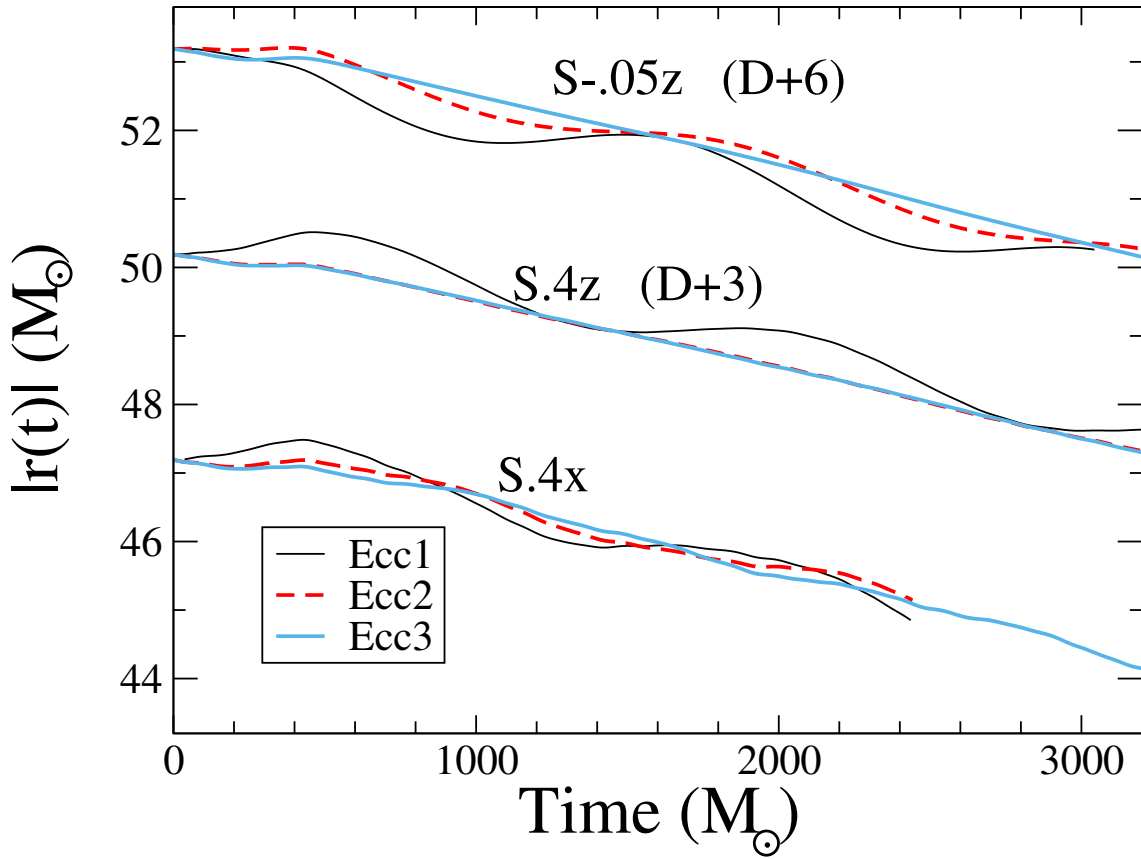


Figure 2.10: The binary separation as a function of time. Shown are three eccentricity removal iterations (Ecc1,Ecc2,Ecc3) for each of the three configurations studied. The data for S-.05z and S.4z is offset vertically by 6 and 3, respectively, for clarity of plotting.

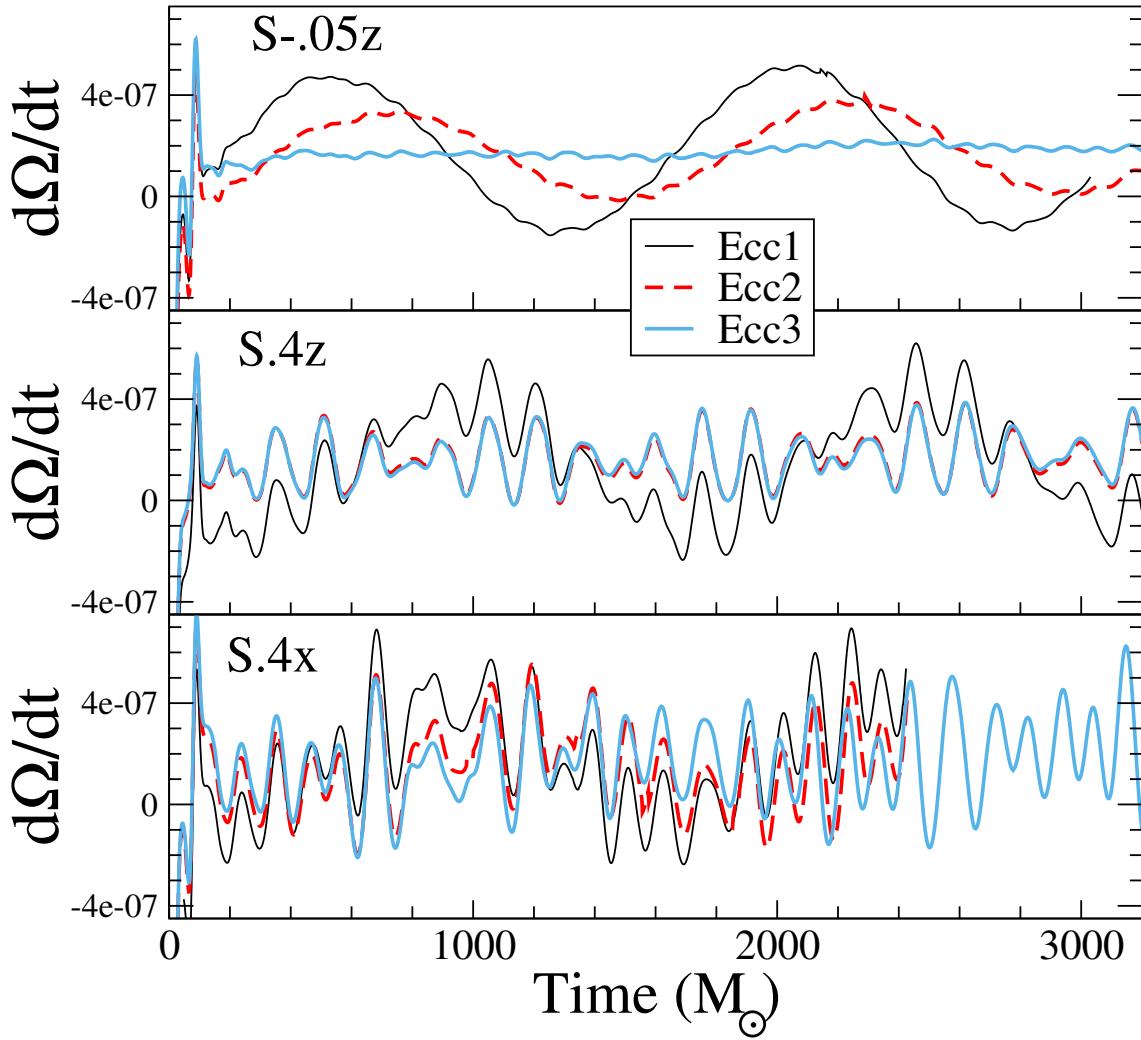


Figure 2.11: The derivative of the binary orbital frequency as a function of time for different levels of eccentricity reduction for our three runs of interest. Note that  $d\Omega/dt$  has units of  $M_{\odot}^{-2}$ .

Name	$\Omega \times 10^3$	$\dot{a}_0 \times 10^5$	$e$
S.4z - Ecc1	5.10538	0	0.006
S.4z - Ecc2	5.09591	-1.60	$\lesssim 0.001$
S.4z - Ecc3	5.09594	-1.75	$\lesssim 0.001$
S-.05z - Ecc1	5.10538	0	0.008
S-.05z - Ecc2	5.11561	0	0.004
S-.05z - Ecc3	5.11769	-1.71	0.0006
S.4x - Ecc1	5.10538	0	0.007
S.4x - Ecc2	5.10429	-2.27	0.004
S.4x - Ecc3	5.10064	-2.36	$\lesssim 0.002$

Table 2.3: Eccentricity removal for the three main runs discussed in this paper. Only initial orbital frequency  $\Omega_0$  and initial radial expansion factor  $\dot{a}_0$  are changed between different EccN iterations. Recall that these quantities have units of  $M_\odot^{-1}$ .

condition in Eq. 2.38. Evolutions with these choices are labeled with the suffix “Ecc1”, and show noticable variations in the separation between the two NS, cf. the solid black lines in Fig. 2.10.

We compute the trajectories of the centers of mass of each star, as determined by Eq. 2.65,  $\vec{c}_1(t)$  and  $\vec{c}_2(t)$ , and using the relative separation  $\vec{r} = \vec{c}_2(t) - \vec{c}_1(t)$ , compute the orbital frequency

$$\Omega(t) = \frac{|\vec{r}(t) \times \dot{\vec{r}}(t)|}{r(t)^2}, \quad (2.68)$$

where an over-dot indicates a numerical time-derivative. Finally, we compute  $\dot{\Omega}(t)$  and fit it to a function of the form

$$\begin{aligned} \dot{\Omega}(t) = & A_1(t_c - t)^{-11/8} + A_2(t_c - t)^{-13/8} \\ & + B_0 \cos(B_1 t + B_2 t^2 + B_3). \end{aligned} \quad (2.69)$$

The power law parts of this fit represent the orbital decay due to the emission of gravita-

tional waves, while the oscillatory part represents the eccentric part of the orbit. We then update  $\Omega_0$  and  $\dot{a}_0$  with the formulae (see Buonanno et al. (2011) for a detailed overview)

$$\Omega_0 \leftarrow \Omega_0 - \frac{B_0 B_1}{4\Omega_0^2} \sin B_3, \quad (2.70)$$

$$\dot{a}_0 \leftarrow \dot{a}_0 + \frac{B_0}{2\Omega_0} \cos B_3. \quad (2.71)$$

We repeat this procedure twice, resulting in simulations with suffix Ecc2 and Ecc3. Table 2.3 summarizes the orbital parameters for the individual simulations, and Figs. 2.10 and 2.11 illustrate the efficacy of the procedure through plots of separation and time-derivative of orbital frequency. The eccentricity is successfully reduced from  $e \sim 1\%$  to  $\sim 0.1\%$ . After two eccentricity reduction iterations, variations in  $\dot{\Omega}(t)$  are so small that they are no longer discernible from higher-frequency oscillations in  $\dot{\Omega}(t)$ , cf. Fig. 2.11.

The high frequency oscillations in  $\dot{\Omega}(t)$  are caused by the quasi-normal ringing of the neutron stars, as discussed in detail below in Sec. 2.5.5. Here, we only note that these oscillations are convergently resolved, cf. Fig. 2.12, and are therefore a genuine feature of our initial data. Figure 2.12 also confirms that the lowest resolution ( $k = 0$ ) gives adequate resolution for eccentricity removal.

The eccentricity removal algorithm attempts to isolate variations on the orbital time-scale as the signature of eccentricity. For S.4z - Ecc2, it reports  $e = 0.0005$  and for S.4z - Ecc3,  $e = 0.0002$ . However, given the large amplitude of the QN mode ringing, we consider these estimates unreliable, and therefore quote an upper bound of 0.001 in Table 2.3. Similarly, for S.4x - Ecc3, the fitting reports  $e = 0.001$ , and we quote a conservative upper bound of 0.002.

### 2.5.3 Aligned spin BNS evolutions: NS Spin

In this section, we will discuss the measurement of spins during our evolutions for the non-precessing cases, S.4z and S-.05z. Aligned spin binaries do not precess. Combined with the low viscosity we expect the NS spins to stay approximately constant during the

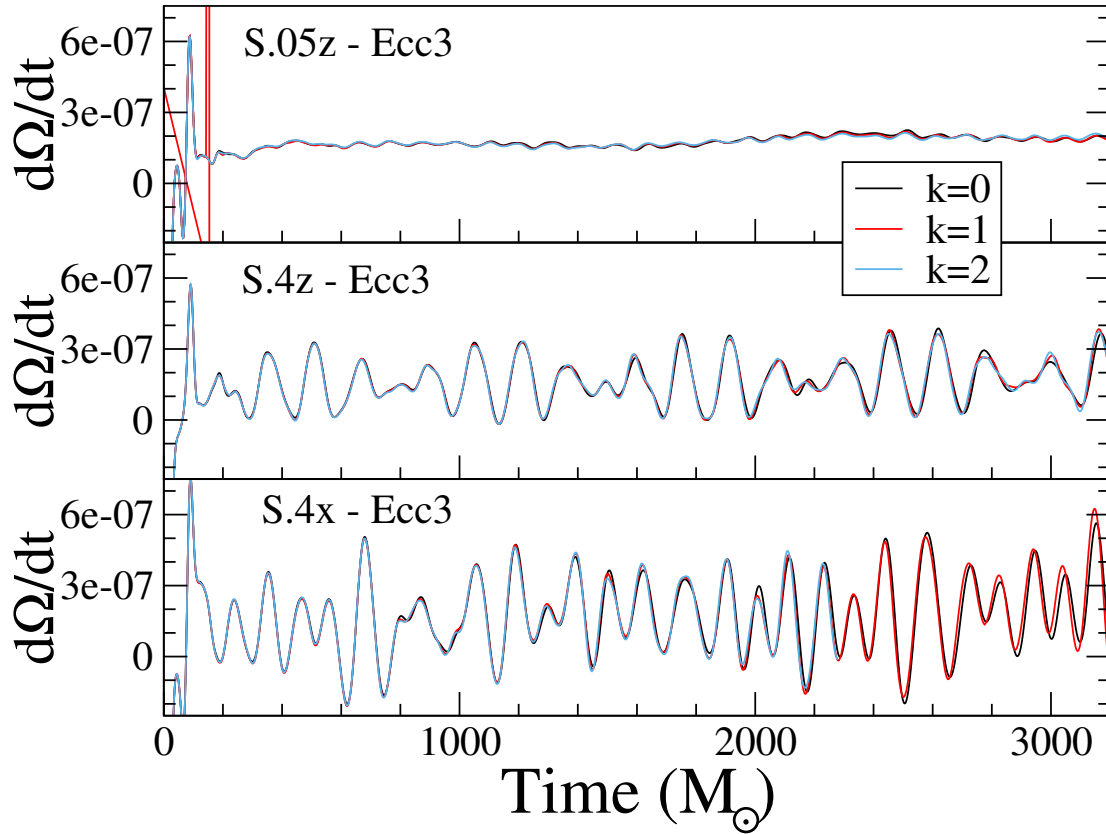


Figure 2.12: Convergence of  $\dot{\Omega}(t)$ . Shown are  $\dot{\Omega}(t)$  at three different numerical resolutions ( $k = 0, 1, 2$ ) for the final, lowest-eccentricity initial data. The oscillations in  $\dot{\Omega}(t)$  are evidently not caused by numerical truncation error. Note that  $\dot{\Omega}$  has units of  $M_\odot^{-2}$ .



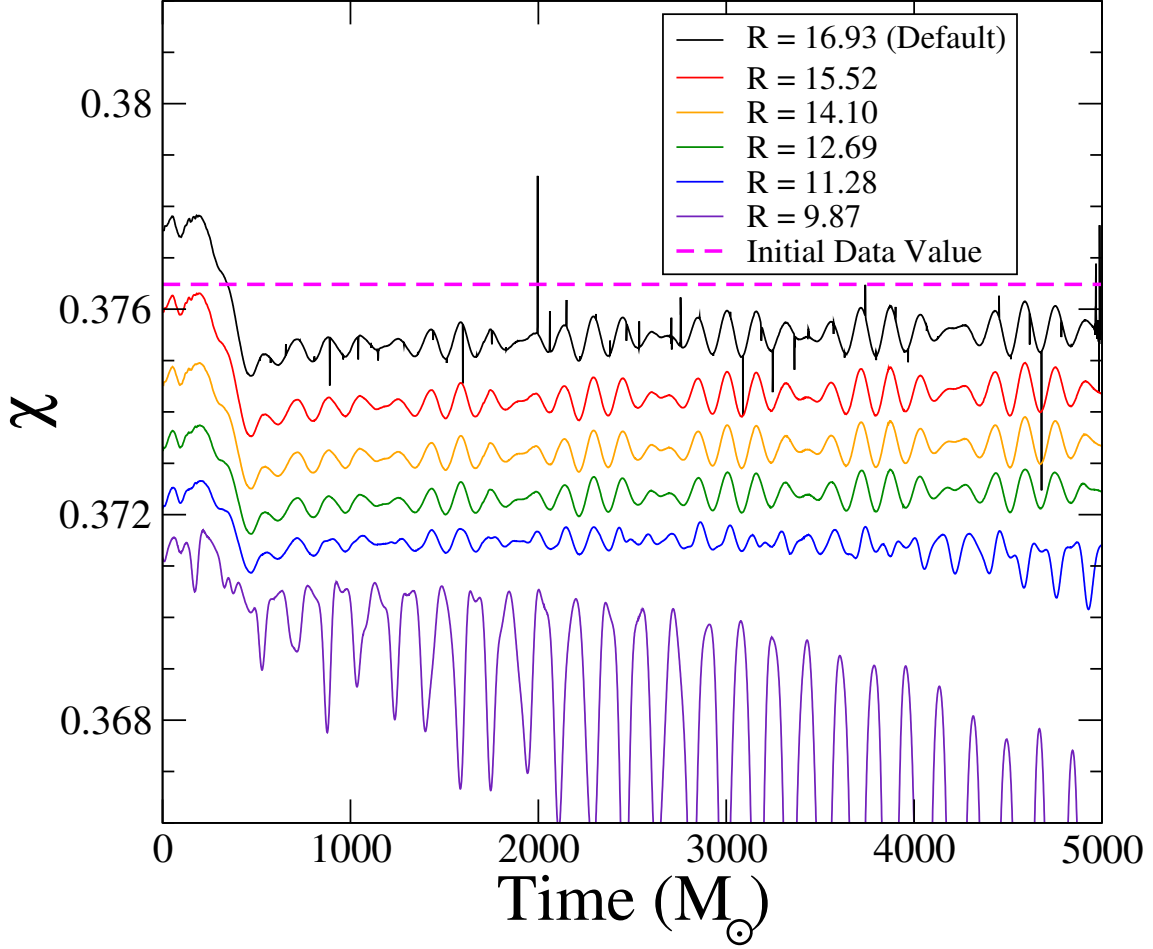


Figure 2.13: The spin measured on multiple coordinate spheres for the **S.4z** run.

evolutions. These systems therefore serve as a test on our spin diagnostics during the evolutions. In this section, and through the rest of this paper, we always use the final eccentricity reduction, “Ecc3”. For brevity, we will omit the suffix “-Ecc3”, and refer to the runs simply as **S-.05z**, etc.

We do not track the surface of the star during the evolution. Instead we simply evaluate the quasi-local spin of the stars on coordinate spheres in the frame comoving with the binary. We must therefore verify that the spin measured is largely independent of the radius of the sphere, and that it is maintained during the evolutions at the value consistent with that in the initial data. Figure 2.9 established that coordinate spheres can be used to extract the quasi-local spin in the initial data. Figure 2.13 shows the

results for the high-spin simulation **S.4x** during the inspiral.

For coordinate spheres with radii  $R = 11.28M_\odot$  to  $R = 16.93M_\odot$  in grid coordinates, the spins remain roughly constant in time. The different extraction spheres yield spins that agree to about 1%, with a consistent trend that larger extraction spheres result in slightly larger spins (as already observed in the initial data). The horizontal dashed line in Fig. 2.13 indicates the spin measured on the stellar surface (i.e. not on a coordinate sphere) in the initial data. We thus find very good agreement between all spin measurements, and conclude that the quasi-local spin is reliable to about 1%.

The extraction sphere  $R = 9.87M_\odot$  in Fig. 2.13 intersects the outer layers of the neutron star. Because the quasi-local spin captures only the angular momentum within the extraction sphere, the value measured on  $R = 9.87M_\odot$  falls as our comoving grid-coordinates cause this coordinate sphere to slowly move deeper into the interior of the star. This behavior, again, is consistent with Fig. 2.9.

These tests of using multiple coordinate spheres were only run for about half of the inspiral – enough to establish that the method is robust. Subsequently, we report spins measured on the largest coordinate sphere,  $R = 16.93M_\odot$ .

The full behavior of the spin during the inspiral is shown in figure 2.14 for both the **S.4z** and **S-.05z** runs. Comparing the spin at different resolutions, we note that the data for  $k = 1$  and  $k = 2$  are much closer to each other than compared to  $k = 0$ , indicating numerical convergence. We note that the impact of numerical resolution (as shown in Fig. 2.14) is small compared to the uncertainty inherent from the choice of extraction sphere, cf. Fig. 2.13. We also note that for the first  $10000M_\odot$  of the run, the measured spin behaves as a constant, as expected, albeit with some small oscillations. However, afterward, we notice the absolute value of the spin starts to decrease in both cases. Finally, we note that in both cases, the spin measured in the initial data on the stellar surface is within  $\Delta\chi = 0.008$  of the spin measured during the evolution.

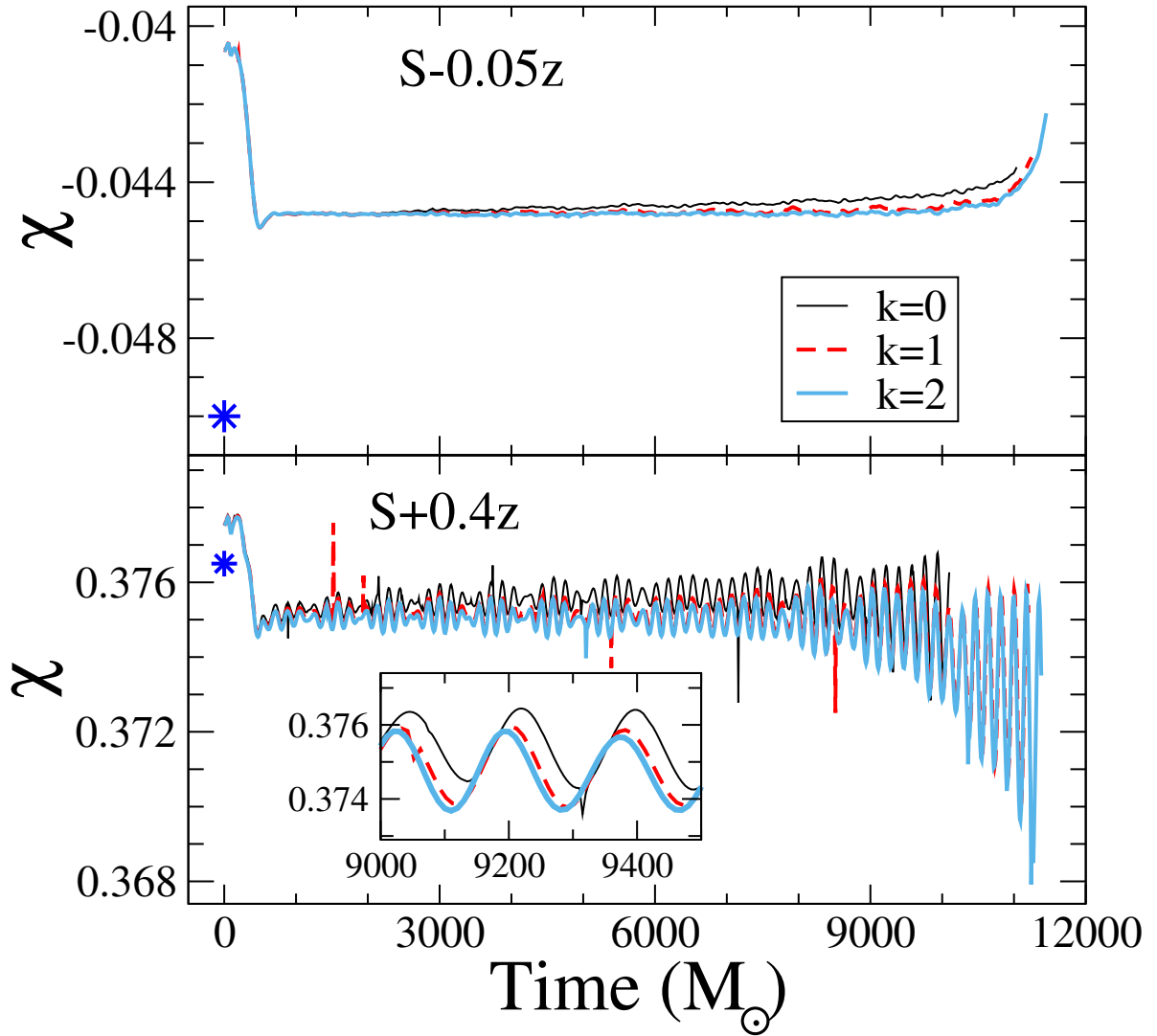


Figure 2.14: Neutron star spin during the two aligned-spin evolutions. Shown are three different numerical resolutions,  $k = 0$  (lowest),  $k = 1$ , and  $k = 2$  (highest). The asterisk indicates the spin measured on the stellar surface in the initial data.

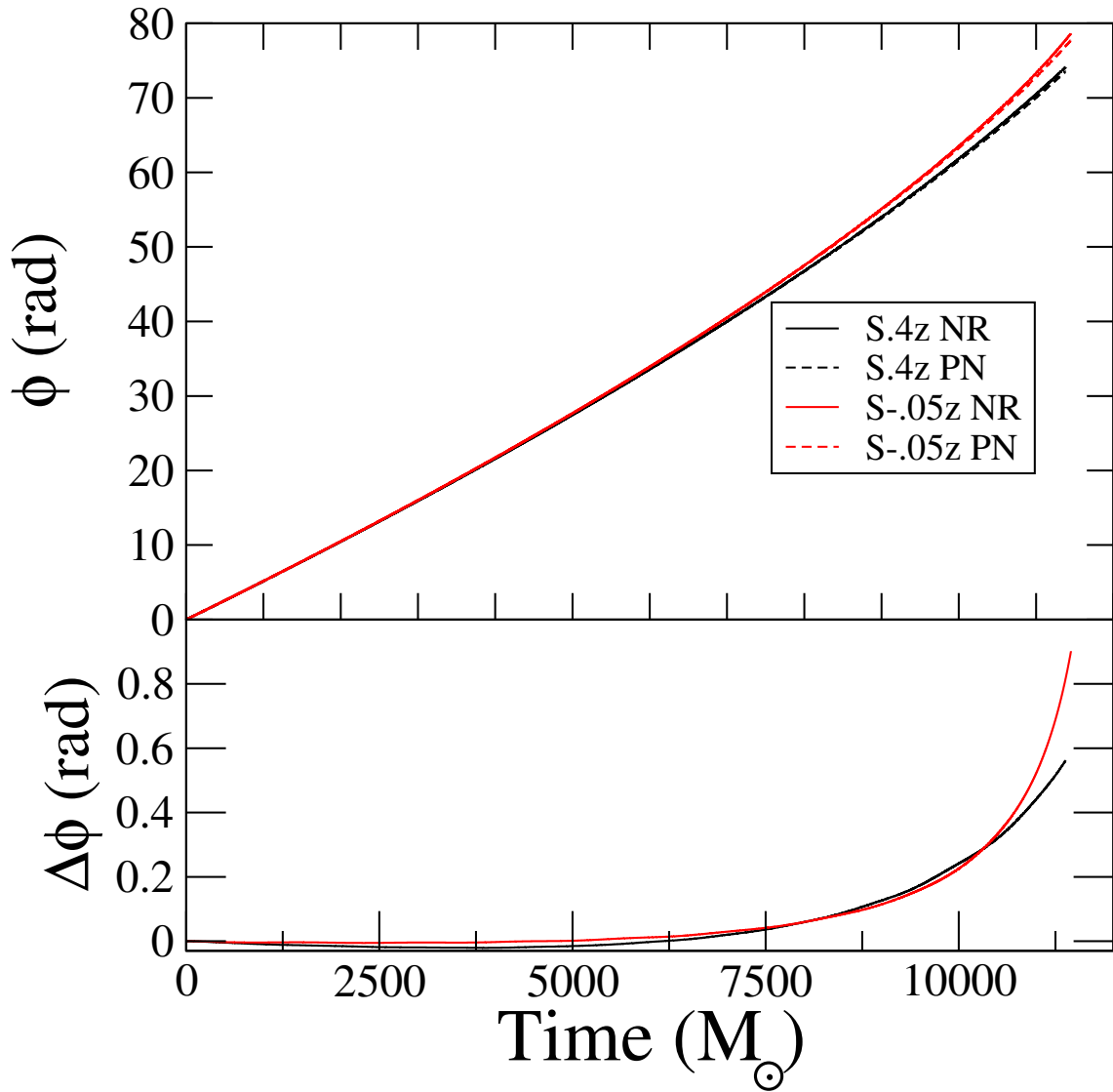


Figure 2.15: Accumulated orbital phase as a function of time for our anti-aligned, S-.05z, and aligned, S.4z, runs. The dashed lines are Taylor T4 PN simulations. The PN simulations were matched to NR in the intervals [1109,3956] and [2090,4904] respectively. Qualitatively, there is excellent agreement with the numerical data. The lower panel shows the difference  $\Delta\phi(t) = \phi_{\text{NR}}(t) - \phi_{\text{PN}}(t)$ .

Finally, we compute the orbital phase

$$\phi(t) = \int_0^t \Omega(t') dt', \quad (2.72)$$

where the orbital frequency  $\Omega(t)$  is given by Eq. (2.68). The result is plotted in Fig. 2.15, along with the

Post-Newtonian prediction for the same binary parameters (spins, masses and initial orbital frequencies). We use the Taylor T4 model (see e.g., Boyle et al. (2007)) at 3.5PN order expansion, with no tidal terms added, using the matching techniques described in Ossokine et al. (2015). We find excellent qualitative agreement in both cases, thereby giving additional evidence that our numerical simulations are working as expected. We do find large late time growth in the phase difference, however this is expected because we do not model tidal effects, which become increasingly important at late times, in our Post-Newtonian equations.

Figure 2.16 shows the gravitational waveforms for our two non-precessing simulations. We extract the waves on a sphere of radius  $R = 627M_\odot$ .

### 2.5.4 Precession

We now turn to the precessing simulation, S.4x. Figure 2.17 shows the components of the spin-vector  $\vec{\chi}$  of one of the neutron stars, as a function of time. The quasi-local spin diagnostic returns a spin with nearly constant magnitude, varying only by  $\pm 0.002$  around its average value 0.370. The spin components clearly precess, with the dominant motion in the xy-plane (the initial orbital plane), with the simulation completing about 2/3 of a precession cycle. A z-component of the NS spin also appears, indicating precession of the neutron star spin out of the initial orbital plane.

Fig. 2.17 shows a comparison of spin precession between numerical relativity and Post-Newtonian theory. We perform this comparison using the matching technique in Ossokine et al. (2015). This gives very good agreement between PN (dotted) and NR

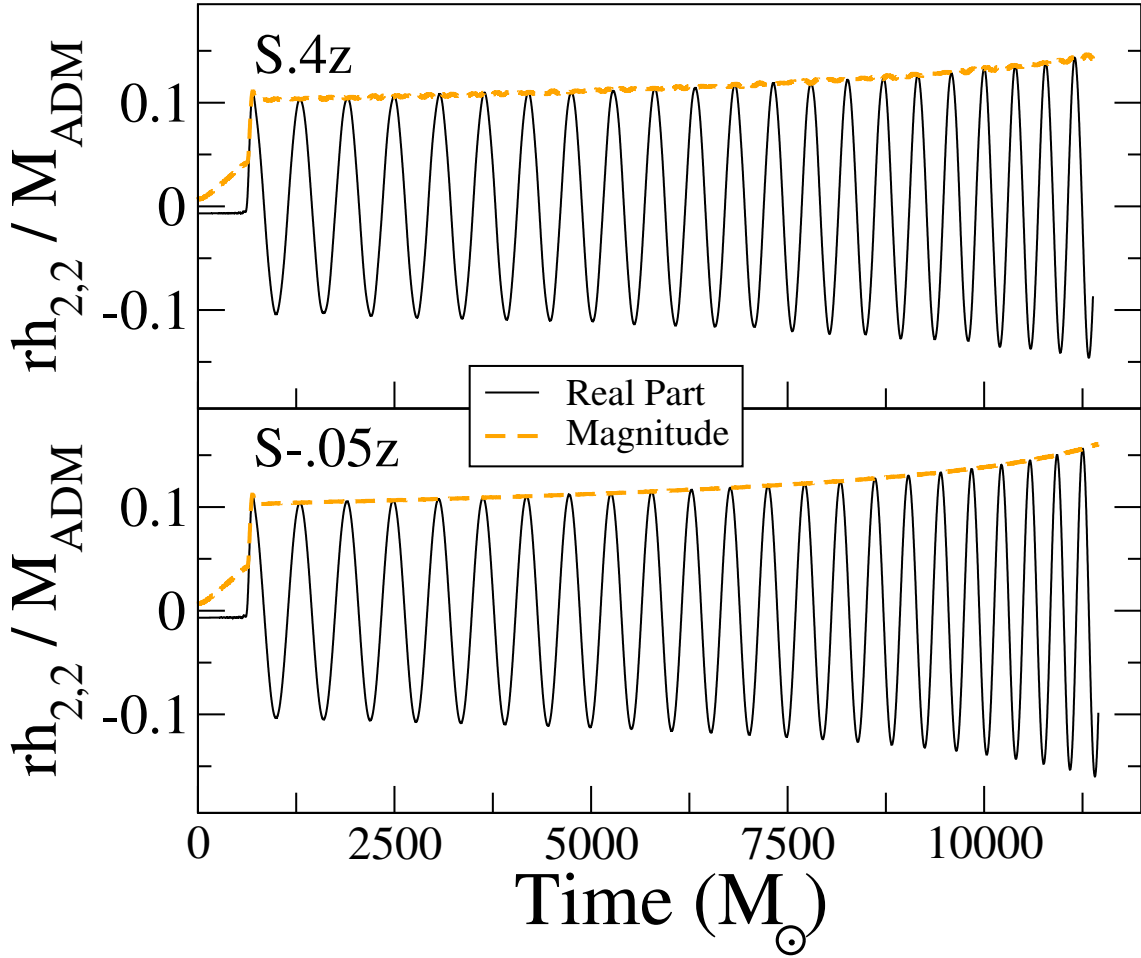


Figure 2.16: The gravitational waveforms for our anti-aligned, S-.05z, and aligned, S.4z runs. The black curve represents the real part of the waveform,  $\Re(h_{2,2})$  while the orange curve represents the magnitude of the waveform.

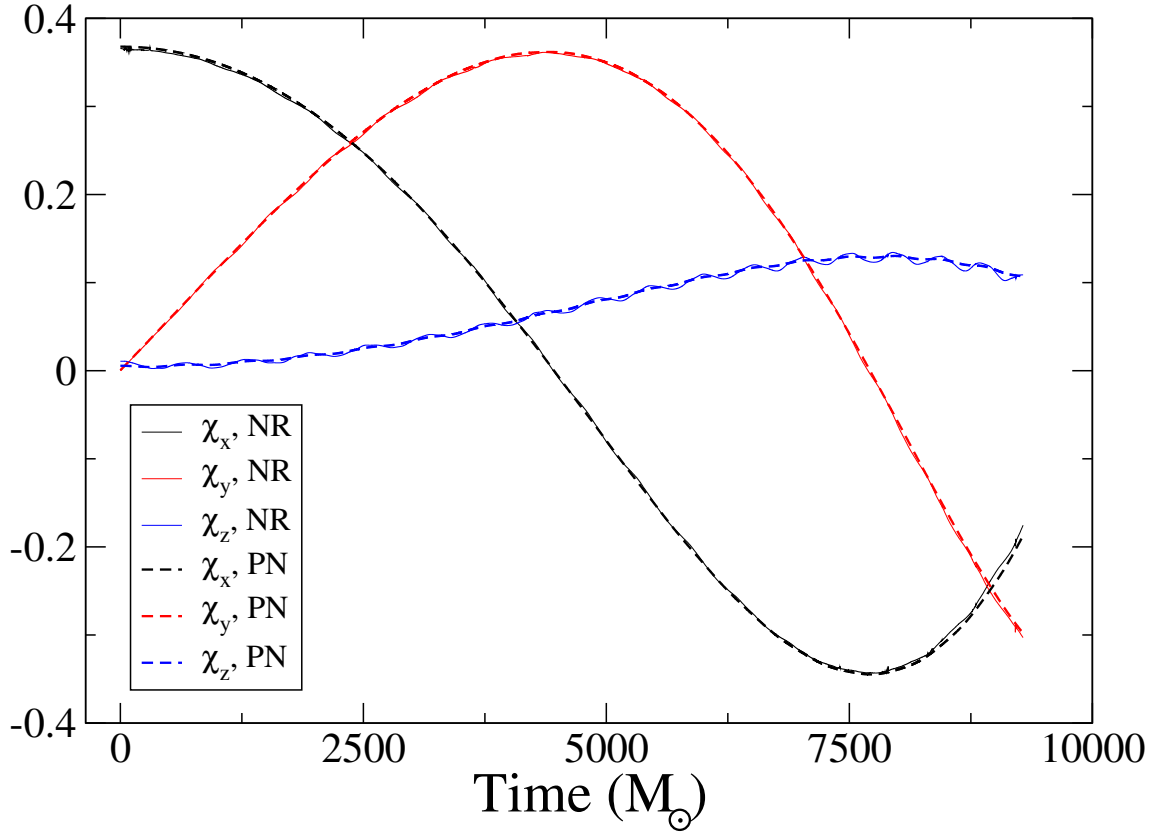


Figure 2.17: Spin-components of one of the neutron stars during the precessing simulation (thick, solid lines). The dotted and dashed lines represent the unmatched and matched PN results respectively. The agreement between PN and NR is good for both PN simulations. The orbital frequency was evolved using the Taylor T4 approximant. The matching was done in the interval  $[1892, 4575]$ .

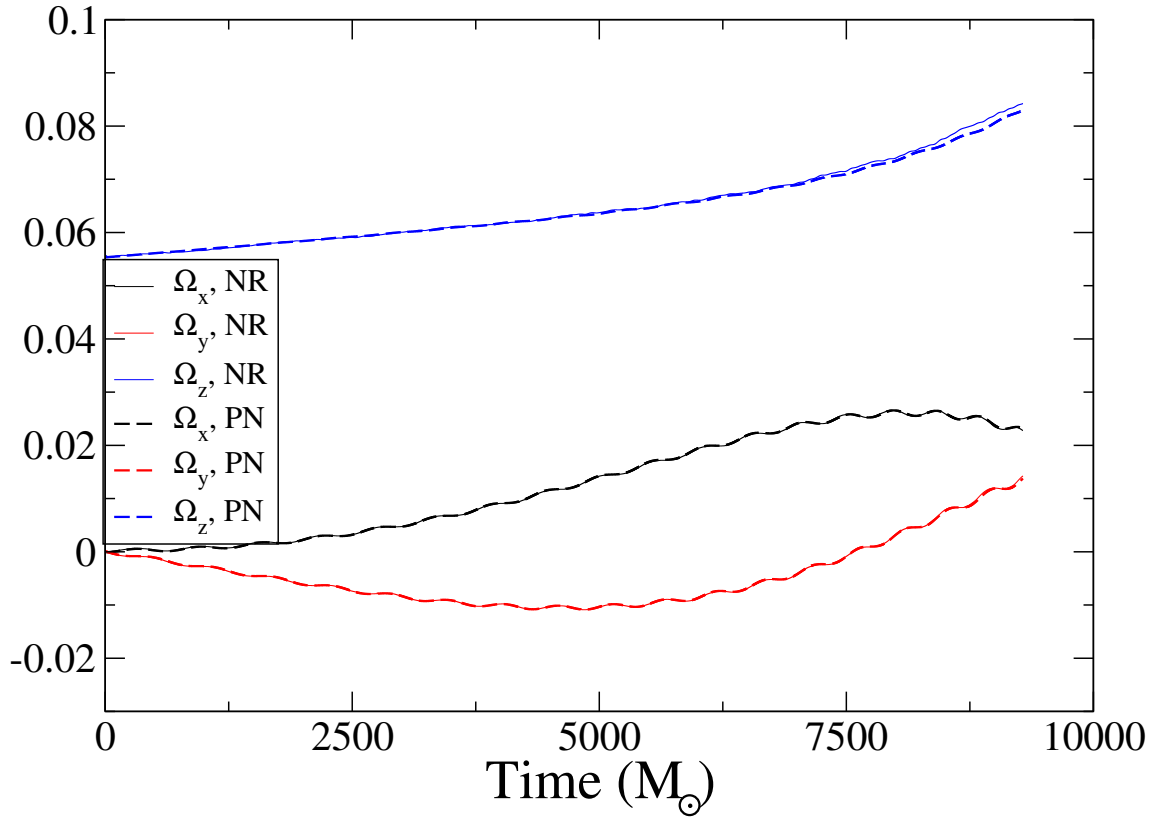


Figure 2.18: Components of the orbital frequency vector  $\vec{\Omega}$ . Thick solid lines represent the precessing BNS simulation and thin dashed lines represent the matched post-Newtonian simulations. The inclination reaches  $\delta = 0.34\text{rad}$  at  $t = 7600M_\odot$ .



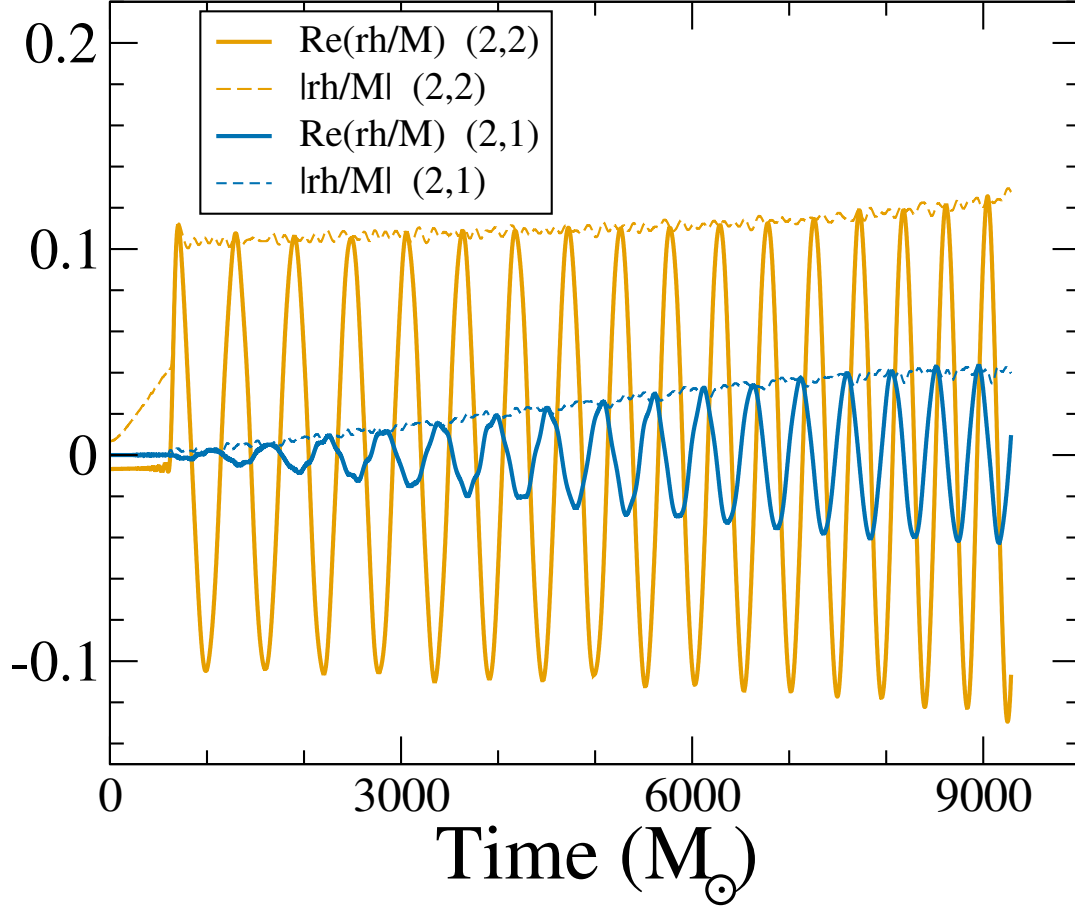


Figure 2.19: Gravitational waveforms of our precessing run. Shown are the  $(l, m) = (2, 2)$  and  $(2, 1)$  modes, as extracted in a spherical harmonic decomposition aligned with the  $z$ -axis. The emergence of the  $(2, 1)$  mode indicates precession of the orbital plane away from the  $xy$ -plane.

(solid) as shown by Fig. 2.17. The NS spins indeed precess as expected, thus confirming both the quality of quasi-local spin measures, as well as the performance of the PN equations. Note that  $z$ -component of the spin in the NR data undergoes oscillations that are unmodelled by PN. These occur on a timescale of half the orbital timescale. Similar effects were found in Ossokine et al. (2015). The origin of these oscillations remains unclear. The precession of the orbital angular frequency is shown in Fig. 2.18. We find substantial precession away from the initial direction of the orbital frequency  $\vec{\Omega}_0 \propto \hat{z}$ , with the angle  $\delta$  between  $\vec{\Omega}(t)$  and the  $z$ -axis reaching  $20^\circ$ . Once again, the PN equations reproduce the precession features successfully.

Finally, Fig. 2.19 shows the (2,2) and the (2,1) spherical harmonic modes of the gravitational wave-strain extracted at an extraction surface of radius  $R = 647M_\odot$ . The (1,m)=(2,1) mode would be identically zero for an equal-mass aligned spin binary with orbital frequency parallel to the z-axis, so the emergence of this mode once again indicates precession in this binary.

### 2.5.5 Stellar Oscillations

The rotating neutron stars constructed here show oscillations in the central density, as plotted in Fig. 2.20. In the low spin run, the density oscillations have a peak-to-peak amplitude of about 0.6%, whereas in the high-spin runs (S.4z and S.4x), the density oscillations reach a peak-to-peak amplitude of 20%. The two high-spin simulations show oscillations of nearly the same amplitude and frequency, therefore oscillating nearly in phase throughout the entire inspiral. The oscillation-period is about  $177M_\odot \sim 0.87\text{ms}$ , i.e. giving a frequency of 1.15kHz. It remains constant throughout the inspiral. The low-spin run S-0.5z exhibits a slightly smaller oscillation period of about  $P \approx 170M_\odot \approx 0.84\text{ms}$ , i.e. a frequency of  $\approx 1.19\text{kHz}$ .

To investigate the spectrum of the density oscillations, we perform a Fourier-transform on  $\rho(t)$ . The result is shown in Fig. 2.21. The Fourier-transform confirms the dominant frequencies just stated, and reveals several more frequency components ranging up to 4kHz. The high spin evolutions S.4z and S.4x exhibit identical frequencies for all five discernible peaks. In contrast, the low-spin evolution S-.05z shows different frequencies.

We interpret these features as a collection of excited quasi-normal modes in each neutron star. The modes are excited because the initial data is not precisely in equilibrium. For the two high-spin cases the neutron stars have similar spin, and therefore the same quasi-normal modes, whereas in the low-spin model, the quasi-normal mode frequencies differ due to the different magnitude of the spin.

To strengthen our interpretation, we consider the series of rotating, relativistic,  $\Gamma = 2$

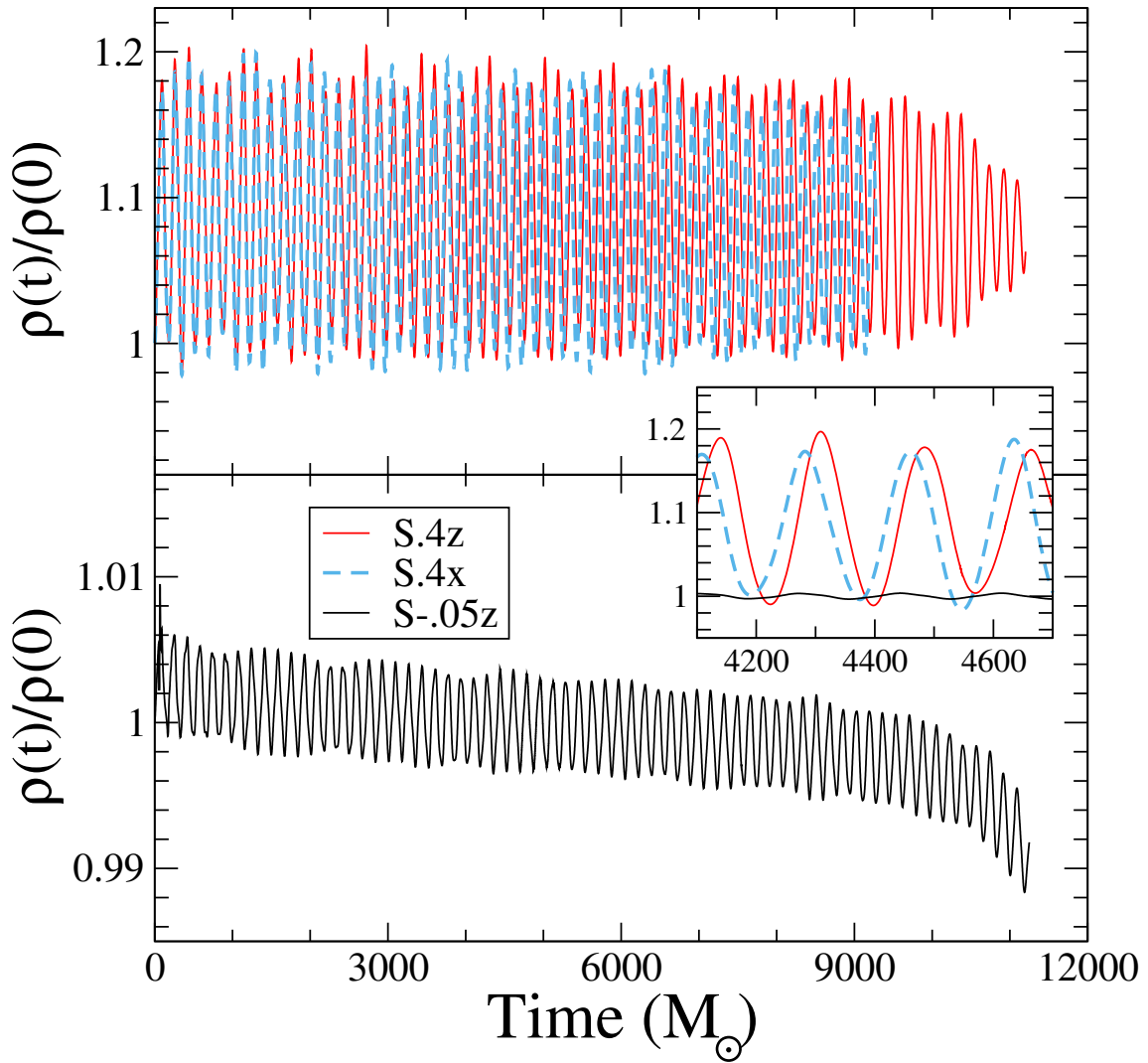


Figure 2.20: The maximum density  $\rho(t)$  in each of our runs, normalized by the initial maximum density  $\rho(0)$ . The inset shows an enlargement of all three runs, illustrating that the oscillations are more pronounced in the high-spin simulations.

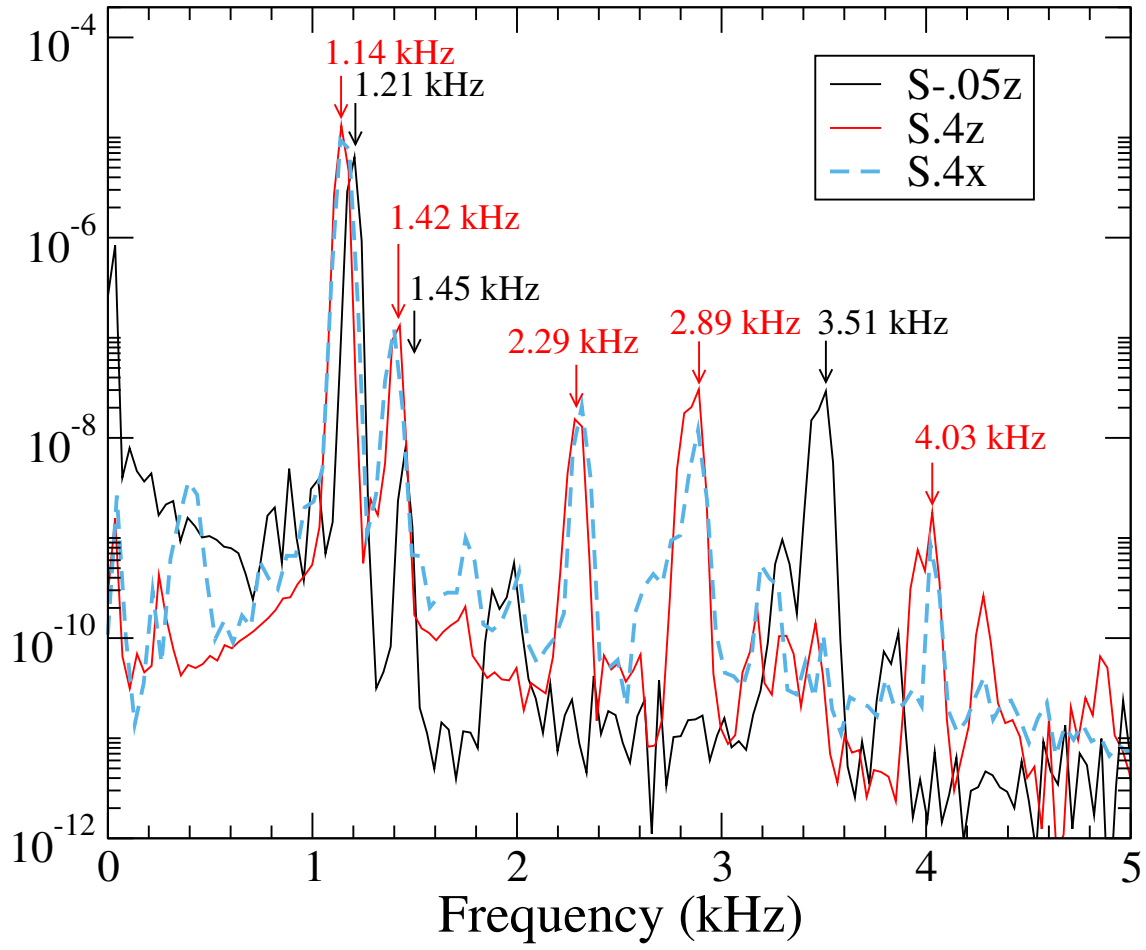


Figure 2.21: The Fourier transforms of the central density in all three of our runs. Labelled are the peak frequencies for the quasi-radial F mode and the  $l = 2, {}^2f$  mode.

polytropes computed by Dimmelmeyer et al Dimmelmeyer et al. (2006).

Ref. Dimmelmeyer et al. (2006)’s model “AU3” has a central density of  $1.074 \times 10^{-3} M_{\odot}^{-2}$  and its rotation is quantified through the ratio of polar to equatorial radius,  $r_p/r_e = 0.780$ . Meanwhile, our high-spin runs have a central density of  $1.02 \times 10^{-3} M_{\odot}^{-2}$  (measured as time-average of the data shown in Fig. 2.20) and from our initial data, we find  $r_p/r_e \sim 0.8$ . Given the similarity in these values, we expect Ref. Dimmelmeyer et al. (2006)’s “AU3” to approximate our high-spin stars **S.4x**, **S.4z**. Ref. Dimmelmeyer et al. (2006) reports a frequency of  $f_F = 1.283\text{kHz}$  for the spherically symmetric ( $\ell = 0$ ) F-mode, and a frequency  $f_{2f} = 1.537\text{kHz}$  for the axisymmetric  $\ell = 2$  mode  ${}^2f$ . These frequencies compare favorably with the two dominant frequencies in Fig. 2.21, 1.14kHz and 1.42kHz.

Presumably, the small differences in these frequencies can be accounted for by the slight differences in stellar mass, radius, and rotation. Moreover, tidal interactions and orbital motion could factor in, as well. In our figure 2.21 we also see several other peaks at higher frequencies, which are reminiscent of the overtones and mode couplings in figure 10 of Dimmelmeyer et al. (2006). If we identify our peak at  $f_{H1} = 4.03\text{kHz}$  with the  $H_1$  mode, then (in analogy to Dimmelmeyer et al. (2006) Fig. 10),  $f_{H1} - f_F = (4.03 - 1.14)\text{kHz} = 2.89\text{kHz}$ , and  $2f_F = 2.28\text{kHz}$ , two frequencies that are indeed present in our simulations. Although we find clear indications of axisymmetric  $\ell = 2$ -modes, we note that their power is smaller by two orders of magnitude, compared to the spherically symmetric, dominant  $F$  mode.

Turning to the low-spin run **S.05z**, we note that if, to first order, these frequencies scale like  $f \sim \sqrt{\rho}$  (on dimensional grounds), then we expect to see  $F = 1.22\text{kHz}$  and  ${}^2f = 1.49\text{kHz}$ . This is very close to what is seen.

The density oscillations discussed in this section are reflected in analogous oscillations in various other diagnostic quantities, for instance, the orbital frequency, Fig. 2.12 and the quasi-local spin as shown in Fig. 2.14. The dominant frequencies 1.14kHz and 1.42kHz can be robustly identified throughout our data analysis. In figure 2.22 we plot the

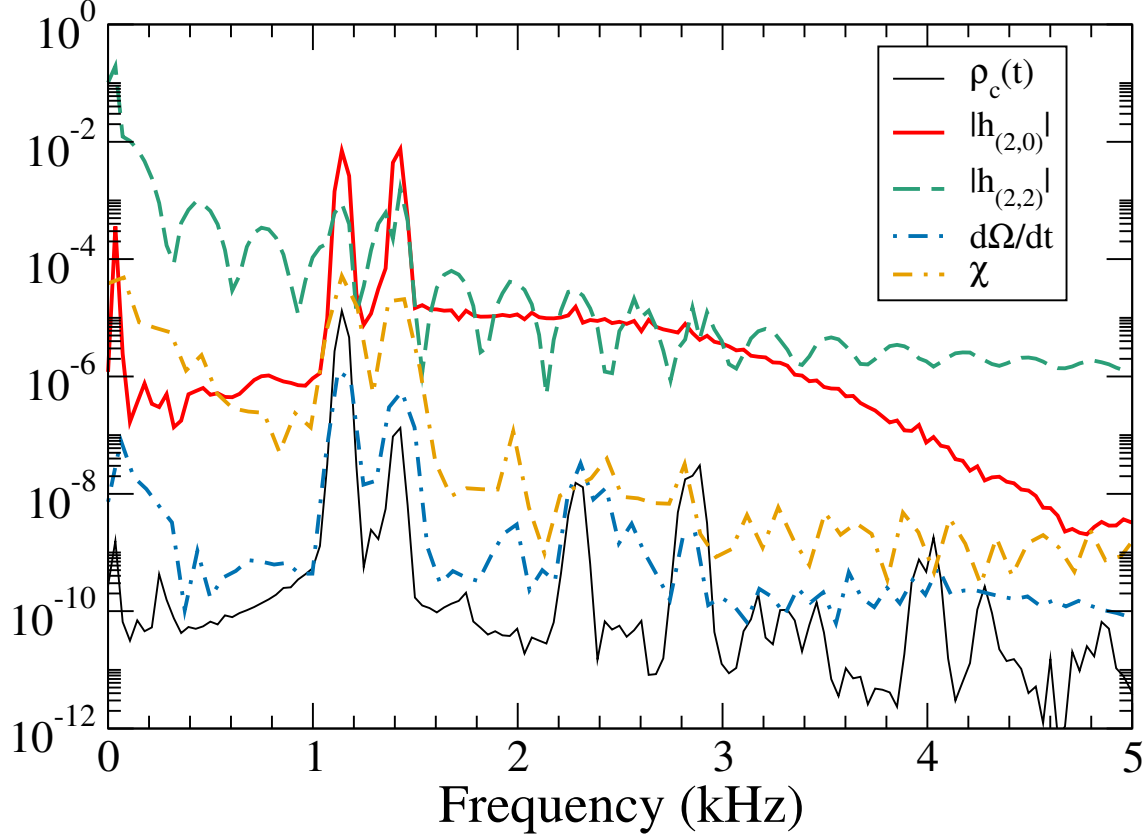


Figure 2.22: Fourier transforms of the central density  $\rho_c(t)$ , two modes of the magnitude of gravitational wave strain ( $|h_{2,2}|$  and  $|h_{2,0}|$ ),  $\dot{\Omega}$  and  $\chi$  for the **S.4z** run. All quantities show excess power at 1.14kHz and 1.4kHz, corresponding to the frequencies of excited neutron star quasi-normal modes.

Fourier transform of the density, the (2,0) and (2,2) gravitational wave strains, the orbital angular velocity time derivative  $d\Omega/dt$  and the measured spin  $\chi$  for the **S.4z** run. All show peaks in power at these two frequencies,  $F \sim 1.14\text{kHz}$  and  ${}^2f \sim 1.4\text{kHz}$ . Gold et. al. Gold et al. (2012), in the simulation of close encounters in eccentric, irrotational, NSNS binaries, **where the modes are physical and much stronger than the quasi-circular case**, find an excited f-mode frequency of 1.586 kHz.

We believe that the stellar modes are excited because the initial data are not in perfect equilibrium. We expect the quasi-equilibrium approximations that enter the initial data formalism to become less valid at higher spins, consistent with our observation that

the high spin models exhibit stronger oscillations. This interpretation is strengthened by additional simulations of neutron stars at larger separation. Increasing the initial separation by a factor 1.5, while keeping the same rotation parameter  $\omega$  as in the S.4z-case, we find quasi-normal oscillations of similar amplitude than in S.4z. If the oscillations were caused by the neglect of tidal deformation, we would expect the amplitude to drop with the 3rd power of separation, inconsistent with our results.

Finally, we point out that the radial rotation profile, cf. Eq. (2.48) influences the amplitude of the induced quasi-normal oscillations. If the initial data is constructed with the rotation profile Eq. (2.49), instead of equation 2.48, then the amplitude of the density oscillations for high spin doubles. This further supports our conjecture that the origin of this mode comes from non-equilibrium initial data.

## 2.6 Discussion

In this paper we implement Tichy’s method Tichy (2012) to construct binary neutron star initial data with arbitrary rotation rates. We demonstrate that our implementation is exponentially convergent, as expected for the employed spectral methods.

We measure the spin of the resulting neutron stars using the quasi-local angular momentum formalism Brown & York (1993); Cook & Whiting (2007); Lovelace et al. (2008); Owen (2007). The resulting angular momentum is found to be nearly independent on the precise choice of extraction sphere, cf. Fig. 2.9, and provides a means to define the quasi-local angular momentum of each neutron star to about 1%, both in the initial data and during the evolution, cf. Fig. 2.13. We are able to construct binary neutron star initial data with dimensionless angular momentum of each star as large as  $\chi = S/M^2 \sim 0.43$ , both for the case of aligned spins, and also for a precessing binary where the initial neutron star spins are tangential to the initial orbital plane.

For irrotational BNS initial data sets, we find a quasi-local angular momentum of  $\chi \sim 2 \times 10^{-4}$ , cf. Fig. 3.8. This spin is small enough that present waveform modeling

studies for BNS (e.g. Bernuzzi et al. (2015); Baiotti et al. (2011); Baiotti et al. (2010)) are not yet limited by residual spin.

When evolving the initial data sets, the dimensionless spin measured in the initial data drops by about 0.004, and then remains constant through the 10 inspiral orbits for which we evolved the neutron star binaries. During these evolutions, we also demonstrated iterative eccentricity removal: By analyzing the orbital frequency  $\Omega(t)$  during the first few orbits, we can correct the initial data parameters  $\Omega_0$  and  $\dot{a}_0$ , and thus decrease the orbital eccentricity from  $e \approx 0.01$  to  $e \lesssim 0.001$ .

For the precessing simulation **S.4x**, we find precession of the neutron star spin directions. The numerically established precession of the spin axes and of the orbital angular momentum agrees well with post-Newtonian predictions.

The rotating neutron stars constructed here exhibit clear signals of exciting quasi-normal modes. We are able to identify multiple modes in the Fourier spectrum of the central density. The amplitude of the excited quasi-normal modes increases steeply with rotation rate of the neutron stars. For **S-.05z** (spin magnitude  $\chi = 0.045$ ) the density oscillations have peak-to-peak amplitude of 0.6%, raising to 20% for the two runs with high spins (**S.4x** and **S.4z**).



# Chapter 3

## Initial Data for Spinning Neutron Stars in Mixed Binaries

### 3.1 Introduction

The spectacular detection of merging binary black holes by Advanced LIGO (Abbott et al. (2016b), Abbott et al. (2016a)) has dawned the beginning of the era of gravitational wave astronomy. Black-hole - neutron star (Bh-Ns) binaries are now the only compact object binary whose existence has not been directly confirmed. They remain, however, an important potential source of gravitational waves for advanced ground-based detectors, with an expected event rate of approximately ten per year (Abadie et al. (2010a)), albeit with a large uncertainty. In addition to gravitational waves, Bh-Ns mergers can be an exciting source of electromagnetic radiation and give further clues to the violent processes that occur during the merger. If a massive disk is left from the merger, it could lead to a short-duration gamma ray burst (SGRB) and material ejected during the merger could radiate a signal such as a "kilonova" (Metzger & Berger (2012)).

Numerical relativity simulations are important to accurately study both the gravitational waves and electromagnetic emission produced in Bh-Ns mergers. The parameter space for Bh-Ns binary simulations is relatively large. The mass ratio,  $q$ , and black hole

spin,  $\vec{\chi}$ , have been of particular interest in numerical simulations. [cites](#) Foucart (2012) gave a semi-analytic description of how this combination (of mass ratio and spin magnitude) can predict when neutron star disruption occurs. The neutron star equation of state is also of great interest, especially in more recent simulations that can incorporate more microphysics. [cites](#) The size of the star is directly linked to when tidal disruption occurs. One aspect that has not been studied, however, is the effect of neutron star spin, as all simulations to date use irrotational neutron stars in their Bh-NS binaries. For Ns-Ns binaries, in contrast, A significant number of studies, however, investigate spinning neutron stars in Ns-Ns binaries (Baumgarte & Shapiro (2009), Tichy (2011), East et al. (2012), Tichy (2012), Bernuzzi et al. (2014), Kastaun et al. (2013), Tsatsin & Maronetti (2013), Dietrich et al. (2015), East et al. (2015), Tsokaros et al. (2015), Tacik et al. (2015)). Since no Bh-NS binaries have been directly observed, the NS spins are, at least observationally, unconstrained. Spinning NS will affect the gravitational waveforms and cause the inspiral to proceed more slowly (for spin-aligned NS). The spin can be important for gravitational wave detection and can cause appreciable mismatch with non-spinning templates, especially at lower Bh-Ns mass ratios (Ajith (2011)). The spin could also affect the time of NS disruption, as the stellar material will be less tightly bound to the stellar surface.

Recently, Tacik et al. (2015) used the `SpEC` code to create and evolve initial data sets of binary neutron star systems with arbitrary spins. In this chapter, we extend this code to create initial data for Bh-Ns systems where the neutron star spin is arbitrary. The structure of this chapter is as follows: In section 3.2, we review standard numerical relativity initial data formalism, as well as the formalism developed in Tichy (2011) to create binaries with spinning NS, and discuss how this is extended to Bh-NS systems. In section 3.3 we discuss the numerical methods used by our initial data solver. In section 4.6, we create a number of initial data sets to demonstrate the robustness of our solvers. We extend the results of Foucart et al. (2013) to incorporate different neutron

star spins, and we also create a variety of initial data sets with various values of neutron star spin, black hole spin, and mass ratio, to demonstrate robustness across the Bh-Ns parameter space. We demonstrate initial data convergence and investigate properties of the solution. Finally, we conclude the chapter in section 3.5.

## 3.2 Initial Data Formalism

Consider shortening this section and instead reference previous sections. In this section we will discuss the formalism used to solve the Einstein field equations and create quasi-equilibrium initial data for BH-NS binaries with spinning neutron stars. We begin with the  $3 + 1$  decomposition of the space-time metric tensor,

$$g_{\mu\nu}dx^\mu dx^\nu = -\alpha^2 dt^2 + \gamma_{ij} (dx^i + \beta^i dt) (dx^j + \beta^j dt), \quad (3.1)$$

where  $\alpha$  is the lapse function,  $\beta^i$  is the shift vector, and  $\gamma_{ij}$  is the induced metric on a spatial hypersurface  $\Sigma(t)$ . The normal vector  $n^\mu$  to  $\Sigma(t)$  is related to the coordinate time  $t$  by

$$t^\mu = \alpha n^\mu + \beta^\mu. \quad (3.2)$$

The extrinsic curvature of  $\Sigma(t)$  is given by

$$K_{\mu\nu} = -\frac{1}{2}\mathcal{L}_n \gamma_{\mu\nu}, \quad (3.3)$$

where  $\gamma_{\mu\nu} = g_{\mu\nu} + n_\mu n_\nu$ . and  $\mathcal{L}_n$  is the Lie derivative in the direction of the  $n^\mu$ . We restrict our attention to the spatial part of the extrinsic curvature,  $K^{ij}$ , since  $n_\mu K^{\mu\nu} = 0$  by construction. It is convenient to decompose it into its trace and trace-free parts,

$$K^{ij} = A^{ij} + \frac{1}{3}K\gamma^{ij}. \quad (3.4)$$

The matter in the system is modelled with the stress-energy tensor of a perfect fluid

$$T_{\mu\nu} = (\rho + P) u_\mu u_\nu + P g_{\mu\nu}, \quad (3.5)$$

where  $\rho$  is the fluid's energy density,  $P$  is its pressure, and  $u^\mu$  is its four-velocity. It is further useful to define the projections of the matter quantities,

$$E = T^{\mu\nu} n_\mu n_\nu, \quad (3.6)$$

$$S = \gamma^{ij} \gamma_{i\mu} \gamma_{j\nu} T^{\mu\nu}, \quad (3.7)$$

$$J^i = -\gamma_\mu^i T^{\mu\nu} n_\nu. \quad (3.8)$$

The spatial metric is decomposed with the conformal transformation

$$\gamma_{ij} = \Psi^4 \tilde{\gamma}_{ij}, \quad (3.9)$$

where  $\Psi$  is called the conformal factor, and  $\tilde{\gamma}_{ij}$  is the conformal metric. The other quantities in the initial value problem use the following conformal transformations:

$$E = \Psi^{-6} \tilde{E}, \quad (3.10)$$

$$S = \Psi^{-6} \tilde{S}, \quad (3.11)$$

$$J^i = \Psi^{-6} \tilde{J}^i, \quad (3.12)$$

$$A^{ij} = \Psi^{-10} \tilde{A}^{ij}, \quad (3.13)$$

$$\alpha = \Psi^6 \tilde{\alpha}. \quad (3.14)$$

$\tilde{A}^{ij}$  is related to the shift and to the time derivative of the conformal metric,  $\tilde{u}_{ij} = \partial_t \tilde{\gamma}_{ij}$ , by

$$\tilde{A}^{ij} = \frac{1}{2\tilde{\alpha}} \left[ \left( \tilde{L}\beta \right)^{ij} - \tilde{u}^{ij} \right], \quad (3.15)$$

where  $\tilde{L}$  is the conformal longitudinal operator,

$$\left( \tilde{L}V \right)^{ij} = \tilde{\nabla}^i V^j + \tilde{\nabla}^j V^i - \frac{2}{3} \tilde{\gamma}^{ij} \tilde{\nabla}_k V^k. \quad (3.16)$$

We solve the extended conformal thin sandwich (XCTS) equations, which are a set of 5 coupled non-linear equations.

$$2\tilde{\alpha} \left[ \tilde{\nabla}_j \left( \frac{1}{2\tilde{\alpha}} (\tilde{L}\beta)^{ij} \right) - \tilde{\nabla}_j \left( \frac{1}{2\tilde{\alpha}} \tilde{u}^{ij} \right) - \frac{2}{3} \Psi^6 \tilde{\nabla}^i K - 8\pi \Psi^4 \tilde{J}^i \right] = 0, \quad (3.17)$$

$$\tilde{\nabla}^2 \Psi - \frac{1}{8} \Psi \tilde{R} - \frac{1}{12} \Psi^5 K^2 + \frac{1}{8} \Psi^{-7} \tilde{A}_{ij} \tilde{A}^{ij} + 2\pi \Psi^{-1} \tilde{E} = 0 \quad (3.18)$$

$$\tilde{\nabla}^2 (\tilde{\alpha} \Psi^7) - (\tilde{\alpha} \Psi^7) \left[ \frac{1}{8} \tilde{R} + \frac{5}{12} \Psi^4 K^2 + \frac{7}{8} \Psi^{-8} \tilde{A}_{ij} \tilde{A}^{ij} + 2\pi \Psi^{-2} (\tilde{E} + 2\tilde{S}) \right] = -\Psi^5 (\partial_t K - \beta^k \partial_k K). \quad (3.19)$$

These are solved for the conformal factor,  $\Psi$ , the densitized lapse,  $\alpha\Psi$ , and the shift,  $\beta^i$ .

The matter content of  $\Sigma(t)$  is determined by  $\tilde{E}$ ,  $\tilde{S}$ , and  $\tilde{J}^i$ . The free data are  $\gamma_{ij}$ ,  $\tilde{u}_{ij}$ ,  $K$  and  $\partial_t K$ .  $\tilde{u}_{ij} = 0$  and  $\partial_t K = 0$  are natural choices in a coordinate system corotating with the binary. The choice of the conformal metric will be discussed in section 3.3.

Let us now further discuss the matter content of the neutron star. The energy density of the fluid is  $\rho = \rho_0 (1 + \epsilon)$ , where  $\rho_0$  is the baryon density and  $\epsilon$  is the internal energy. The specific enthalpy of the fluid is

$$h = 1 + \epsilon + \frac{P}{\rho_0}. \quad (3.20)$$

It is convenient to introduce the following projections of the four velocity  $u^\mu$  and the three-velocity  $U^\mu$ :

$$u^\mu = \gamma_n (n^\mu + U^\mu), \quad (3.21)$$

$$U^\mu n_\mu = 0. \quad (3.22)$$

$$U_0^i = \frac{\beta^i}{\alpha}, \quad (3.23)$$

$$\gamma_0 = (1 - \gamma_{ij} U_0^i U_0^j)^{-1/2}, \quad (3.24)$$

$$\gamma_n = (1 - \gamma_{ij} U^i U^j)^{-1/2}, \quad (3.25)$$

$$\gamma = \gamma_n \gamma_0 (1 - \gamma_{ij} U^i U_0^j), \quad (3.26)$$

Following Tichy (2011), the three-velocity is written as the sum of an irrotational part (the gradient of a potential  $\phi$ ) and a rotational part  $W$ :

$$U^i = \frac{\Psi^{-4} \tilde{\gamma}^{ij}}{h \gamma_n} (\partial_j \phi + W_j). \quad (3.27)$$

$W$  is a freely chosen, divergence-free, vector field in this formalism; we will discuss this choice in section 3.3.

The matter fluid must satisfy the continuity equation and the Euler equation. Under the assumptions made in Tichy (2011), the continuity equation is a second order elliptic equation for the potential  $\phi$ :

$$\frac{\rho_0}{h} \nabla^\mu \nabla_\mu \phi + (\nabla^\mu \phi) \nabla_\mu \frac{\rho_0}{h} = 0. \quad (3.28)$$

Following Tichy (2011) this can be re-written as

$$\begin{aligned} \rho_0 \left\{ -\tilde{\gamma}^{ij} \partial_i (\partial_j \phi + W_j) + \frac{h\beta^i \Psi^4}{\alpha} \partial_i \gamma_n + hK\gamma_n \Psi^4 + \left[ \tilde{\gamma}^{ij} \tilde{\Gamma}_{ij}^k + \gamma^{ik} \partial_i \left( \ln \frac{h}{\alpha \Psi^2} \right) \right] (\partial_k \phi + W_k) \right\} \\ = \tilde{\gamma}^{ij} (\partial_i \phi + W_i) \partial_j \rho_0 - \frac{h\gamma_n \beta^i \Psi^4}{\alpha} \partial_i \rho_0. \end{aligned} \quad (3.29)$$

The Euler equation is solved for the specific enthalpy  $h$ . The solution is, as shown in Tichy (2011):

$$h = \sqrt{L^2 - (\nabla_i \phi + W_i) (\nabla^i \phi + W^i)}, \quad (3.30)$$

where

$$L^2 = \frac{b + \sqrt{b^2 - 4\alpha^4 ((\nabla_i \phi + W_i) W^i)^2}}{2\alpha^2}, \quad (3.31)$$

and

$$b = (\beta^i \nabla_i \phi + C)^2 + 2\alpha^2 (\nabla_i \phi + W_i) W^i. \quad (3.32)$$

The boundary condition on  $\phi$  at the surface of the neutron star can be deduced from the  $\rho_0 \rightarrow 0$  limit of the continuity equation:

$$\tilde{\gamma}^{ij} (\partial_i \phi + W_i) \partial_j \rho_0 = \frac{h\gamma_n \beta^i \Psi^4}{\alpha} \partial_i \rho_0. \quad (3.33)$$

Note that  $\phi$  is only solved for inside the neutron stars, while the metric variables are solved for everywhere. The boundary condition at infinity (which is in practice, in our computational grid, at  $R = 10^{10}$ ) are the requirement of a Minkowski metric in the

inertial frame (Foucart et al. (2008)):

$$\beta_0 = 0, \quad (3.34)$$

$$\alpha\Psi = 1, \quad (3.35)$$

$$\Psi = 1. \quad (3.36)$$

The interior of the black hole is excised from the computation domain. The boundary conditions at the surface of the black hole apparent horizon,  $\mathcal{H}$ , are (Cook & Pfeiffer (2004)):

$$\tilde{s}^k \nabla_k \log \Psi = -\frac{1}{4} \left( \tilde{h}^{ij} \tilde{\nabla}^i \tilde{s}_j - \Psi^2 h^{ij} K_{ij} \right) \quad \text{on } \mathcal{H} \quad (3.37)$$

$$\beta_\perp = \alpha \quad \text{on } \mathcal{H} \quad (3.38)$$

$$\beta_\parallel = \Omega_j^{BH} x_k \epsilon^{ijk} \quad \text{on } \mathcal{H} \quad (3.39)$$

where  $s^i = \Psi^{-2} \tilde{s}^i$  is the outward pointing unit normal to the apparent horizon surface,  $h^{ij}$  is the 2-metric on the surface,  $x_i$  are the Cartesian coordinates relative to the centre of the black hole and  $\Omega_j^{BH}$  is a free vector that determines the spin of the black hole. The force balance equation at the centre of the NS is

$$\nabla \log h = 0 \quad \text{on } x^i = c^i. \quad (3.40)$$

We can re-write this equation as

$$\nabla \ln (\alpha^2 - \gamma_{ij} \beta^i \beta^j) = -2 \nabla \ln \Gamma, \quad (3.41)$$

where

$$\Gamma = \frac{\gamma_n \left( 1 - \left( \beta^i + \frac{W^i \alpha}{h \gamma_n} \right) \frac{\nabla_i \phi}{\alpha h \gamma_n} - \frac{W_i W^i}{\alpha^2 \gamma_n^2} \right)}{\sqrt{1 - \left( \frac{\beta^i}{\alpha} + \frac{W^i}{h \gamma_n} \right) \left( \frac{\beta_i}{\alpha} + \frac{W_i}{h \gamma_n} \right)}}, \quad (3.42)$$

which is a second order equation for the orbital frequency  $\Omega$ , since  $\beta^i = \beta_0^i + \vec{\Omega} \times \vec{r} + \dot{a} \vec{r}$ , where  $\beta_0^I$  is the shift in the inertial frame. If desired, this equation can be solved to find a best guess for the orbital frequency. Alternatively, eccentricity removal techniques, such

as those used in Tacik et al. (2015) can be used to find the best value of the orbital frequency.

$W^i$  is chosen as as to give the NS a uniform rotational profile. Following our work in Tacik et al. (2015), we use

$$W^i = \epsilon^{ijk} \omega^j r^k, \quad (3.43)$$

where  $\epsilon^{ijk} = \{\pm 1, 0\}$ ,  $r^k$  is the position vector relative to the centre of the star, and  $\omega^j$  is a freely chosen constant vector.

The angular momentum of the black hole is computed as (Foucart et al. (2008)):

$$S = \frac{1}{8\pi} \oint_{\mathcal{H}} \phi^i s^j K_{ij} dA. \quad (3.44)$$

In a space-time with azimuthal symmetry,  $\phi^i$  would represent the exact azimuthal Killing vector field generated by this symmetry. Since azimuthal symmetry is not present in a binary system, we instead use an *approximate* Killing vector. It is computed by solving a shear minimization eigenvalue problem - see Cook & Whiting (2007); Lovelace et al. (2008) for details. The dimensionless spin is defined as

$$\chi = \frac{S}{M^2} \quad (3.45)$$

where  $M$  is the Christodoulou mass

$$M^2 = M_{\text{irr}}^2 + \frac{S^2}{4M_{\text{irr}}^2}. \quad (3.46)$$

The irreducible mass is related to the surface area of the horizon

$$M_{\text{irr}} = \sqrt{A/16\pi}. \quad (3.47)$$

The same method is used to compute the dimensionless spin of the neutron star. In particular we use Eq. 3.44, with  $\mathcal{H}$  replaced by the neutron star's surface, as defined in Eq. to compute the star's angular momentum. Its Arnowitt-Deser-Misner (ADM) mass is used as the normalization to compute its dimensionless spin. In particular, we use the



ADM mass of an analogous rotating star with the same angular momentum in isolation, since the ADM mass of the star in a binary is not directly measurable. Tacik et al. (2015) showed that this method of computing neutron star spin was robust and accurate.

### 3.3 Numerical Methods

The XCTS equations (eqs. (3.17) to (3.19) and the continuity equation (Eq. 3.29 for  $\phi$ ) form a set of six non-linear coupled elliptic equations that we must now solve. We use the pseudo-spectral multi-grid elliptic solver developed in Pfeiffer et al. (2003) and enhanced in Foucart et al. (2008) to incorporate matter. The computational domain is divided into a number of subdomains. A small cube is placed at the centre of the NS. Overlapping this cube is a spherical shell whose outer boundary deforms to fit the NS surface. These are surrounded by an additional spherical shell. The black hole is represented by two concentric spherical shells. Their inner boundary is required to be an apparent horizon. Three rectangular parallelepipeds surround the axis passing through the centres of the Bh and the Ns - one between them and one on each side of the objects. An additional eight cylindrical shells are placed around the same axis to cover the intermediate field region. The far-field region is covered by a large spherical shell whose outer boundary is placed at  $R = 10^{10}$  using an inverse radial mapping. This domain is visualized in Fig. 3.1.

All variables (metric and hydrodynamical) are decomposed on sets of basis functions on each subdomain. Finite difference schemes are needed for hydrodynamical quantities during evolutions so as to capture shocks, but for initial data, where shocks are not present, spectral methods are suitable and exponential convergence can be achieved. The resolution of each domain is synonymous with the number of collocation points used. They are chosen manually at the start of the initial data solve, and then modified several

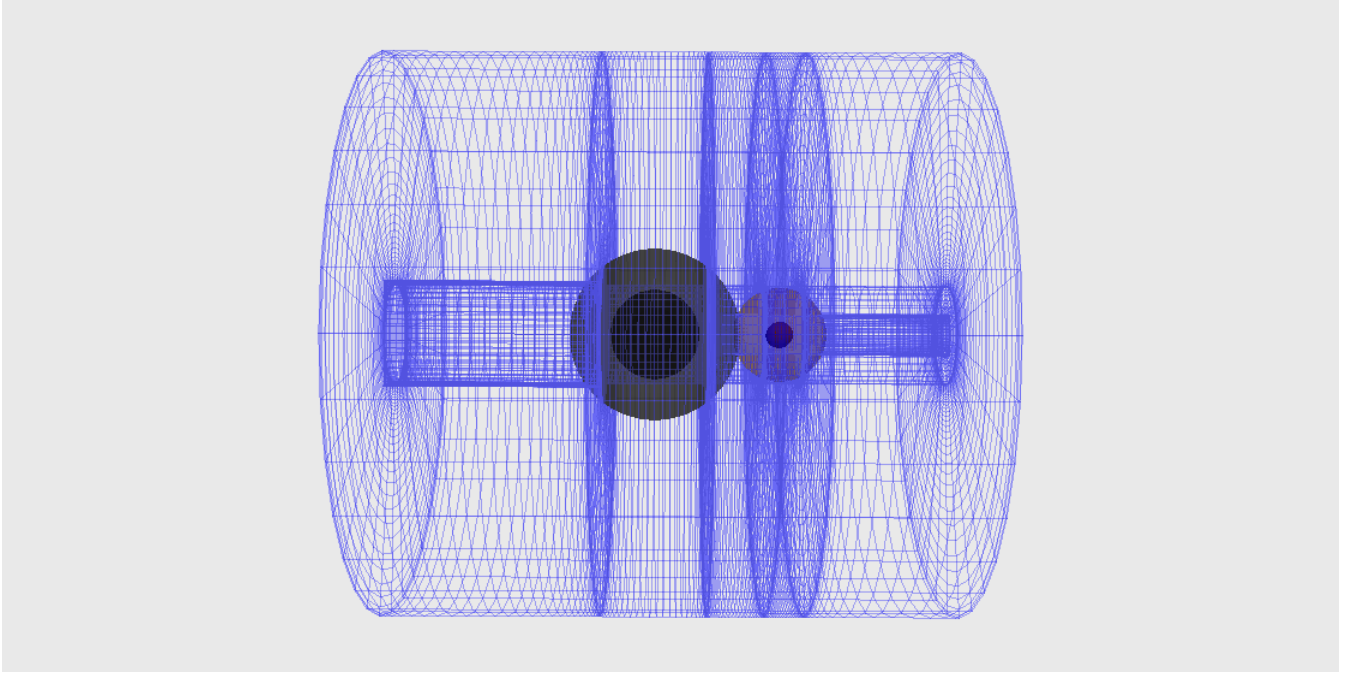


Figure 3.1: Visualization of the Bh-Ns domain decomposition. The black object on the left is the black hole and the orange object on the right is the neutron star. The blue wireframes represent the various cylinders and rectangular parallelepipeds in the domain. [\[Make this look nicer\]](#)

times using an adaptive scheme (see step To discuss the resolution of the computational domain for the purpose of convergence tests, we will use the notation

$$N^{1/3} = \left( \sum N_i \right)^{1/3}, \quad (3.48)$$

where we are summing the colocation points of all of the subdomains. This gives an indication of the average resolution per dimension. A typical initial data solve starts with,  $N^{1/3} \sim 33$  and end with  $N^{1/3} \sim 80$

Construction of initial data begins by choosing values for the physical parameters in the problem we aim to achieve. In particular, these are: parameters of the black hole,

- The black hole mass,  $M_{\text{BH}}$ ,
- The black hole's target dimensionless spin vector,  $\vec{\chi}_{\text{BH}}$ .

parameters of the neutron star,

- The neutron star's baryon mass,  $M_b$ ,
- The neutron star's equation of state,
- The neutron star's spin vector,  $\omega^i$ ,

and orbital parameters,

- The separation between the centres of the Bh and Ns,  $D$ ,
- The orbital angular velocity,  $\Omega_0$ ,
- The initial infall velocity parameter,  $\dot{a}$ .

Additionally, a prescription is required for the free metric variables,  $\tilde{g}_{ij}$  and  $K$ . We use the following: near the black hole they are equal to the values for a black hole with the same spin and boost velocity, written in Kerr-Schild coordinates. Near the neutron star, they are a conformally flat metric and  $K = 0$ . They fall-off from the black hole to the neutron star with a function of the form  $e^{(-r/w)^4}$ , where  $w$  is half the coordinate separation between them.

Let's now discuss the algorithm we use to solve for the initial data.

1. If this is the first resolution (i.e. step 11 has not been completed once yet), set  $\omega^i = 0$ , otherwise set to the desired value. This has been found to help with overall convergence. Additionally, impose a maximum radius out to which to apply  $W^i = \epsilon^{ijk}\omega^j r^k$ , otherwise low density material at high radius can lead to spurious large velocities, especially when the neutron star spin is large.
2. Solve the non-linear XCTS equations for the metric variables (eqs. (3.17) to (3.19))  $X = (\beta^i, \Psi, \alpha\Psi)$  assuming the matter source terms are fixed. Update the metric variables using a relaxation scheme

$$X^{n+1} = \lambda X^* + (1 - \lambda)X^n, \quad (3.49)$$

where  $X^*$  is the result found by solving the XCTS equations, and  $X^n$  is the previous value of  $X$ . We use  $\lambda = 0.3$ .

3. If both the Ns and Bh have either aligned spin or zero spin, impose equatorial symmetry. This will be speed convergence and decrease computational cost.
4. If already at a sufficiently high AMR resolution, skip to step 8, otherwise proceed to step 5. We generally find that after completed the first four resolutions, the stellar and black hole parameters are already computed to a good enough accuracy, so therefore those steps can be skipped to decrease computational cost.
5. Locate the surface of the star. The surface of the star is represented in terms of spherical harmonics

$$R(\theta, \phi) = \sum_{m,l}^{m_{\max}, l_{\max}} c_{lm} Y^{lm}(\theta, \phi). \quad (3.50)$$

The coefficients  $c_{lm}$  are determined by solving the relation  $h(R(\theta, \phi)) = 1$ . We generally use  $l_{\max} = 11$ .

6. Compute the ADM linear momentum  $P_{\text{ADM}}$ , as

$$P_{\text{ADM}}^i = \frac{1}{8\pi} \oint_{S_\infty} K^{ij} dS_j. \quad (3.51)$$

If its norm has changed by less than 10% in the last iteration, move the centre of the BH so as to zero-out the momentum of the system. In particular, find  $\delta c$  satisfying  $\vec{\delta c} \times \vec{\Omega}_0 = \vec{P}_{\text{ADM}}$ . Additionally, modify the radius of the excision surface to drive  $M_{\text{BH}}$  to the desired value by applying (Buchman et al. (2012))

$$\delta r_{\text{ex}} = -r_{\text{ex}} \frac{M_{\text{BH}} - M_{\text{BH}}^*}{M_{\text{BH}}}, \quad (3.52)$$

where  $M_{\text{BH}}$  is the measured value in the initial data solve and  $M_{\text{BH}}^*$  is the desired value.

7. Compute the spin of the BH by evaluating Eq. 3.44. Then modify the vector  $\Omega_{\text{BH}}^i$  in Eq. 3.39 to drive the black hole spin to the target value, by applying (Buchman et al. (2012))

$$\delta\Omega_{\text{BH}}^i = -\frac{\chi_{\text{BH}}^i - \chi_{\text{BH}}^{*i}}{4M} + \frac{M_{\text{BH}} - M_{\text{BH}}^*}{4M_{\text{BH}}^2} \chi_{\text{BH}}^i, \quad (3.53)$$

where  $\chi_{\text{BH}}^i$  is the computed black hole spin, and  $\chi_{\text{BH}}^{*i}$  is the target spin.

8. If desired, adjust the orbital angular frequency using Eq. 3.41, which, after expanding the shift as  $\beta^i = \beta_0^i + \vec{\Omega} \times \vec{r} + \dot{a}\vec{r}$ , is a second-order equation for  $\Omega$ .

9. Fix the Euler constant by evaluating the integral

$$M_B = \int \rho_0 \Psi^6 \gamma_n dV \quad (3.54)$$

as a function of the Euler constant  $C$  (since  $C$  is a function of  $h$  and  $h$  is a function of  $\rho_0$ ), and using the secant method to drive the baryon mass to the desired value.

10. Solve the elliptic equations for the velocity potential,  $\phi$ , and update using the same relaxation scheme as described above.
11. Check whether all equations satisfied to the desired accuracy. If so, proceed to step 12. Otherwise return to step 2.
12. Compute the truncation error for the current solution by examining the spectral coefficients of the metric variables. If the truncation error is too large (generally we use  $10^{-9}$  as the criterion), adjust the number of grid points and return to step 1. This adaptive refinement is based on the target truncation error and the measured convergence rate of the solution. See Szilágyi (2014) for a complete description of this procedure.

## 3.4 Results

### 3.4.1 Initial Data Set Parameters

Let us begin by discussing the parameters for the initial data sets that will be used in this work. We start from the six BH-NS configurations described in Table 1 of Foucart et al. (2013). All binaries have a mass ratio  $q = 7$  and a black hole spin magnitude of  $\chi_{\text{BH}} = 0.9$ . The neutron star in each binary has an ADM mass of  $M_{\text{ADM}}^{\text{Ns}} = 1.4M_{\odot}$  - note that this is distinct from the ADM energy,  $E_{\text{ADM}}$  of the full binary. In practice, this means that it is fixed to have the same baryon mass as that of an isolated, non-spinning neutron star with ADM mass  $1.4M_{\odot}$ , with the same equation of state. We explore three different Ns equations of state. All three are polytropic equations of state ( $P = \kappa\rho^{\Gamma}$ ) with  $\Gamma = 2$ , but vary in terms of  $\kappa$ , resulting in different neutron star compactnesses. The values of  $\kappa$  used are 84.28, 92.12, 101.45, which result in compactnesses of 0.170, 0.156, 0.144, and radii of approximately  $12km$ ,  $13km$ ,  $14km$ , respectively, for non-spinning neutron stars with ADM Mass  $1.4M_{\odot}$ . We will use the notation  $R12$ ,  $R13$  and  $R14$  to refer to these configurations, respectively. The  $R12$  and  $R13$  configurations are the only sets with the black hole spin aligned with the orbital angular momentum. For  $R14$ , we also consider precessing black hole spins spanning angles of  $20^{\circ}$ ,  $40^{\circ}$  and  $60^{\circ}$  with the orbital angular momentum. The non-parallel part of the black hole spin is set parallel to the  $\hat{x}$  axis. In each case the initial separation between the black hole and the neutron star is  $D = 7.44M$ , where  $M = M_{\text{BH}} + M_{\text{ADM}}^{\text{NS}}$  is the total mass of the binary. The initial infall velocity parameter  $\dot{a}_0$  is set to 0. The orbital angular velocity,  $\Omega_0$ , is the same as in Foucart et al. (2013) and is indicated in table 3.1. The above constitutes 6 different configurations.

For each of these 6 configurations, we choose an additional 6 configurations of neutron star spins (thus 36 total configurations). In particular we choose three directions - aligned with the orbital angular momentum, anti-aligned with the orbital angular momentum,

and completely in the orbital plane, parallel to the  $\hat{x}$  direction. For each of these 3 directions, we use a “high-spin” and a “low-spin”. These are typically  $\chi_{NS} \sim 0.4$  and  $\chi_{NS} \sim 0.1$ , respectively. In our naming notation, we use a large arrow ( $\Uparrow$ ) for the “high-spin” configurations and a small arrow ( $\uparrow$ ) for the “low-spin”, with the direction of the arrow indicating the direction of the NS spin vector. The full parameters of the initial data sets are summarized in Table 3.1. In particular, the name of the run, the black hole spin direction, the baryon mass of the neutron star, the orbital angular velocity of the system, the approximate number of orbits before merger, the neutron star spin vector  $\vec{\omega}_{NS}$ , and the measured dimensionless spin of the neutron star. Note that the number of orbits is taken from Foucart et al. (2013), and does not account for the neutron star spin.

Name	$\Theta_{BH}$	$M_{NS}^B$	$M\Omega_0$	$\sim N_{orb}$	$\vec{\omega}_{NS}$	$\vec{\chi}_{NS}$
R12i0 $\Uparrow$	$0^\circ$	1.5212	0.0413	10.25	$0.00667\hat{z}$	$0.0995\hat{z}$
R12i0 $\uparrow$	$0^\circ$	1.5212	0.0413	10.25	$0.0225\hat{z}$	$0.4093\hat{z}$
R12i0 $\Downarrow$	$0^\circ$	1.5212	0.0413	10.25	$-0.00667\hat{z}$	$-0.0895\hat{z}$
R12i0 $\downarrow$	$0^\circ$	1.5212	0.0413	10.25	$-0.0225\hat{z}$	$-0.4030\hat{z}$
R12i0 $\rightarrow$	$0^\circ$	1.5212	0.0413	10.25	$0.00667\hat{x}$	$0.0936\hat{x}$
R12i0 $\Rightarrow$	$0^\circ$	1.5212	0.0413	10.25	$0.0225\hat{x}$	$0.3989\hat{x}$
R13i0 $\Uparrow$	$0^\circ$	1.5128	0.0413	10.15	$0.00555\hat{z}$	$0.0997\hat{z}$
R13i0 $\uparrow$	$0^\circ$	1.5128	0.0413	10.15	$0.019\hat{z}$	$0.3911\hat{z}$
R13i0 $\Downarrow$	$0^\circ$	1.5128	0.0413	10.15	$-0.00555\hat{z}$	$-0.0845\hat{z}$
R13i0 $\downarrow$	$0^\circ$	1.5128	0.0413	10.15	$-0.019\hat{z}$	$-0.3793\hat{z}$
R13i0 $\rightarrow$	$0^\circ$	1.5128	0.0413	10.15	$0.00555\hat{x}$	$0.0913\hat{x}$
R13i0 $\Rightarrow$	$0^\circ$	1.5128	0.0413	10.15	$0.019\hat{x}$	$0.3771\hat{x}$
R14i0 $\Uparrow$	$0^\circ$	1.5049	0.0413	9.85	$0.005541\hat{z}$	$0.1188\hat{z}$
R14i0 $\uparrow$	$0^\circ$	1.5049	0.0413	9.85	$0.017\hat{z}$	$0.4109\hat{z}$
R14i0 $\Downarrow$	$0^\circ$	1.5049	0.0413	9.85	$-0.005541\hat{z}$	$-0.0965\hat{z}$
R14i0 $\downarrow$	$0^\circ$	1.5049	0.0413	9.85	$-0.017\hat{z}$	$-0.3915\hat{z}$

R14i0 $\rightarrow$	0°	1.5049	0.0413	9.85	0.005541 $\hat{x}$	0.1066 $\hat{x}$
R14i0 $\Rightarrow$	0°	1.5049	0.0413	9.85	0.017 $\hat{x}$	0.3907 $\hat{x}$
R14i20 $\uparrow$	20°	1.5049	0.0412	9	0.005541 $\hat{z}$	0.1188 $\hat{z}$
R14i20 $\uparrow\uparrow$	20°	1.5049	0.0412	9	0.017 $\hat{z}$	0.4110 $\hat{z}$
R14i20 $\downarrow$	20°	1.5049	0.0412	9	-0.005541 $\hat{z}$	-0.0964 $\hat{z}$
R14i20 $\downarrow\downarrow$	20°	1.5049	0.0412	9	-0.017 $\hat{z}$	-0.3915 $\hat{z}$
R14i20 $\rightarrow$	20°	1.5049	0.0412	9	0.005541 $\hat{x}$	0.1064 $\hat{x}$
R14i20 $\Rightarrow$	20°	1.5049	0.0412	9	0.017 $\hat{x}$	0.3905 $\hat{x}$
R14i40 $\uparrow$	40°	1.5049	0.0412	8.5	0.005541 $\hat{z}$	0.1193 $\hat{z}$
R14i40 $\uparrow\uparrow$	40°	1.5049	0.0412	8.5	0.017 $\hat{z}$	0.4117 $\hat{z}$
R14i40 $\downarrow$	40°	1.5049	0.0412	8.5	-0.005541 $\hat{z}$	-0.0961 $\hat{z}$
R14i40 $\downarrow\downarrow$	40°	1.5049	0.0412	8.5	-0.017 $\hat{z}$	-0.3908 $\hat{z}$
R14i40 $\rightarrow$	40°	1.5049	0.0412	8.5	0.005541 $\hat{x}$	0.1064 $\hat{x}$
R14i40 $\Rightarrow$	40°	1.5049	0.0412	8.5	0.017 $\hat{x}$	0.3905 $\hat{x}$
R14i60 $\uparrow$	60°	1.5049	0.0415	7	0.005541 $\hat{z}$	0.1200 $\hat{z}$
R14i60 $\uparrow\uparrow$	60°	1.5049	0.0415	7	0.017 $\hat{z}$	0.4132 $\hat{z}$
R14i60 $\downarrow$	60°	1.5049	0.0415	7	-0.005541 $\hat{z}$	-0.0954 $\hat{z}$
R14i60 $\downarrow\downarrow$	60°	1.5049	0.0415	7	-0.017 $\hat{z}$	-0.3898 $\hat{z}$
R14i60 $\rightarrow$	60°	1.5049	0.0415	7	0.005541 $\hat{x}$	0.1061 $\hat{x}$
R14i60 $\Rightarrow$	60°	1.5049	0.0415	7	0.017 $\hat{x}$	0.3903 $\hat{x}$

Table 3.1: Full set of parameters of the 36 sets of initial data constructed here.  $\theta_{\text{BH}}$  is the angle between the black hole spin and the orbital angular momentum,  $M_{\text{NS}}^B$  is the baryon mass of the neutron star,  $M\Omega_0$  is the orbital frequency of the binary,  $\sim N_{\text{orb}}$  is the approximate number of orbits before merger,  $\vec{\omega}_{\text{NS}}$  is the spin vector of the neutron star as defined in Eq. 3.43, and  $\vec{\chi}_{\text{NS}}$  is the measured dimensionless spin of the neutron star.

Although we do not perform evolutions of any of these initial data sets, in principle



these initial data sets could be easily used to extend the work of Foucart et al. (2013). For example, it was found that the size of the neutron star, varying from  $12km$  to  $14km$  can greatly affect the onset of neutron star disruption, and thus the disk produced and the electromagnetic signal that would be produced. Given such sensitivity to the NS parameters, it is natural to think that sensitivity to the NS spin should be tested. If the material is less strongly bound to the star because of centrifugal forces arising from the spin, then the stars should disrupt earlier.

### 3.4.2 Convergence of the Initial Data Solver

To assess the convergence of the initial data solver we will begin by looking at the convergence of the iterative part of the solver. That is, the convergence of steps 1-12 in the iterative procedure described above. We will first focus on one particular initial data set of the 36 in Tab 3.1 - namely the R14i60 $\uparrow$  initial data set. The results we present for R14i60 $\uparrow$  are representative for all of the 36 sets considered.

We begin by looking at the convergence of the Euler constant,  $C$ . In figure 3.2 we plot the absolute difference in  $C$  between neighbouring iterations for the eight different resolutions used in the initial data solve. In the figure we see that at a given resolution these differences decrease exponentially with iteration as expected for the relaxation scheme employed (cf. Eq. 3.49). Meanwhile the differences also decrease with increasing resolution. This all shows that the initial data solver is working as it should. Note that although we've only shown this plot for the R14i60 $\uparrow$  initial data set, we find similar results for all the other initial data sets we consider.

Next, we will look at the properties of the black hole to verify that they converge as expected in the presence of a spinning neutron star. Again, we will focus on the R14i60 $\uparrow$  run, and look at the black hole spin parameter  $a = J/M = M\chi$ , which is controlled by

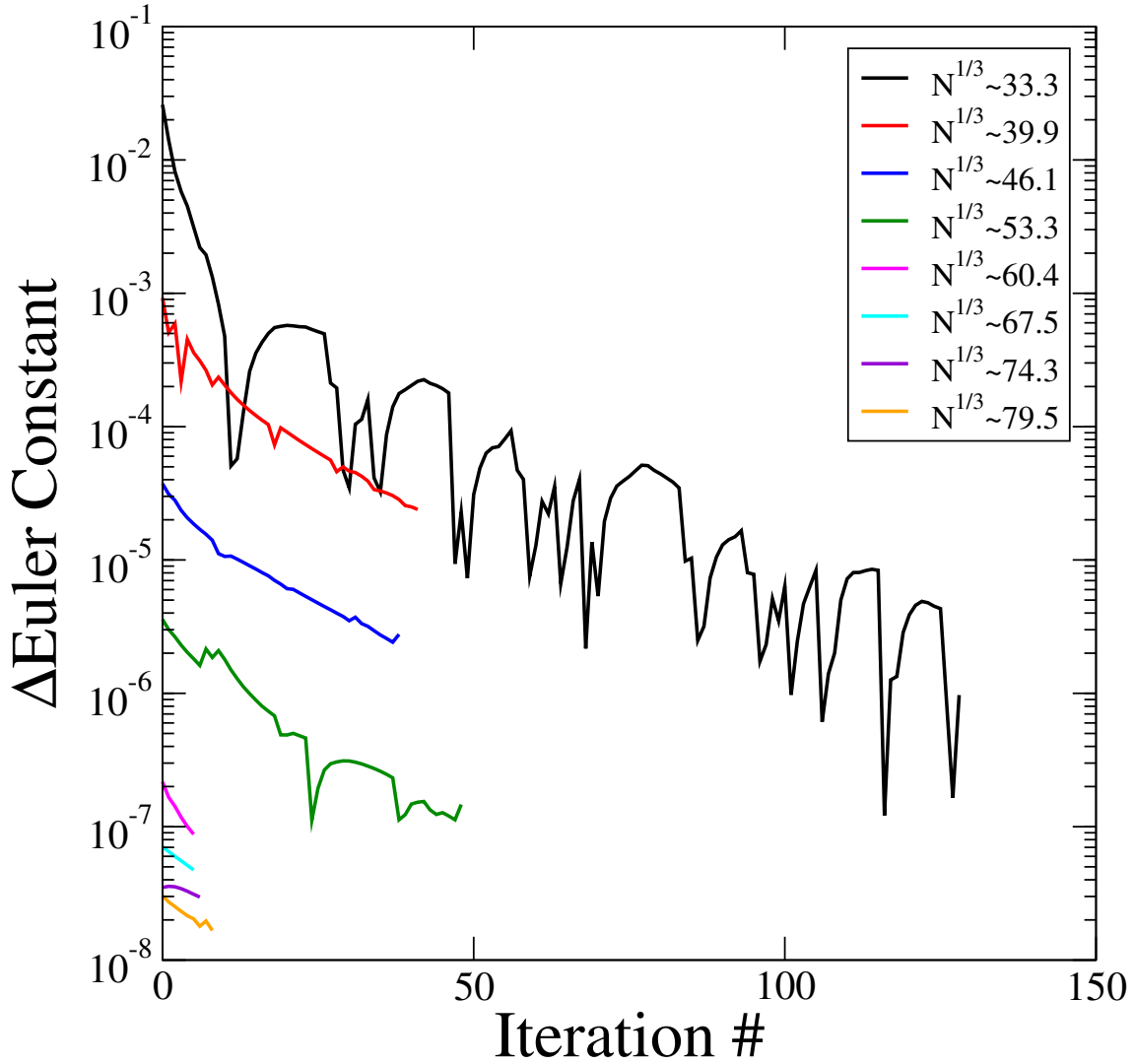


Figure 3.2: Absolute difference between neighbouring iterations of the Euler constant for the R14i60 $\uparrow$  initial data set. The eight curves are the eight different resolutions used in the initial data solve.

the parameter  $\Omega_j^{\text{BH}}$  in Eq. 3.39. The target values are

$$a = \chi_{\text{BH}} M_{\text{BH}} \quad (3.55)$$

$$= q \chi_{\text{BH}} M_{\text{NS}}^{\text{ADM}} \quad (3.56)$$

$$a_x = q \chi_{\text{BH}} (\sin 60^\circ) M_{\text{NS}}^{\text{ADM}} \quad (3.57)$$

$$a_z = q \chi_{\text{BH}} (\cos 60^\circ) M_{\text{NS}}^{\text{ADM}} \quad (3.58)$$

We also consider the convergence of the irreducible mass of the black hole,  $M_{\text{irr}}$ . It is controlled by the size of the excision surface, and satisfies the relation

$$M_{\text{BH}}^{\text{irr}} = \sqrt{\frac{A_{\text{AH}}}{16\pi}} \quad (3.59)$$

$$(M_{\text{BH}}^{\text{ADM}})^2 \left( (M_{\text{BH}}^{\text{irr}})^2 - \frac{a^2}{4} \right) = (M_{\text{BH}}^{\text{irr}})^4 \quad (3.60)$$

In figure 3.3 we plot the fractional difference between the measured black hole spin and the target value, for both the x and z directions, as well as the fractional difference between the measured black hole irreducible mass and the target value. The difference is plotted as a function of iteration, for four different resolutions. Note that the previous plot had eight different resolutions, while this one only has four. This is because the black hole spin is only computed for the first four resolutions - afterwards it is no longer solved adjusted (cf. Step 4) We note that in general we see a decrease in this difference with iteration, especially at the first resolution, therefore showing that the iterative solver is correctly driving the the black hole properties to the target values. We also note that this difference decrease with resolution, and that we are able to achieve an accuracy of about  $10^{-5}$  in the BH spin and mass. **Can we understand this sawtooth pattern?**

Having now established the convergence of the iterative procedure, we turn now to establish the convergence with resolution of the global properties of the solution, continuing to focus on the R14i60 $\uparrow$  ID set. We begin by looking at the Hamiltonian and momentum constraints for the R14i60 $\uparrow$  initial data set. The Hamiltonian constraint is computed as

$$H = \left\| \frac{R_\Psi}{8\Psi^5} \right\| \quad (3.61)$$

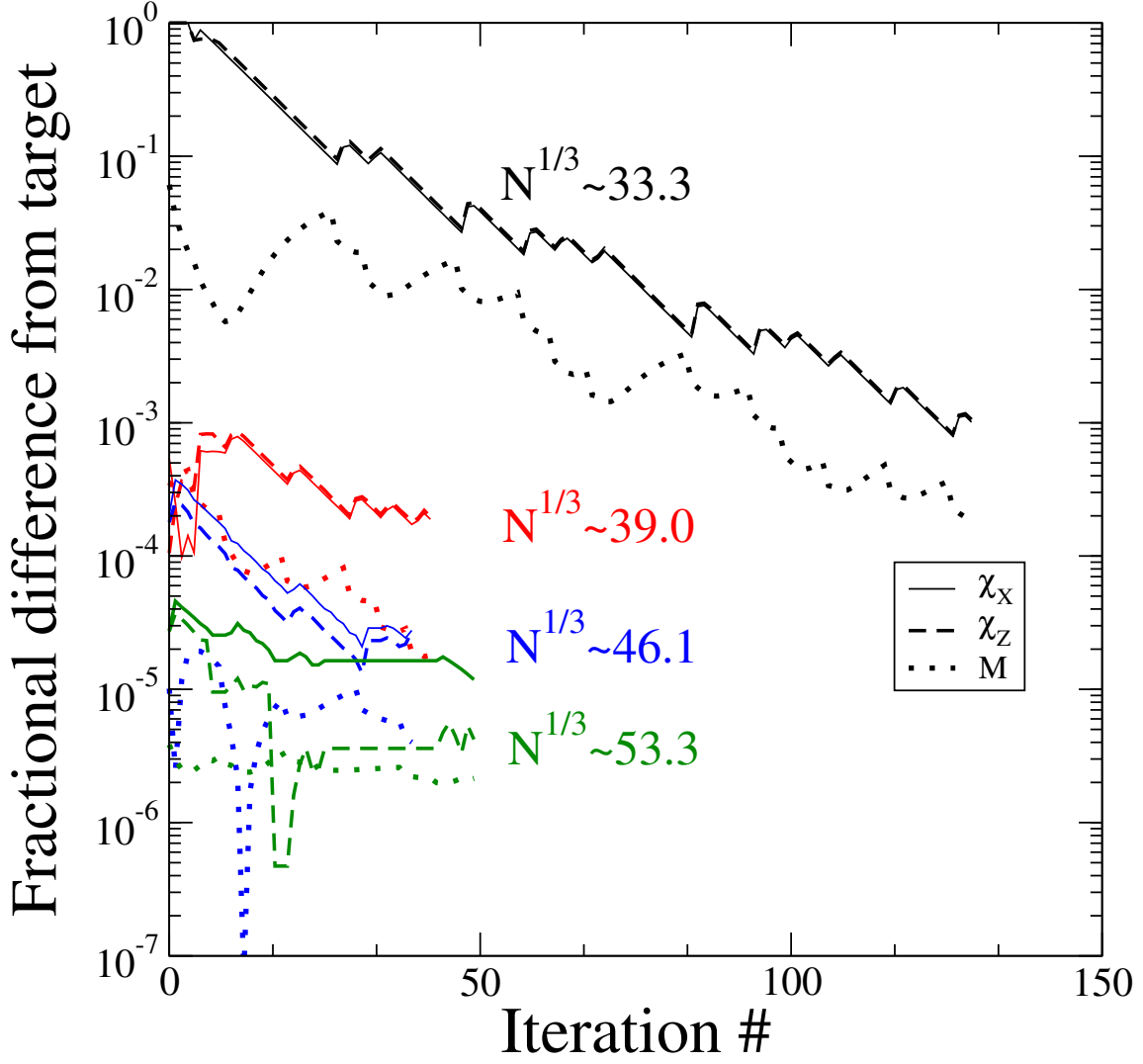


Figure 3.3: Plotted is the fractional difference from the target black hole spin and black hole mass in the R14i60 $\uparrow$  initial data set as a function of iteration. The four colours represent the four different resolutions at which the black hole spin is measured. The solid curves are for the  $\hat{x}$  component of the BH spin, the dashed curves for the  $\hat{z}$  component of the BH spin, and the dotted curves are for the irreducible mass of the BH.

where  $R_\Psi$  is the residual of Eq. 3.18 and  $||.||$  represents the  $L2$  norm over the computational domain. Similarly, the momentum constraint is computed as

$$M = ||\frac{R_\beta}{2\alpha\Psi^4}|| \quad (3.62)$$

where  $R_\beta$  is the residual of Eq. 3.17. The constraints for this ID set are shown in figure 3.4. We find exponential convergence in the constraints, as expected for spectral methods. The most notable feature is that at the second resolution the constraints are higher than would be expected from the trend, otherwise. This is because the neutron star spin is only "turned on" during the second resolution (cf. step 1), and so an additional amount of solver time is needed to adjust to this change.

**Improve wording of this paragraph** Finally, we look at the properties of the neutron star. As noted in Eq. 3.50, the neutron star surface is expressed as a sum of spherical harmonics. To evaluate the convergence of the surface location, we define the quantity,

$$\Delta c(N) = \sqrt{\sum_{l,m}^{l_{\max}, m_{\max}} (c_{lm}(N) - c_{lm}^*)^2} \quad (3.63)$$

where  $N$  represents the current resolution, and  $*$  represents the highest resolution. This quantity is plotted in figure 3.5. Similar to the black hole surface, the neutron star surface is only computed for the first four resolutions, and so we have three data points shown. We find exponential convergence in this quantity. We also look at the convergence of the neutron star spin  $\chi_{\text{NS}}$  measured at each resolution. In figure 3.5, we plot the fractional difference in  $\chi_{\text{NS}}$  between neighbouring resolutions. That is, we plot  $\Delta\chi = |\frac{\chi(N+1) - \chi(N)}{\chi(N)}|$ . We find apparent exponential convergence, although there are two distinctly different slopes in the data, with the slope becoming more shallow at high resolution. This is likely because we have stopped measuring the NS surface at this point, i.e., after the fourth resolution. However, we are able to measure the spin to an accuracy of about  $10^{-6}$ . We have omitted the first data point in this curve because the neutron star spin is not turned on in the first resolution, so by construction the first data point is artificially large.

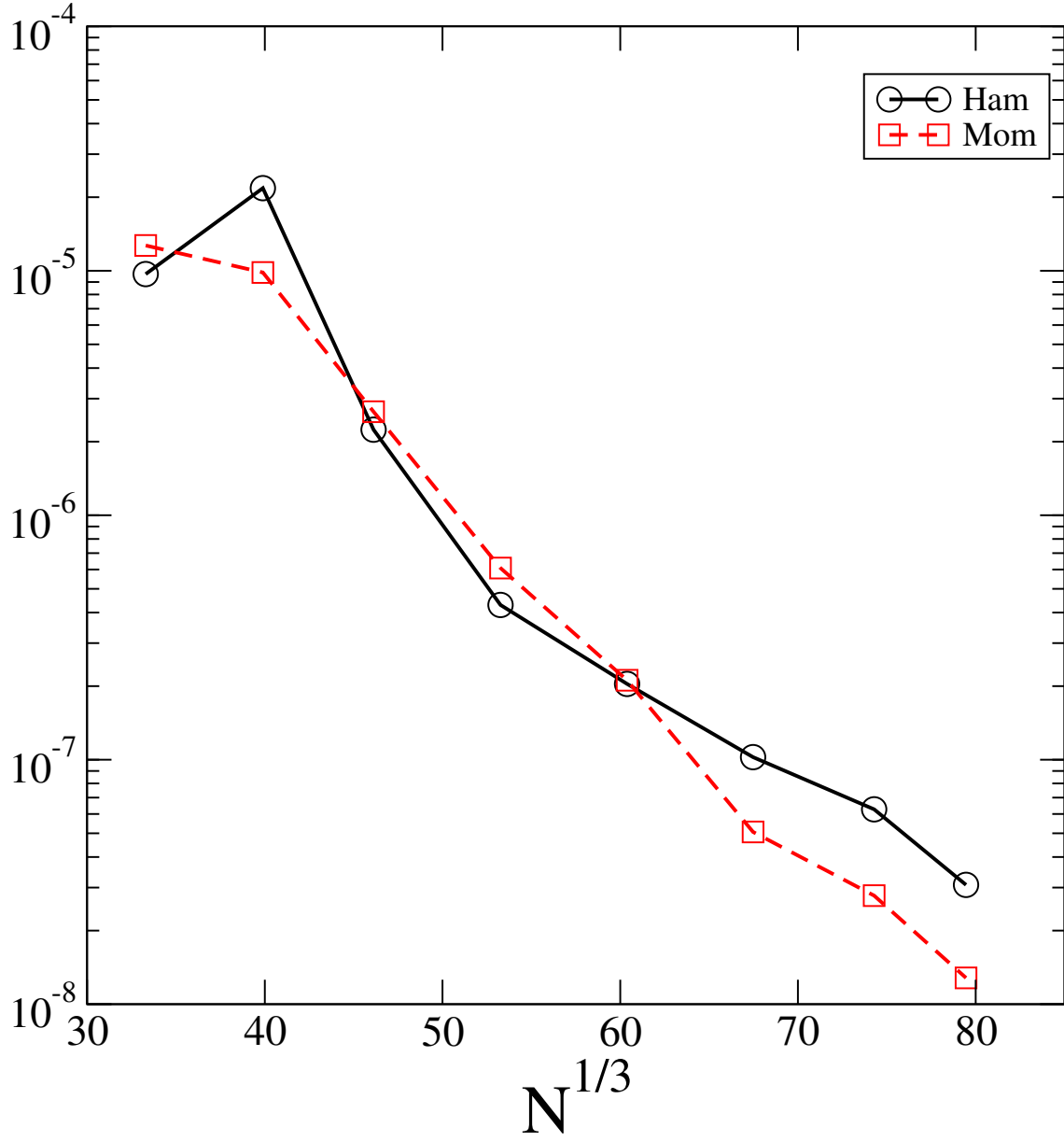


Figure 3.4: The Hamiltonian and momentum constraints for the R14i60 $\uparrow$  initial data set as a function of resolution. We find exponential convergence in both.

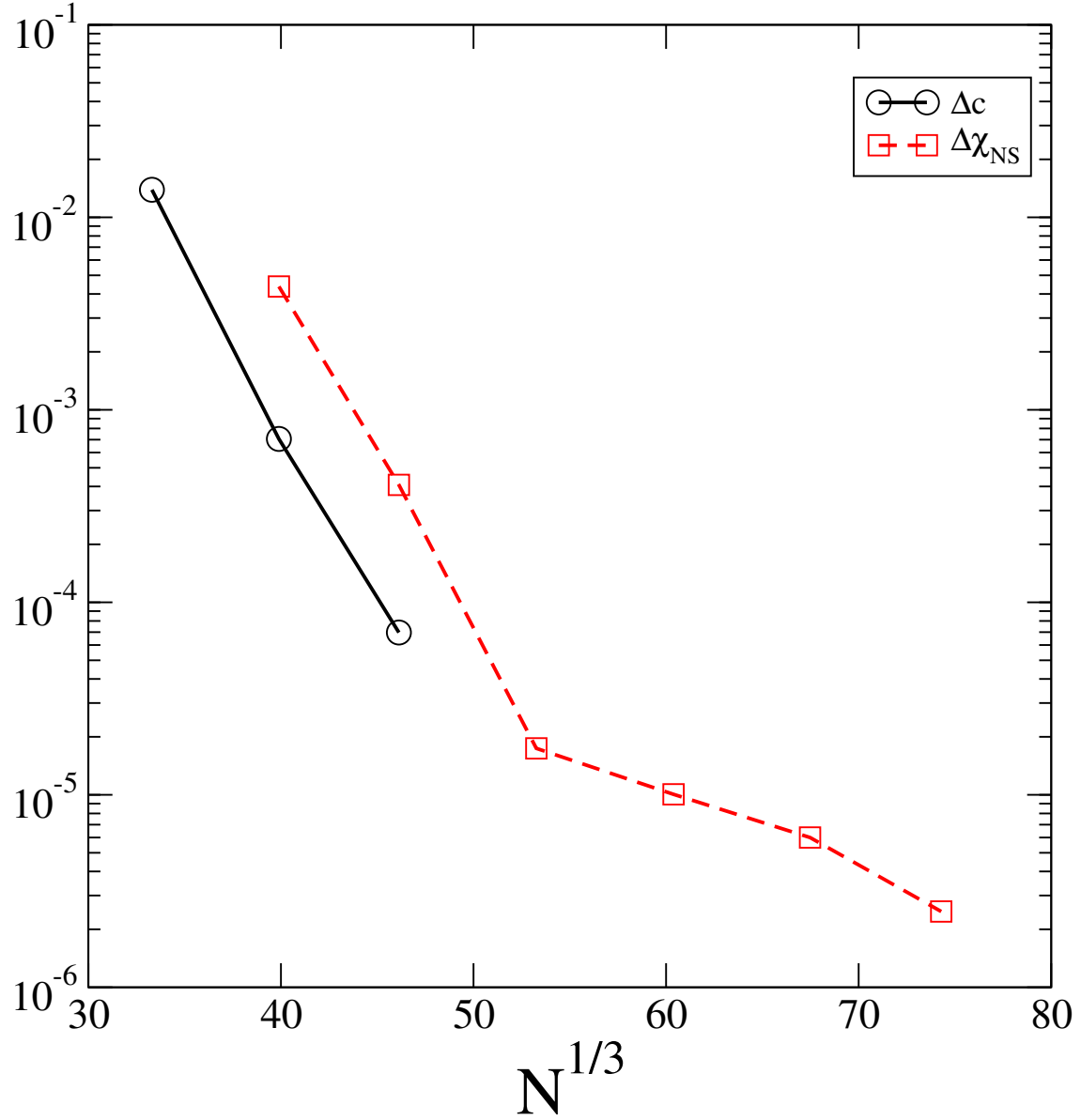


Figure 3.5: [Re-visit this plot](#) Accuracy of neutron star properties. Plotted are, as a function of resolution the accuracy of the computation of the neutron star surface,  $\Delta c$ , as defined in Eq. 3.63 (solid black curve), and the fractional difference between neighbouring resolutions in the measured neutron star spin  $\chi_{NS}$  (dashed red curve). The first data point is omitted for the latter curve since it is artificially high by construction - the Ns spin is set to zero during the first resolution. This is for the R14i60 $\uparrow$  ID set.

The above data all show that we have established the convergence of our initial data solver, by showing exponential convergence of the iterative solver, the black hole properties, neutron star properties, and the constraints.

### 3.4.3 Other Initial Data Sequences

In addition to the parameters discussed above, we consider several other sequences of Bh-Ns initial data sets to verify the robustness of the solutions across the whole parameter space. First, we consider a sequence of where we vary the neutron star spin from  $\chi_{\text{NS}} = 0$  to  $\chi_{\text{NS}} \sim 0.7$ , keeping it aligned with the orbital angular momentum. In these initial data sets, the other binary parameters are the same as in the **R14i0** runs. Namely, the neutron star mass, equation of state, black hole mass, black hole spin, initial separation and orbital angular frequency.

Next, we consider a sequence of runs where we vary the black hole spin from  $\chi_{\text{BH}} = 0$  to  $\chi_{\text{BH}} = 0.99$ , while keeping the other binary parameters as in the **R14i0** run.

Finally, we consider a sequence of runs where we vary the mass ratio from  $q = 2$  to  $q = 10$ . In these runs the other binary parameters are the same as in the **R14i0** run. In particular, the orbital parameters  $M\Omega$  and  $D/M$  are constant. While not the most accurate way of choosing these parameters, as it is only correct to Newtonian order, it is a very simple method that is sufficient for our purposes, as it will only induce a small orbital eccentricity. To assess the accuracy of this approximation, we use the post-Newtonian expansion in Eq. 228 of Blanchet (2006):

$$\Omega^2 = \frac{GM}{r^3} \left( 1 + (-3 + \nu)\gamma + \left( 6 + \frac{41}{4}\nu + \nu^2 \right) \gamma^2 + \dots \right) \quad (3.64)$$

where  $\nu$  is the symmetric mass ratio,  $\nu = q/(1+q)^2$ , and  $\gamma = GM/Dc^2$ . Keeping  $D$  and  $M$  constant, the quantity  $M\Omega$  varies by approximately 3% in the mass ratio range we consider. Thus, while this approximation will induce a small eccentricity of a similar order, it's not a large enough difference to invalidate our results.



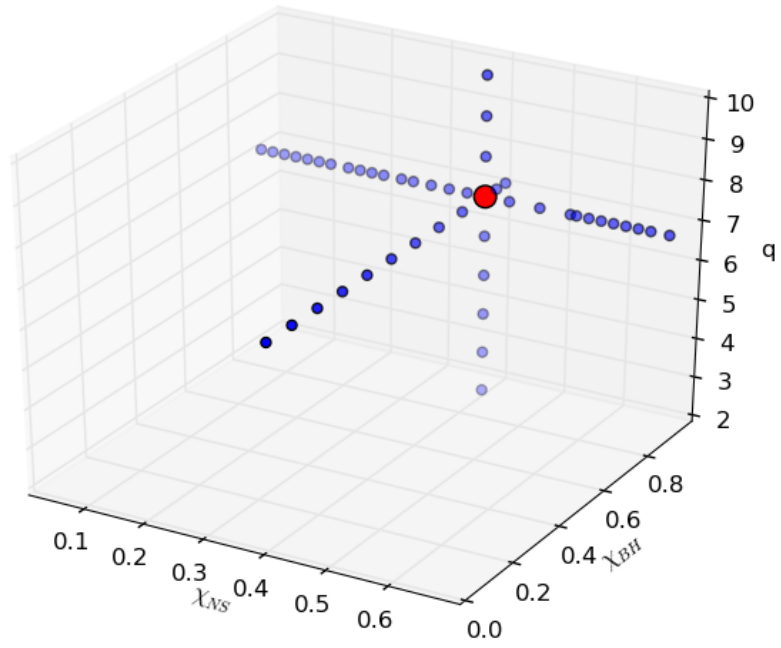


Figure 3.6: Parameter space exploration. Starting from R14i60 $\uparrow$  (large red circle) we vary (i) the Bh spin  $\chi_{\text{BH}}$ , (ii) the Ns spin  $\chi_{\text{NS}}$  and (iii) the black hole mass  $M_{\text{BH}}$ , indicated by the mass-ratio  $q$ .

Figure 3.6 summarizes all the initial data sets along the axes of  $\chi_{\text{NS}}$ ,  $\chi_{\text{BH}}$  and  $q$ .

We begin by varying the neutron star spin from  $\chi = 0$  ( $\omega = 0$ ) to  $\chi \sim 0.7$ , corresponding to  $\omega \sim 0.22$ . The parameters in this sequence are otherwise the same as in the R14i0 data sets, and the neutron star spin is kept aligned with the orbital angular momentum. To demonstrate convergence, we begin by plotting the Hamiltonian and momentum constraints for a subset of the generated initial data sets, with  $\chi \sim 0.1, 0.3, 0.5, 0.7$ . This is shown in Fig. 3.7. We note that in general we see exponential convergence, as expected, but there are a few features worth discussing in the data. As discussed earlier, the constraints at the second resolution are higher than expected because the spin is "turned on" at the second resolution. The size of this feature at is a monotonically increasing function of spin, as we might expect, as the solver has a more difficult time adjusting to a larger spin being abruptly turned on. We also note that at high resolution, in the  $\chi \sim 0.7$  curve, we lose exponential convergence and the curves flatten out around  $10^{-6}$ . **Plot  $\delta C$  for different  $\chi_{\text{NS}}$ .** This is likely a sign that the accuracy of the solver is becoming limited, likely by approximations that go into the solver.  $\chi \sim 0.7$  is around the maximum theoretical neutron star spin, so such difficulties are expected.

In Fig. 3.8 we plot the measured neutron star spin  $\chi_{\text{NS}}$  as a function of the code parameter  $\omega$  for the full sequence. As expected, we find a linear relationship at low  $\omega$ , but the relationship becomes non-linear at higher  $\omega$ , as the neutron star's size, and thus moment of inertia, becomes an appreciable function of spin. We find that the solver breaks down around  $\chi_{\text{NS}} \sim 0.7$  which is around the theoretical maximum spin for  $\Gamma = 2$  polytropes. In Fig. 3.8 we have also plotted, in addition to this Bh-Ns curve, a curve from Ns-Ns initial data sets. These data use different NS parameters, with mass  $M_{\text{ADM}} = 1.64M_{\odot}$  and equation of state parameter  $\kappa = 123.6$ . However, the curves remain very close to each other in shape. Thus we see the neutron star spin code seems to be working the same for the code described in this chapter, as well as the code described in Ch. 2.

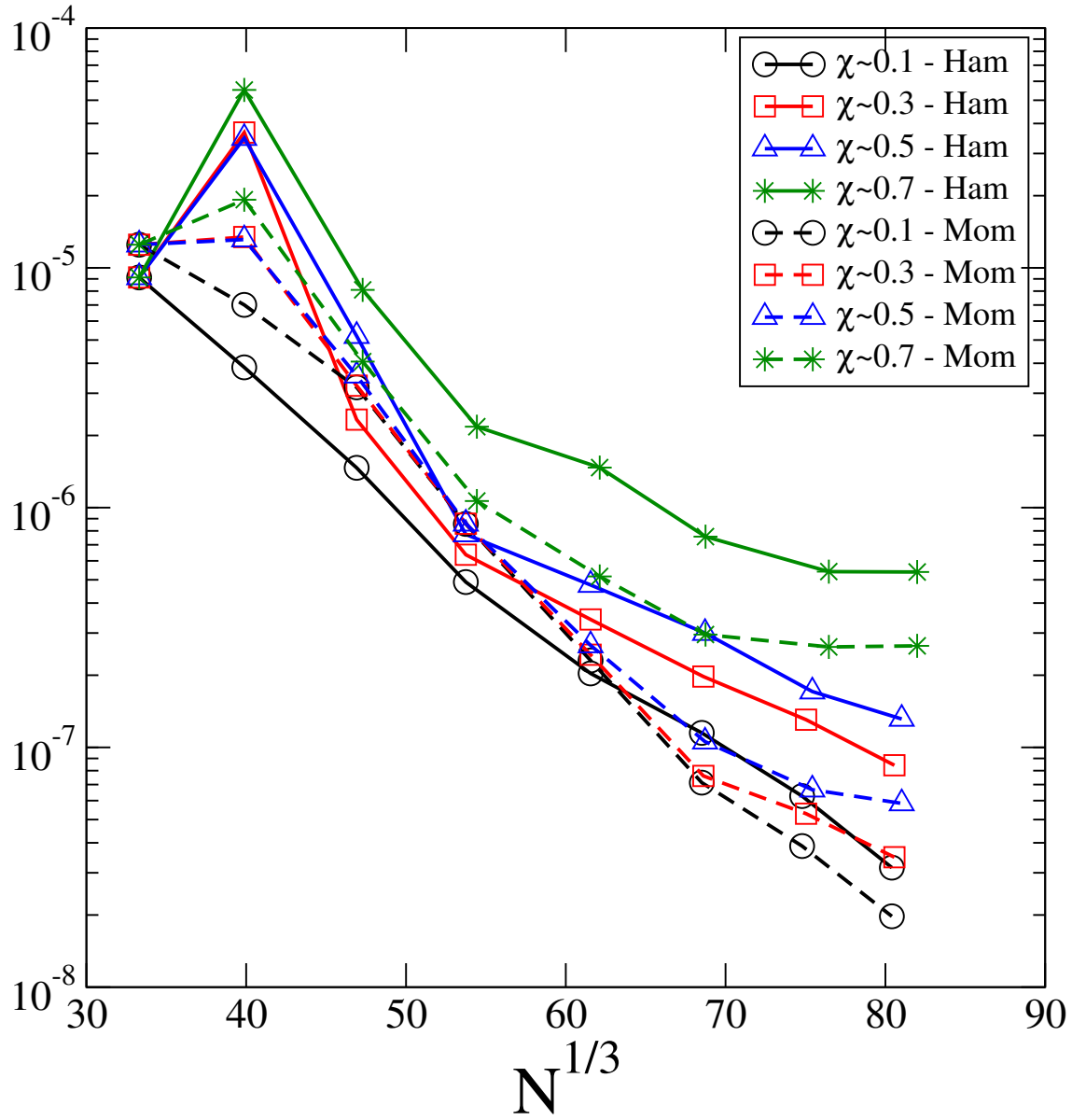


Figure 3.7: Hamiltonian (solid curves) and momentum (dotted curves) constraints for four different neutron star spins.

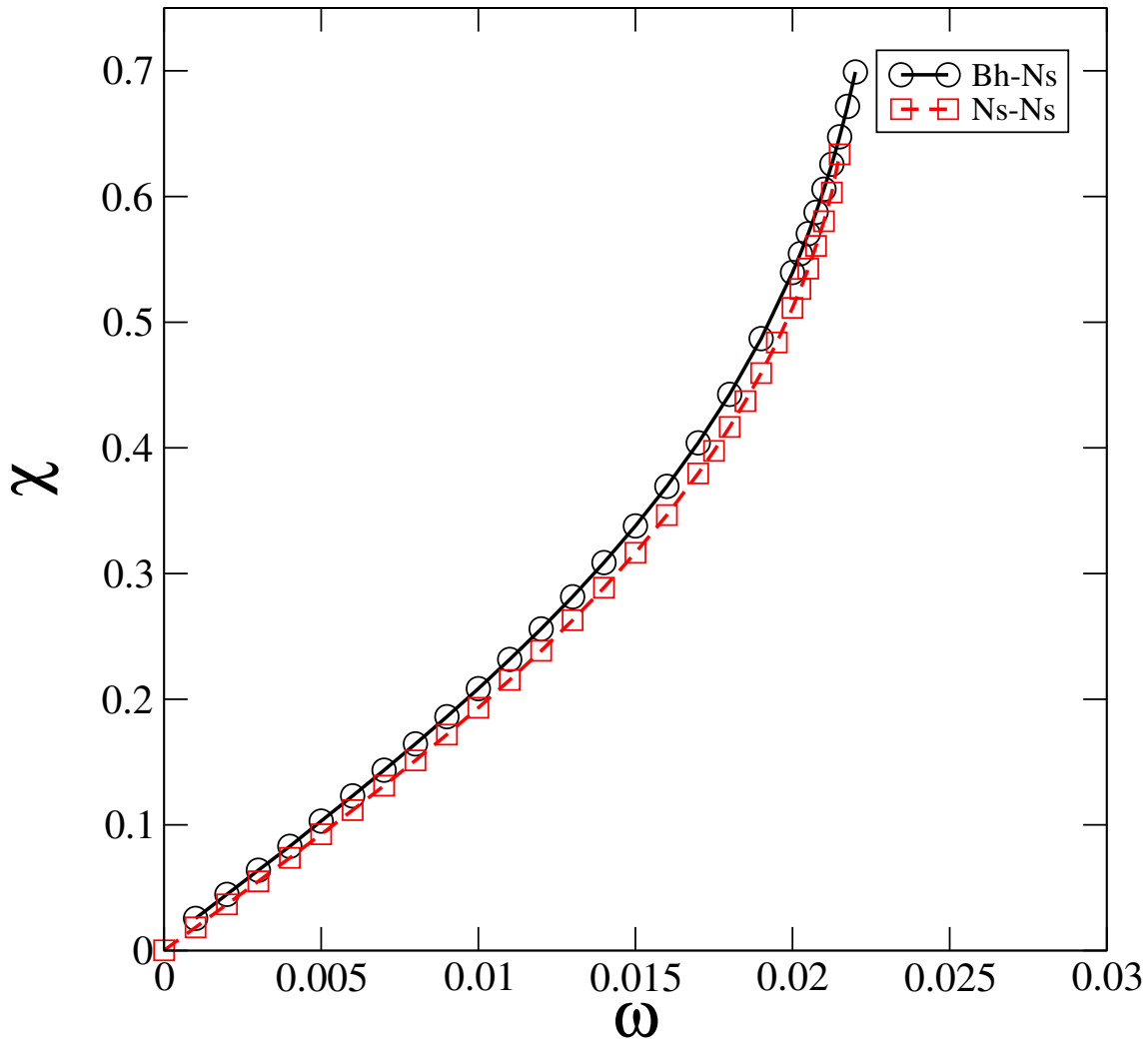


Figure 3.8: Neutron star spin  $\chi$  as a function of neutron star spin parameter  $\omega$  for a sequence of initial data sets. The black hole spin is constant at  $\chi = 0.9$  and the mass ratio is  $q = 7$ . The dashed red curve is from Ns-Ns binaries, with somewhat different neutron star parameters.

After the sequence in  $\chi_{\text{NS}}$ , we next look at a sequence in  $\chi_{\text{BH}}$ . In particular, we vary the black hole spin from  $\chi_{\text{BH}} = 0$  to  $\chi_{\text{BH}} = 0.99$ , keeping it aligned with the orbital angular momentum. The other binary parameters are kept the same as in the R14i0  $\uparrow$  initial data set; that is  $\chi_{\text{NS}} \sim 0.4$  and  $q = 7$ . In Figs. 3.9 we plot the Hamiltonian and momentum constraints, respectively, for this sequence. We find exponential convergence in all cases. It is interesting to note that the constraints seem to be lowest at the highest black hole spins,  $\chi_{\text{BH}} = 0.95$  and  $\chi_{\text{BH}} = 0.99$ , while one might expect these to be the most challenging cases.

Since in this work we are largely concerned with neutron star spin, it is interesting to consider how the measured neutron star spin,  $\chi_{\text{NS}}$  couples to other binary parameters. To lowest order, it should depend only on  $\omega_{\text{NS}}$ , but in practice it may also depend on the parameters of the black hole or of the orbit. For this sequence in  $\chi_{\text{BH}}$ , we plot  $\chi_{\text{NS}}$  as a function of  $\chi_{\text{BH}}$  in figure 3.10.  $\chi_{\text{NS}}$  is nearly constant, dropping by less than 1% between  $\chi_{\text{BH}} = 0$  and  $\chi_{\text{BH}} = 0.99$ .

Finally, we consider a sequence where we vary the mass ratio from  $q = 2$  to  $q = 10$ . In this sequence we keep the other binary parameters the same as in the R14i0  $\uparrow$  initial data set and we keep the orbital parameters  $M\Omega$  and  $D/M$  constant. As discussed above, we expect that this will induce a eccentricity of a few percent. To assess convergence, we plot the Hamiltonian and momentum constraints for this sequence in Fig. 3.11. We find exponential convergence in all cases. Interestingly, no clear pattern in  $q$ -space emerges.

As with the previous sequence, it is interesting to look at the properties of  $\chi_{\text{NS}}$  as a function of  $q$ . This is shown in Fig 3.12. Although there is not a great amount of variation, apart from  $q = 2$ , there is a clear trend of  $\chi_{\text{NS}}$  decreasing with  $q$ . Again, however, the effect is quite small and we do not seek to explain it.

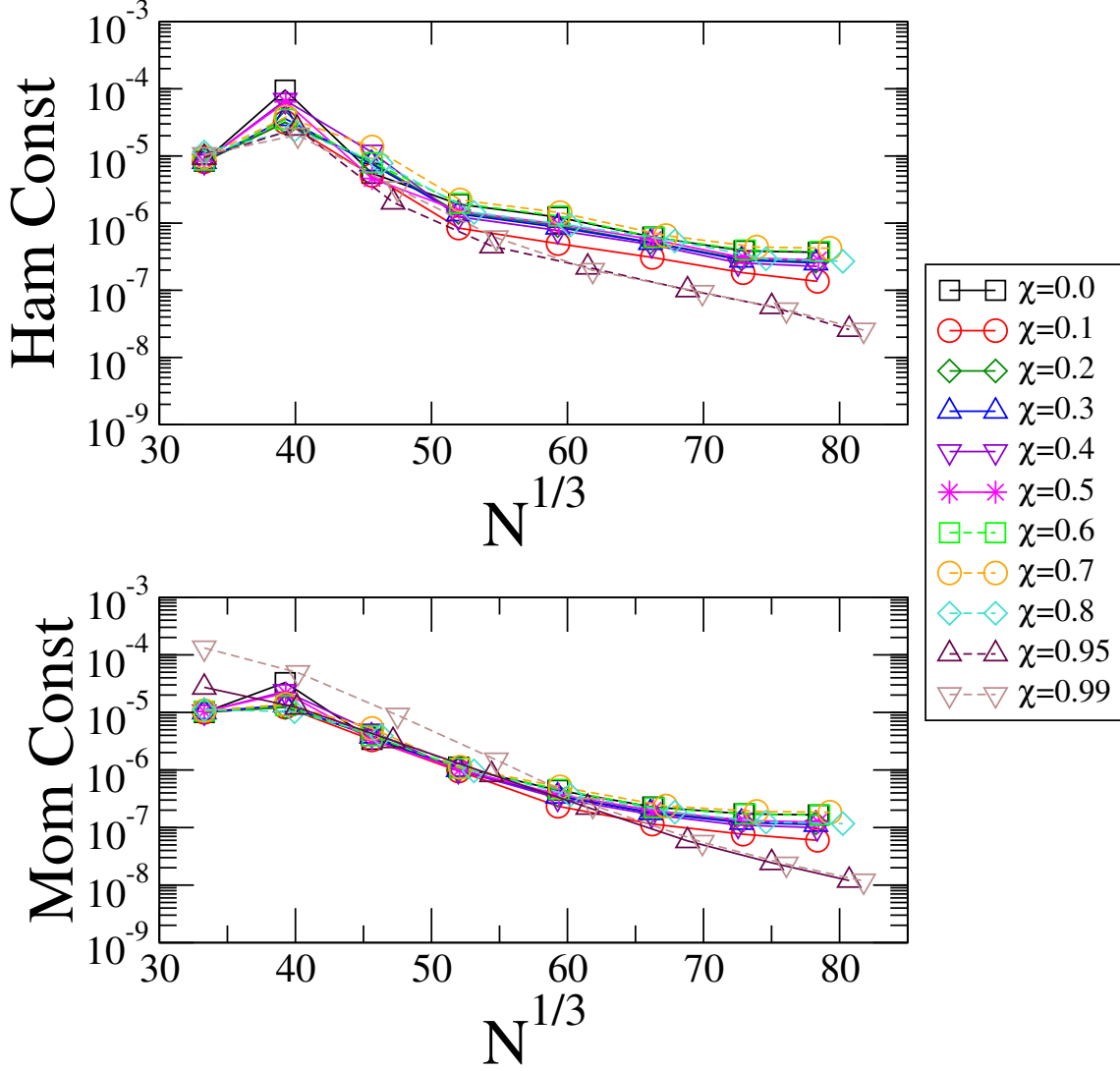


Figure 3.9: Hamiltonian (top panel) and momentum (bottom panel) constraints versus resolution for our sequence of binaries where the black-hole spin is varied from  $\chi_{\text{BH}} = 0$  to  $\chi_{\text{BH}} = 0.99$ . The neutron star spin is constant at  $\chi_{\text{NS}} \sim 0.4$  and the mass ratio is  $q = 7$ . We find exponential convergence in all cases.

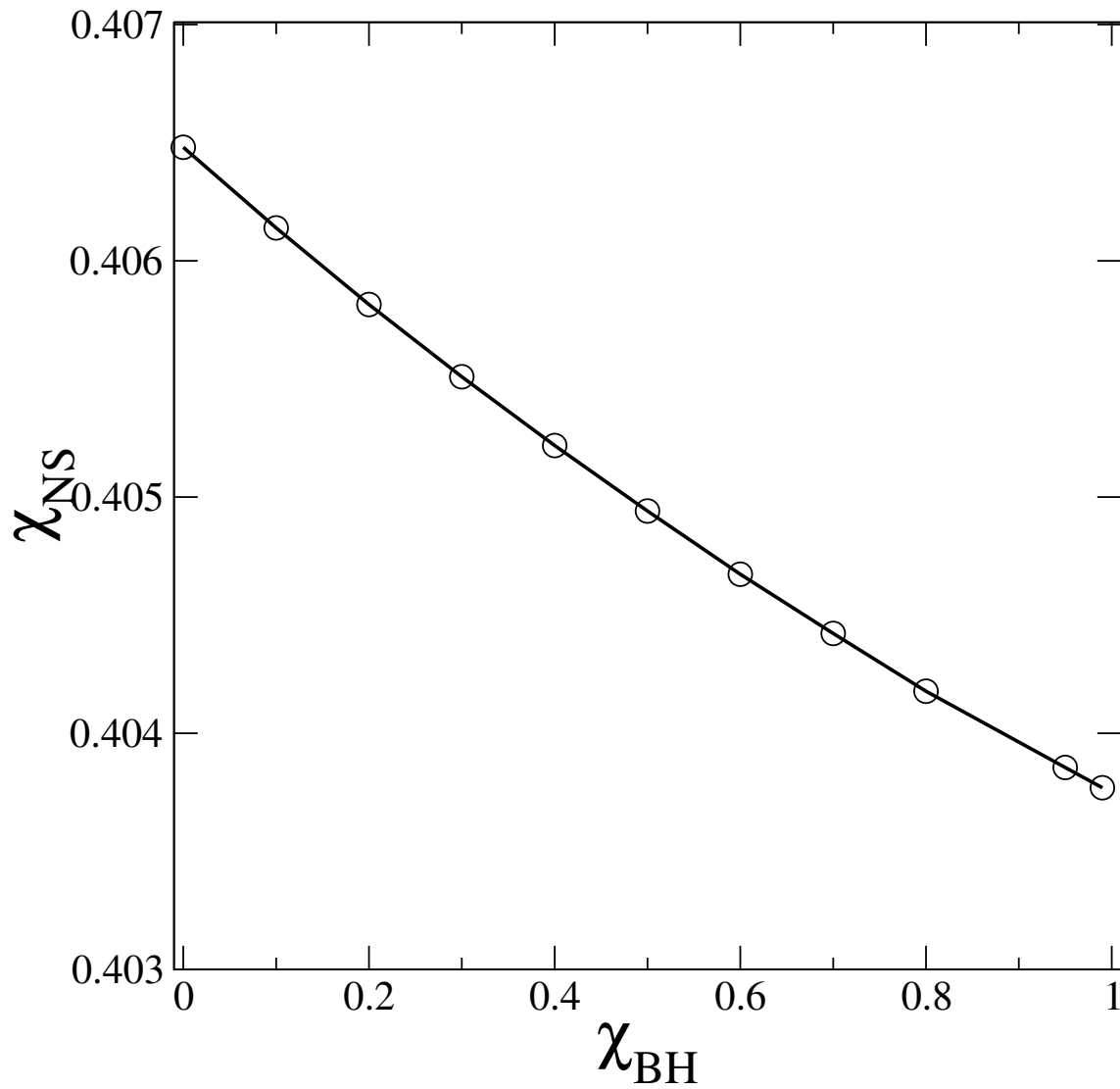


Figure 3.10: Neutron star spin  $\chi_{\text{NS}}$  as a function of black hole spin  $\chi_{\text{BH}}$  for this sequence. We notice a small downward linear trend.

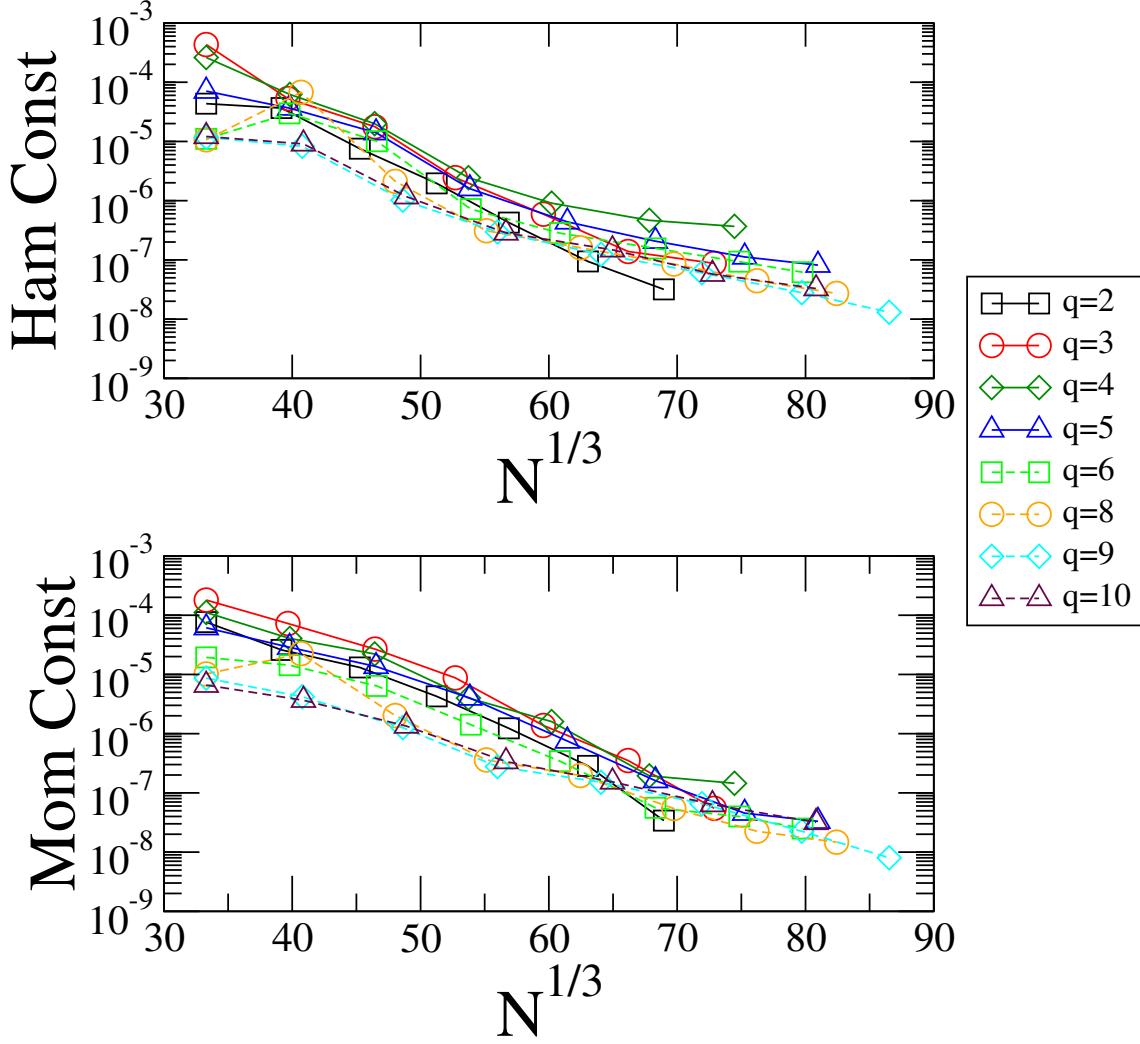


Figure 3.11: Hamiltonian (top panel) and momentum (bottom panel) constraints versus resolution for our sequence of binaries where the mass ratio is varied from  $q = 2$  up to  $q = 10$ . The neutron star spin is constant at  $\chi_{\text{NS}} \sim 0.4$  and the black hole spin is  $\chi_{\text{BH}} = 0.9$ . We find exponential convergence, as expected, in all cases.



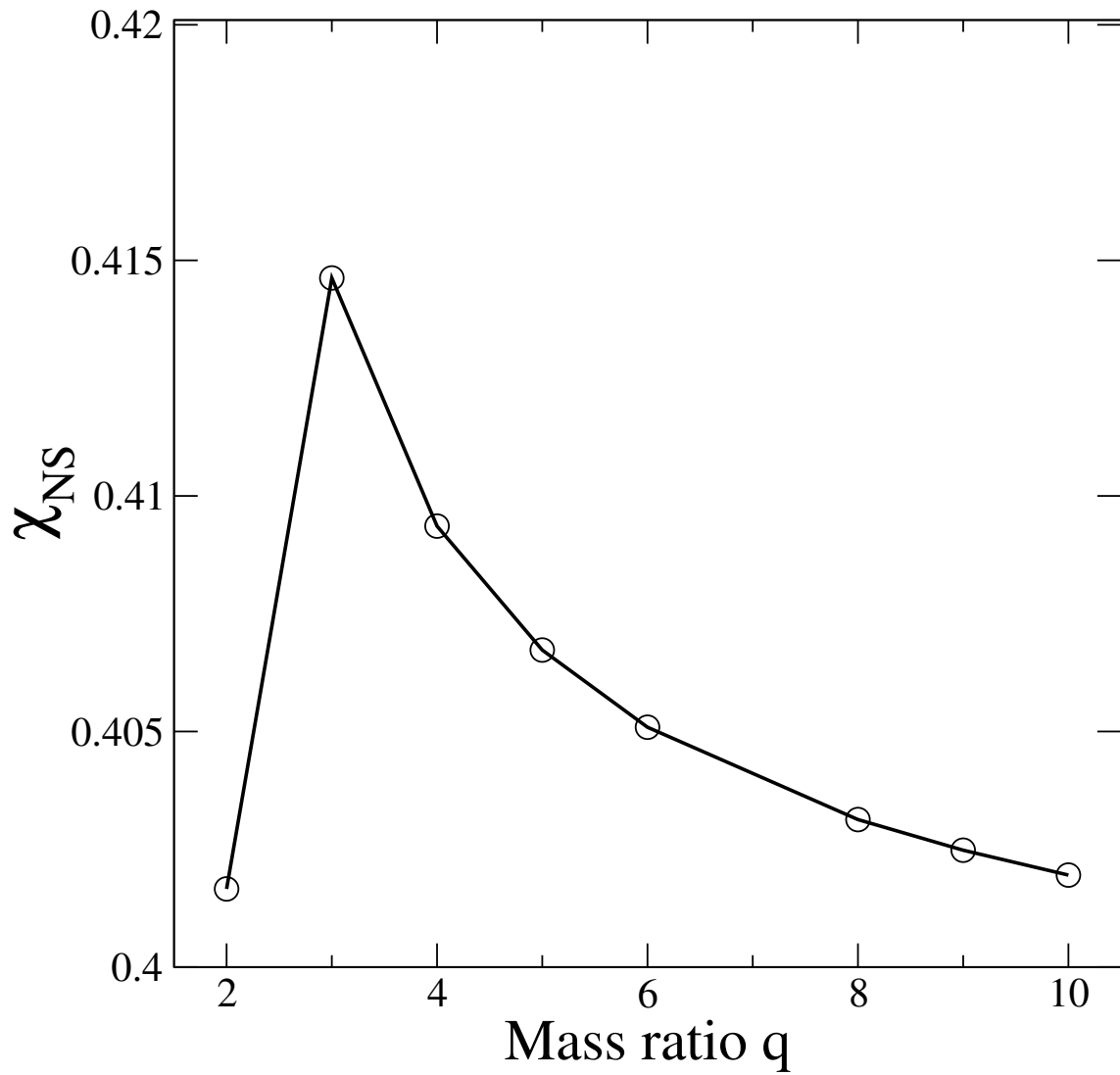


Figure 3.12: Neutron star spin  $\chi_{\text{NS}}$  as a function of mass ratio  $q$  for this sequence. We notice a small downward trend for  $q \geq 3$ .

### 3.5 Conclusion

We have presented code to create initial data for Bh-Ns binaries where the neutron stars have arbitrary spins. To our knowledge, this is the first time initial data has been created for Bh-Ns binaries with spinning neutron stars. We used the same formalism developed by Tichy (2011) and used in Tacik et al. (2015) to create initial data for Ns-Ns systems with arbitrary spins. Two new numerical tricks were found to be necessary to get convergent initial data - setting a maximum radius out to which to apply  $W^i = \epsilon^{ijk}\omega^j r^k$ , and only "turning on" the neutron star spin after the first resolution of the initial data solver has completed. We created convergent initial data sets across a large portion of the Bh-Ns binary parameter space. We created 36 initial data sets using the results of Foucart et al. (2013) as a starting point. These initial data sets spanned three different equations of state (all  $\Gamma = 2$  polytropes), two different neutron star spin magnitudes, three different neutron star spin orientations, and four different black hole spin orientations. We also created three sequences of initial data to help fill out the parameter space - a sequence in neutron star spin ranging from  $\chi_{\text{NS}} = 0$  to  $\chi_{\text{NS}} \sim 0.7$  (near the maximum theoretical spin for neutron stars), a sequence in black hole spin ranging from  $\chi_{\text{BH}} = 0$  to  $\chi_{\text{BH}} = 0.99$  and a sequence in mass ratio ranging from  $q = 2$  to  $q = 10$ .

Future research will involve running evolutions of these, or similar, initial data sets. Some of the 36 initial data sets could be used to investigate how neutron star spin affects tidal disruption of the star by the black hole, and how it affects the disk that is formed. The phase evolution can also be examined and compared to Post-Newtonian or other analytic predictions such as Effective-One-Body (EOB). In long and accurate simulations, the coupling of the neutron star spin to the dynamic tides (Hinderer et al. (2016)) could become important in this kind of comparison. Another interesting route to explore could be to see how large of a disk can be produced in Bh-Ns simulations. Lovelace et al. (2013) create a very large disk with a black hole spin of  $\chi = 0.97$  and mass ratio  $q = 3$  - a highly spinning neutron star with less strongly bound material may

be able to increase this disk mass even further.

# Chapter 4

## Junk Radiation in Binary Black Hole Simulations

### 4.1 Chapter Overview

An Overview of my chapter here.

### 4.2 Chapter TDL

- Many citations in the introduction and very much out of date. It should be re-written.
- Are there any new papers on junk radiation to discuss that have come out since this time? Ask Harald / do a literature search.
- Discuss more about boundary conditions in IVP for bbh
- Maybe make a table detailing all the simulations that were done. Come up with a better naming system for the runs.
- There is a note about the uncertainty from numerical truncation in  $E_J$  for SKS. Not sure what to do about that. I think it can reasonably left the way it is.

- Combine data into a single plot for wave extraction plot
- Decide what to do for  $\delta M$  for SKS, given that the data is so weird
- Write the results section closely citing all the figures properly. Are we overfitting the data? Be careful with how to report the data. Maybe just focus on the plots, and not the fits.
- Write a conclusion. What are the implications of these kinds of numbers?

### 4.3 Introduction

The inspiral and merger of solar-mass binary black holes are one of the most promising sources for ground-based gravitational wave detectors such as LIGO Barish & Weiss (1999), Virgo Acernese et al. (2006), and LCGT Kuroda & the LCGT Collaboration (2010). In the next few years, as it is upgraded to higher sensitivity, Advanced LIGO is expected to begin making detections, with a realistic event rate estimated at about 20 per year Abadie et al. (2010b). For the gravitational radiation to be detected, and to learn about the properties of the source, waveform templates must be accurately modelled. Although analytic prescriptions like Post-Newtonian (PN) Blanchet (2006) or Effective One-Body (EOB) Buonanno & Damour (1999) can accurately model some of the inspiral, Numerical Relativity (NR) simulations are needed to accurately model late inspiral and merger of the black holes.

In current NR simulations, there is always a burst of spurious gravitational radiation at the start of the simulation, often referred to as “junk radiation”. This pulse always occurs at the start of the simulation, it is of much higher frequency and amplitude than the astrophysical gravitational radiation, and it has significant contributions from modes other than the standard  $(l, m) = (2, 2)$  spherical harmonic mode, which is the dominant contribution for the astrophysical part of the waveform. Therefore, this pulse is not astrophysical.

We illustrate this effect in Fig. 4.1, showing the gravitational waveform at the start of a typical simulation. The waves are extracted on a coordinate sphere at  $r = 160M$ <sup>1</sup>, so the waves start appearing at  $t \approx 160M$ . We see the burst of junk radiation last about  $100M$  in time, with significant contributions from both the  $(2, 2)$  and  $(2, 0)$  modes. The junk radiation then dies out, and subsequently, the expected sinusoidal  $(2, 2)$  mode emerges.

This junk radiation is undesirable in simulations for several reasons. It adds to the computational cost of the simulation as the junk radiation must leave the computational grid before any useful physical information can be extracted. It can unrealistically shorten the time until the black holes merge Bode et al. (2008). It also makes it more difficult to compare general relativistic simulations with Post-Newtonian calculations. It is therefore a useful endeavour to try to better understand the junk radiation, how important it is, and how to reduce it.

Junk radiation is thought to be caused by assumptions made during the initial data construction, which are not compatible with black holes in perfect equilibrium. Specifically, black holes are generally treated in the initial data as independent and non-interacting, while in reality there should be some non-trivial tidal interactions between them. If we imagine a sequence of initial data sets where the initial separation between the holes is decreasing, we would expect that this effect becomes more important as the initial separation decreases. Moreover, the black holes in the initial data are often constructed with techniques that do not even allow to construct a single, equilibrium black hole. Specifically, often, conformal flatness is assumed. As detailed in section 4.4.1, the construction of initial data has a free choice for the conformal metric,  $\tilde{g}_{ij}$ , on the initial hypersurface. A common choice is conformal flatness, i.e.,  $\tilde{g}_{ij}$  is equal to the flat Euclidean metric. Since every spherically symmetric space is conformally flat, this would be fine for one Schwarzschild black hole. However, a binary system of compact objects

---

<sup>1</sup>We use units where  $G = c = 1$ . The only natural length and time scale is then the total mass of both black holes,  $M$ .

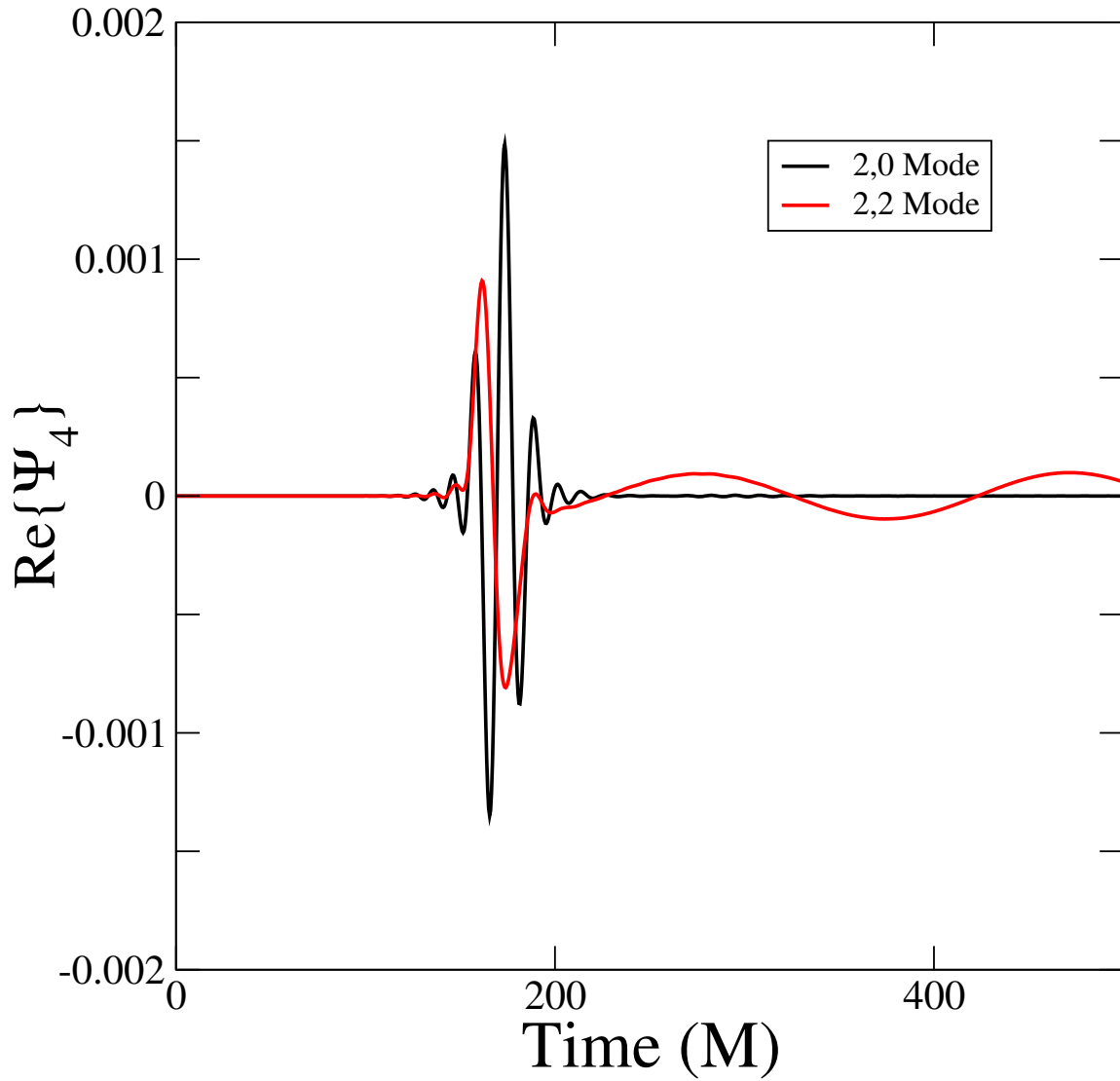


Figure 4.1: A typical run illustrating the spurious burst of junk radiation. We see at early times a burst of high-frequency, high-amplitude radiation. At later times, the  $(2,0)$  mode dies out, and the  $(2,2)$  mode settles into the usual inspiral-type radiation

is not conformally flat at second PN order Rieth (1997), and the Kerr space-time does not admit a conformally flat slicing Garat & Price (2000) that continuously approach Schwarzschild coordinates as the spin goes to zero. The former effect should decrease in importance with increasing separation of the binary. The latter is caused by a deficiency of conformally flat slicing that is present even for single spinning black holes, and so we expect its importance to be approximately independent of binary separation.

Lovelace Lovelace (2009) investigated the effects on junk radiation of using superposed Kerr-Schild Matzner et al. (1998); Marronetti & Matzner (2000); Pfeiffer et al. (2002); Lovelace et al. (2008) (conformally curved) initial data for equal mass, non-spinning black holes. The metric is written as

$$\tilde{g}_{ij} = f_{ij} + e^{-(r_A/w)^2} (g_{ij}^A - f_{ij}) + e^{-(r_B/w)^2} (g_{ij}^B - f_{ij}), \quad (4.1)$$

where  $f_{ij}$  is the Euclidean metric,  $r^{A,B}$  are the distances from black holes  $A$  and  $B$ , and  $g_{ij}^{A,B}$  is the Kerr-Schild metric boosted in the direction of the black hole's motion. This has the effect that the metric looks like Schwarzschild near the black holes, and looks flat far away. The Gaussian scalings were needed to help improve the convergence of the initial data. It was found that in general, the conformally curved initial data can decrease the amplitude of the junk radiation by a factor of  $\sim 2$ . Superposed Kerr-Schild initial data is built around the Kerr-Schild metric, which exactly represents single spinning black holes. Therefore, one would expect that the advantages of superposed Kerr-Schild become particularly apparent for spinning black holes.

In this paper we investigate the parameter space dependence of junk radiation. We measure its dependence on the spin and on the initial separation of the black holes, for low eccentricity, equal-mass, spin-aligned binaries. We also perform a comparison between conformally flat initial data, and superposed Kerr-Schild initial data.

The paper is organized as follows: Section 4.4 presents the numerical methods, and Section 4.5 describes how we quantify junk radiation and other initial transients in the



BBH initial data sets. We present our results in Sec. 4.6 and close with a discussion in Sec. 2.6.

## 4.4 Numerical Methods

### 4.4.1 The Initial Value Problem

Employing the usual 3+1 decomposition( Arnowitt et al. (1962); York, Jr. (1979)),space-time is foliated by a family of spacelike hypersurfaces  $\Sigma_t$ . Each hypersurface has a future-pointing unit normal  $n^\mu$ , induced metric  $g_{ij}$ , and extrinsic curvature  $K_{\mu\nu} = -\frac{1}{2}\mathcal{L}_n g_{\mu\nu}$ . The metric is written as

$$g_{\mu\nu} = -\alpha^2 dt^2 + g_{ij} (dx^i + \beta^i dt) (dx^j + \beta^j dt), \quad (4.2)$$

where  $\alpha$  and  $\beta$  are the lapse function and the shift vector respectively. The lapse measures the proper time between neighbouring hypersurfaces, and the shift vector determines how coordinate labels move between neighbouring hypersurfaces. On the initial hypersurface  $\Sigma_0$ , spatial metric and extrinsic curvature must satisfy the vacuum constraint equations

$$R + K^2 - K_{ij}K^{ij} = 0, \quad (4.3)$$

$$\nabla_j (K^{ij} - g^{ij}K) = 0. \quad (4.4)$$

To solve the constraint equations one writes( Lichnerowicz (1944)) the metric in terms of a conformal metric  $\tilde{g}_{ij}$  and a conformal factor  $\Psi$ :

$$g_{ij} = \Psi^4 \tilde{g}_{ij}. \quad (4.5)$$

We also split the extrinsic curvature into trace and trace-free parts

$$K^{ij} = A^{ij} + \frac{1}{3}g^{ij}K, \quad (4.6)$$

and employ the extended conformal thin sandwich formalism York (1999); Pfeiffer & York (2003) to further decompose  $A^{ij}$ . One must then choose  $(\tilde{g}_{ij}, \partial_t \tilde{g}_{ij}, K, \partial_t K)$  as the

free data. Compared to the extrinsic curvature decomposition Murchadha & York, Jr. (1974), the conformal thin sandwich formalism allows for physically motivated choices to a larger number of the free data. Elliptic equations with appropriate boundary conditions are then solved for  $\Psi$ ,  $\alpha\Psi$ , and  $\beta^i$ , and the physical data is re-assembled.  $\partial_t \tilde{g}_{ij} = \partial_t K = 0$  is chosen so that system is initially stationary in the co-rotating frame. This then leaves  $\tilde{g}_{ij}$  and  $K$  as the free data to choose.

The two types of initial data we compare are described in detail in Ref. Lovelace et al. (2008): Conformally flat, quasi-equilibrium initial data employs conformal flatness, maximal slicing ( $K = 0$ ) and inner boundary conditions that enforce that the black holes are instantaneously in equilibrium Caudill et al. (2006); Cook & Pfeiffer (2004); Cook (2002). Superposed Kerr-Schild initial data, first used in Marronetti & Matzner (2000); Matzner et al. (1998), takes the spatial metric and extrinsic curvature as superposition of elements of Kerr-Schild metrics (one for each black hole). As explained in Ref. Lovelace et al. (2008), we introduce Gaussian attenuation functions to ensure regularity at spatial infinity. Inner boundary conditions are **PROVIDE DETAILS**.

#### 4.4.2 Code

The initial data is solved using the spectral solver **Spells**( Pfeiffer et al. (2003)) of the Spectral Einstein Code **SpEC** SXS (????). This is a multi-domain elliptic PDE solver that uses pseudo-spectral methods, whereby quantities of interest are expressed as a linear summation of basis functions. This method gives exponential convergence (with the number of basis functions) as long as the quantities of interest are smooth. The black hole singularities are dealt with by excision from the computational grid. We use the dual frame method described in Scheel et al. (2006). The domain decomposition and position of the black holes are fixed in a comoving frame, but the equations of motion are solved in an inertial frame that is asymptotically Minkowski. The frames are related by a rotation term (due to orbital motion) and a contraction term (due to inspiral motion).

Gravitational waves are extracted on outer spherical shells of the domain using the Newman-Penrose scalar  $\Psi_4$ . Given a spacelike hypersurface with unit normal  $n^\mu$  and a spatial unit vector in the direction of wave propagation  $r^\mu$ ,  $\Psi_4$  is defined as

$$\Psi_4 = -C_{\alpha\mu\beta\nu} l^\mu l^\nu m^\alpha \bar{m}^\beta \quad (4.7)$$

where  $C_{\alpha\mu\beta\nu}$  is the Weyl tensor,  $l^\mu = (n^\mu - r^\mu)/\sqrt{2}$  and  $m^\mu$  is a complex null vector satisfying  $m^\mu \bar{m}_\mu = 1$ . We then expand  $\Psi_4$  in spin-weighted spherical harmonics

$$\Psi_4(t, r, \theta, \phi) = \sum_{l,m} \Psi_4^{lm}(t, r) {}_{-2}Y_{lm}(\theta, \phi) \quad (4.8)$$

The number of terms used in this expansion is generally  $l \leq 8$  in our simulations. At large  $r$ ,  $\Psi_4$  is related to the gravitational wave amplitude,  $h$ , by

$$\Psi_4 = \frac{d^2}{dt^2} h_+ - i \frac{d^2}{dt^2} h_\times. \quad (4.9)$$

### 4.4.3 Eccentricity Reduction

Gravitational radiation tends to circularize in-spiralling compact binaries (Peters & Mathews (1963); Peters (1964)). We reduce orbital eccentricity with an iterative method similar to the one described in Boyle et al. (2007); Chu et al. (2009). One guesses the initial orbital frequency  $\Omega_0$  from Kepler's third law or from a Post-Newtonian calculation, while assuming that the initial radial velocity,  $v_r$  is zero. After the first simulation has run for a sufficient length, about two orbits, we fit the time derivative of the orbital frequency,  $\dot{\Omega}(t)$  as suggested in Buonanno et al. (2011). We fit parameters  $\{A_0, A_1, T_c, B, \phi, \omega, q\}$  with the function

$$\dot{\Omega}(t) = A_0 (T_c - t)^{-11/8} + A_1 (T_c - t)^{-13/8} + B \cos(\varphi + \omega t + q t^2), \quad (4.10)$$

where  $T_C$  is the time of merger. The first two terms represent the smooth inspiral motion of the black holes, while the oscillatory second terms represents unwanted effects due to eccentricity. The updating formulae

$$\delta\Omega_0 = -\frac{B\omega \sin \varphi}{4\Omega_0^2} \quad (4.11)$$

$$\delta v_r = \frac{B d_0 \cos \varphi}{2\Omega_0}, \quad (4.12)$$

where  $d_0$  is the binary separation, are designed to circularize low eccentricity Newtonian binaries. This process is continued iteratively, typically another one or two times, until the eccentricity is reduced to  $e \lesssim 0.002$ . The effect of eccentricity on junk radiation is discussed in section 4.5.2.

#### 4.4.4 Simulations

We run BBH evolutions using both conformally flat and SKS initial data. We consider five different initial separations for CF data,  $D/M = \{12, 15, 20, 25, 30\}$ , and  $D/M = \{12, 15, 20\}$  for SKS data, where  $M$  is the total mass of both black holes, and at each separation we consider six different spins,  $\chi = \{0, 0.1, 0.2, 0.3, 0.4, 0.5\}$ . In each case the black holes are of equal mass, equal spin, and the spin is aligned with the orbital angular momentum, i.e., in the the  $+z$  direction. To test the convergence of quantities of interest, each run is done at four resolutions, which we will refer to as N0 (lowest resolution) to N3 (highest resolution). Each evolution is run to about  $t \sim 1000M$ , which is long enough to accurately measure the eccentricity, and make sure that it is sufficiently low. As discussed in section 4.5.2, sufficiently low means  $e \lesssim 0.002$ .

### 4.5 Methodology

We employ three diagnostics to measure the initial relaxation of the initial data: the outgoing pulse of radiation (junk radiation), the change in black hole mass during relaxation, and the change in black hole spin during relaxation.

### 4.5.1 Pulse in the Gravitational Waveform

In this section we discuss our methods of quantifying the amount of junk radiation present in a given simulation. It is not immediately obvious what the best way to do this is. Lovelace (2009) considered the maximum value of the Newman-Penrose waveform,  $\max\{R|\Psi_4^{lm}|\}$ , where  $R$  is the extraction radius. The  $(l, m) = (2, 2)$  and  $(2, 0)$  modes were found to dominate. We find, however, that this method has some inadequacies. This is illustrated by comparing  $R|\Psi_4^{lm}|(t_R)$ , where  $t_R$  is the retarded time,  $t_R = t - R$ , for two runs (CF data,  $D = 15M$ ,  $\chi = 0.2$ ); one at our typical highest resolution N3, and another at an even higher resolution, N7. In terms of the total number of basis functions  $X$ ,  $X^{1/3} \sim 58$  for N3 and  $X^{1/3} \sim 78$  for N4. The  $(2, 0)$  and  $(2, 2)$  modes are shown in the top panel of Fig. 4.2. It is clear that the  $(2, 0)$  mode is significantly different between N3 and N7, in both the largest peak and in the subsequent smaller peaks, and that these differences are not well encapsulated simply by  $\max\{R|\Psi_4|\}$ . In Fig. 4.2 we also show these quantities for an SKS run with the same parameters. Because the waveform is significantly different from the CF waveform in both the number of peaks and their relative heights, it is clear that  $\max\{R|\Psi_4^{lm}|\}$  does not encapsulate this waveform very well.

As a more robust quantity that incorporates the whole waveform, and is less resolution dependent than  $\max|R\Psi_4^{lm}|$ , we look at the total energy carried away from the system by gravitational waves. The gravitational wave energy flux is (Boyle et al. (2008))

$$F(t) = \frac{1}{16\pi} \sum_{l,m} \dot{h}_{lm}^2(t), \quad (4.13)$$

where

$$\dot{h}_{lm}(t) = \int_{t_0}^t \Psi_4^{lm}(t') dt' + H_{lm}. \quad (4.14)$$

The  $H_{lm}$  are integration constants. To measure the initial pulse of radiation, we use  $t_0 = 0$  and  $H_{lm} = 0$ . The energy flux,  $F(t)$ , is shown in the red curves in Fig. 4.3 for conformally flat initial data (top panel) and SKS initial data (bottom panel). The

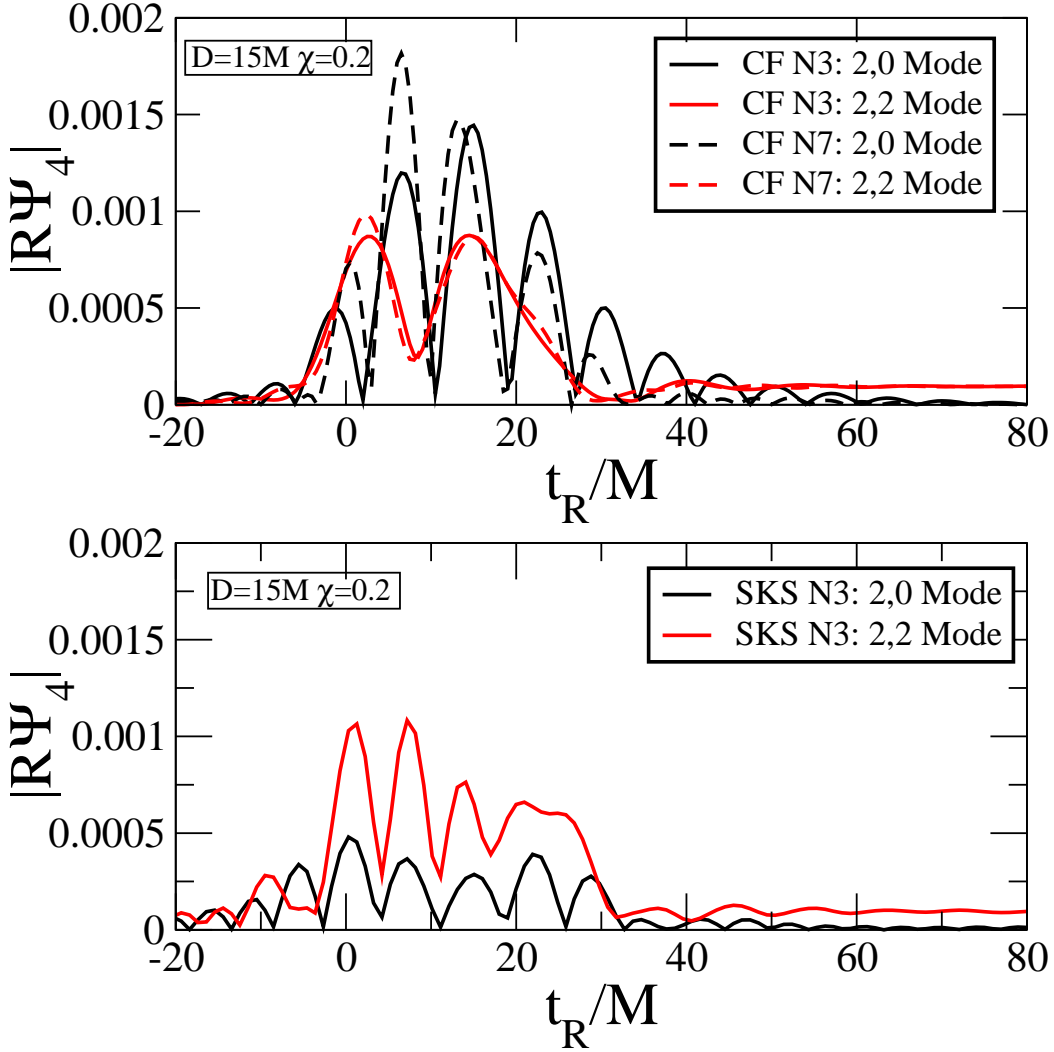


Figure 4.2: *Top Panel:* Comparison of the junk radiation profiles for our usual highest resolution (N3) and an additional run at very highest resolution (N7). We see, especially for the (2,0) mode, that the maximum peak of the junk radiation is much higher for N7, but additional peaks are comparable or higher for N3.

*Bottom Panel:* Junk radiation profile for an SKS run with the same parameters as in the top panel. The waveform is significantly different in structure from the CF waveform.

initial burst is apparent in these figures; at late times  $t_R \gtrsim 40M$ ,  $F(t)$  approaches the nearly constant energy flux of the astrophysical inspiral. We are now faced with two problems: We would like to isolate the energy carried in junk-radiation from the energy-flux astrophysical inspiral. And, we would like to do so in a robust way, independent of arbitrary choices. We proceed as follows:

First, we assume that the astrophysical energy flux begins at a time  $t_{22}$ , i.e.

$$F_{22}(t) = F_0 \theta(t - t_{22}). \quad (4.15)$$

Here,  $F_0$  represents the value of  $F(t)$  after the pulse of junk-radiation and  $\theta$  represents the step-function. The choice of a constant value  $F_0$  is reasonable since the timescale on which  $F_{22}$  changes significantly is much longer than the junk radiation timescale. This energy flux is indicated by the blue dashed curves in Fig. 4.3. We will discuss our choice for  $t_{22}$  shortly. The energy in the junk-radiation is given by

$$E_J = \int_0^{t_C} [(F(t) - F_{22}(t))] dt, \quad (4.16)$$

where the cut-off time  $t_C$  is chosen after the junk radiation has decayed, i.e.  $t_C - R \gtrsim 50M$ . The energy attributed to the junk radiation is thus the shaded area in Fig. 4.3. As already apparent from Fig. 4.3, the precise value of  $t_C$  is not extremely important, because at late times  $F(t) - F_{22}(t) \approx 0$ .

It remains to choose a prescription for the choice of  $t_{22}$ , the time when we deem the astrophysical waveform to “turn on”. A simple method would be to choose  $t_{22}$  to correspond to  $\max\{F(t)\}$ . This seems reasonable for the conformally flat curve in Fig. 4.3, but the more wide double-peaked structure of the SKS curve shows that another approach is needed. Instead we take  $t_{22}$  to correspond to the flux weighted centre of the junk radiation waveform. The first moment of  $F(t) - F_{22}(t)$ , in other words. So,

$$t_{22} = \frac{\int_0^{t_C} t (F(t) - F_0 \theta(t - t_{22})) dt}{\int_0^{t_C} (F(t) - F_0 \theta(t - t_{22})) dt}. \quad (4.17)$$

This equation must be solved iteratively for  $t_{22}$ .

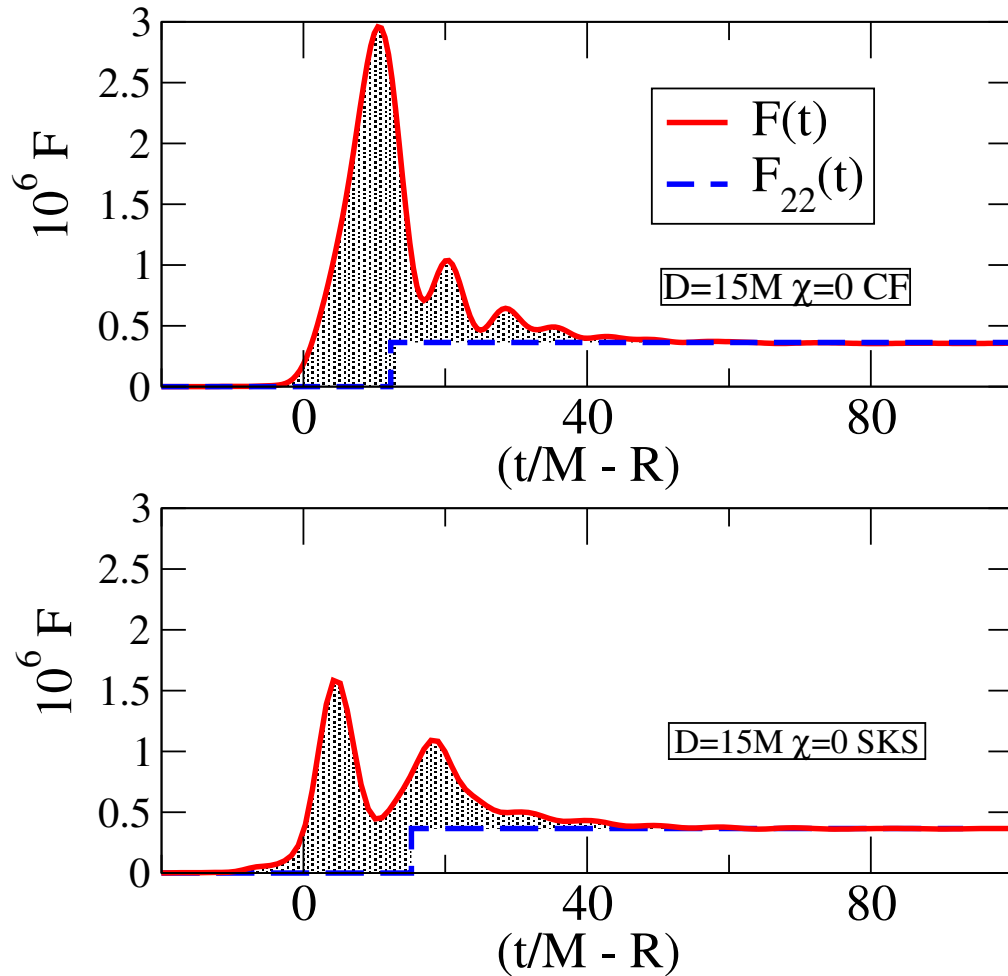


Figure 4.3: The flux  $F(t)$  is plotted for two different runs, both with parameters  $D = 15M$  and  $\chi = 0$ . Conformally flat initial data is in the top panel and SKS initial data is in the bottom panel. The solid red curve represents the total flux,  $F(t)$ . The dashed blue curve represents  $F_{22}(t)$ , the astrophysical flux that we subtract from  $F(t)$ . The shaded area between the two curves is the energy in junk radiation,  $E_J$ .



### 4.5.2 Uncertainty in $E_J$

Several effects may influence the quantity  $E_J$  computed by Eqs. (4.16) and (4.17). *Numerical truncation error* can be estimated by performing the simulations with different numerical resolution. Our simulations show that in general,  $E_J$  increases with resolution. This is because junk radiation is a short wavelength feature, so greater resolution allows for more of the features present to be captured. To estimate the uncertainty in  $E_J$ , we compare our  $D = 15M$ ,  $\chi = 0.2$  runs at N3 and N7, as discussed earlier. We find that at N7,  $E_J$  is about 13% greater than at N3. Since we don't have such high resolutions runs available for each of our cases, we assume that we can use this same 13% difference for each of our runs. This also assumes that at N7 the junk radiation is nearly fully resolved, so that this difference is a good indication of the true value. Finally, we use this same uncertainty of 13% for the SKS runs as well - while the technology is different for the SKS runs, it should still be a reasonably good estimate, and likely a conservative estimate, of the numerical truncation error in them.

A second uncertainty arises through the *choice of  $t_C$* . This number is chosen manually for each run, introducing a subjective element into the analysis. Examining the flux curves in Fig. 4.3, for example,  $t_C$  could conceivably be chosen differently by  $\sim 10M$  and still be a reasonable choice. Our definition Eq. (4.16) was meant to be robust to small changes in  $t_C$ . For  $E_J$  to be a robust measurement, it should therefore not change significantly in response to changes  $\delta t_C$  that are of that order. Indeed, this is enforced by our definition of  $E_J$ , which subtracts out the additional flux in the astrophysical (2,2) mode. To verify this assertion, we compute  $E_J$  with  $t_C$  in Eq. (4.16) replaced by  $t_C + \delta t_C$ . Figure 4.4 shows that indeed  $E_J$  is almost independent of  $\delta t_C$ . In Fig. 4.4,  $E_J$  is plotted against  $t_C$  in the representative  $D = 15M$ ,  $\chi = 0$  case. For each run we define a fractional error parameter due to the choice of  $t_C$ , where we average the differences for  $\delta t_C = -10M$  and  $\delta t_C = 10M$ :

$$\frac{\Delta E}{E} = \frac{|E(t_C + 10M) - E(t_C)| + |E(t_C) - E(t_C - 10M)|}{2E(t_C)} \quad (4.18)$$

This uncertainty ranges from  $\sim 0.25\%$  to  $\sim 3.75\%$  throughout all of our runs.

A third error in  $E_J$  arises through *the finite radius of gravitational wave extraction*. In this study, gravitational waves are extracted at radii  $R_{\text{ex}} \sim 300 - 400M$ . Gravitational waves extracted at finite radii are subject to near-field effects which may cause the extracted waveforms to differ from the one that would be observed at infinity. To estimate the error in  $E_J$  due to the finite extraction radius, we use the following procedure. For each of our runs, we take  $E_J$  at several extraction radii, and examine  $E_J$  as a function of  $1/R_{\text{ex}}$ . We then extrapolate

$$E_\infty = \lim_{1/R_{\text{ex}} \rightarrow 0} E_J(1/R_{\text{ex}}) \quad (4.19)$$

using a linear fit in  $1/R_{\text{ex}}$  to estimate the behaviour of  $E_J$  at infinity. We then take the fractional difference

$$\frac{\Delta E}{E} = \frac{E_\infty - E_J}{E_J} \quad (4.20)$$

as our error estimate. This parameter is on the order of 10% for most of our runs. Note, however, that we still use  $E_J$  and not  $E_\infty$  as our measure of energy in the pulse. In Fig. 4.5 we illustrate an example of this procedure, plotting  $E_J$  vs.  $1/R_{\text{ex}}$  for one case,  $D = 15M, \chi = 0$ , for both CF and SKS data.

A final factor that could influence the estimated  $E_J$  is the *eccentricity of the orbit of the black holes*. Previously we argued that it is important for astrophysically realistic binaries to have low eccentricity. We now consider how it affects the junk radiation, specifically the effect on  $E_J$ . We examine the case  $D = 25M, \chi = 0.1$  for CF data, as this particular case led to a fairly large range of eccentricities in the reduction process;  $e \sim \{0.03, 0.008, 0.0006\}$ . The measured  $E_J$  for these three cases is  $10^6 E_J = \{7.053 \pm 0.38\%, 7.204 \pm 0.53\%, 7.174 \pm 0.58\%\}$ . Here, the quoted uncertainty is purely due to the choice of  $t_C$ . The differences between the first two eccentricities is 2.10% and it is 0.42% for the last two. Because the latter difference is less than the uncertainty due to the choice of  $t_C$ , the two runs are effectively indistinguishable, and we conclude that we can

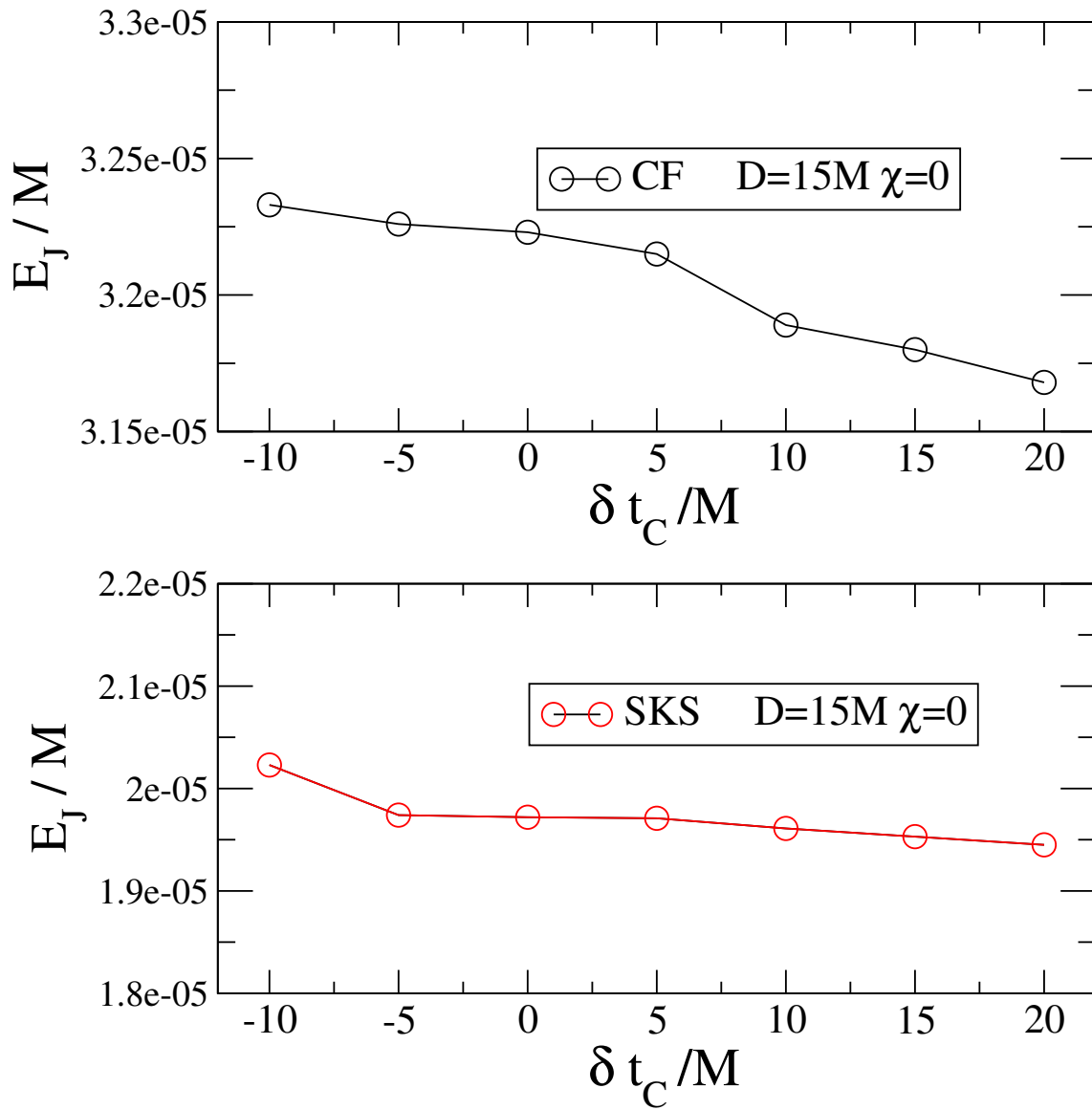


Figure 4.4:  $E_J$  is plotted against  $\delta t_C$ , representing changes to the selected value of  $t_C$  for runs where  $D = 15M$ ,  $\chi = 0$ . The results for conformally flat initial data are shown in the top panel, and SKS initial data in the bottom panel. Typical changes in  $E_J$  are on the order of a few percent.

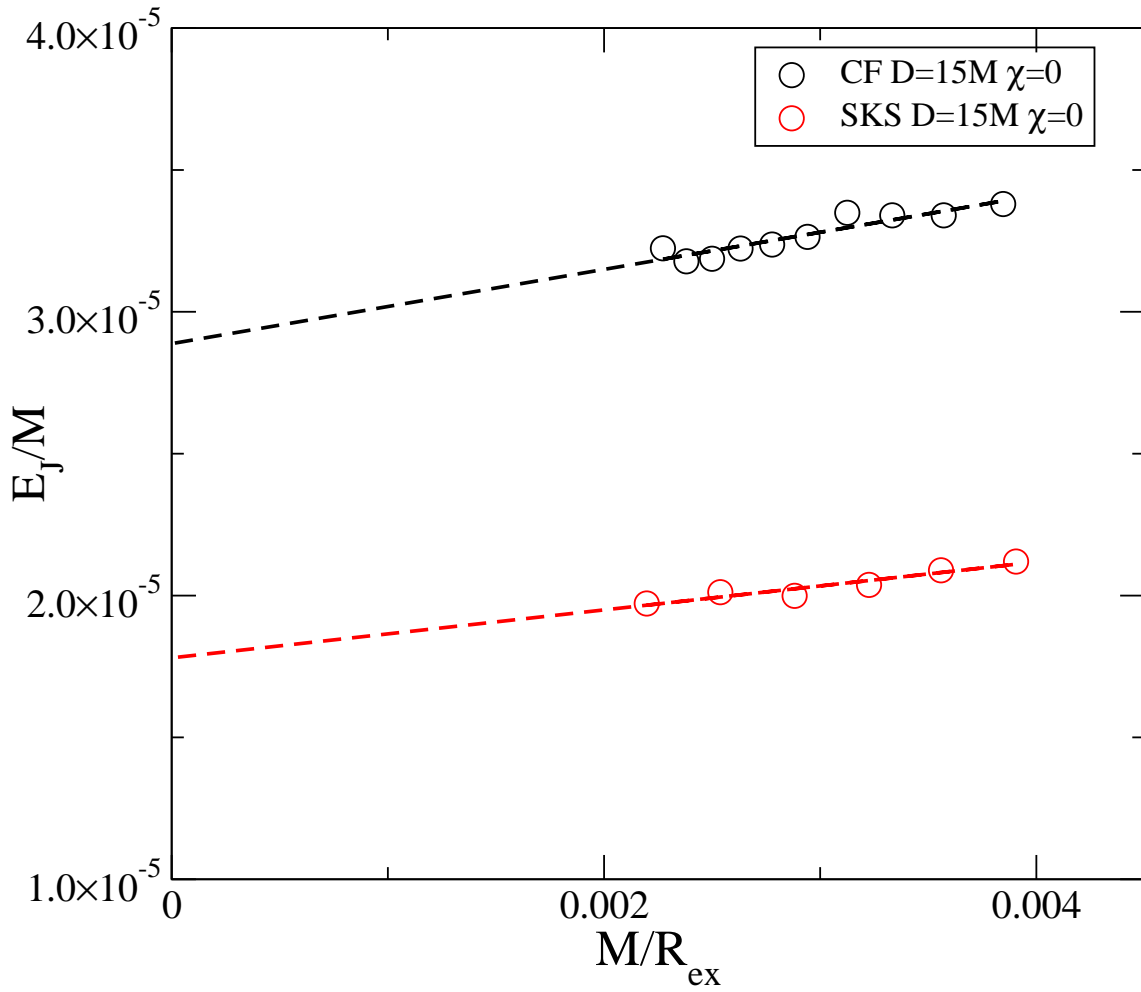


Figure 4.5:  $E_J$  as a function of  $1/R_{ex}$ , where  $R_{ex}$  is the extraction radius. This is for the case where  $D = 15M$ ,  $\chi = 0$ , with CF initial data in the left panel and SKS initial data in the right panel. The extrapolation to  $1/R_{ex} \rightarrow 0$  allows us to estimate the error on  $E_J$  due to finite extraction radius effects.

safely ignore the effects of residual eccentricity once we have  $e \lesssim 0.008$ . However, to be “safe”, we have generally reduced the eccentricity of all of our runs to  $e \lesssim 0.002$ .

### 4.5.3 Transient behaviour in Black Hole quantities

#### Mass Increase

Besides the energy carried away in junk radiation, we utilize two further diagnostics of transients arising from imperfect initial data. The first diagnostic is the irreducible mass of the black hole,  $M_{irr} = \sqrt{A/(16\pi)}$ , where  $A$  is the area of the black hole’s apparent horizon. In the first few  $M$  during the evolution, the apparent horizon mass  $M_{irr}(t)$  increases by a small amount, before settling down to an approximately constant value. This effect is easily apparent for CF initial data plotted in the upper panel of Fig. 4.6. We characterize the increase in mass due to initial transients by

$$\delta M(t) = \frac{M_{irr}(t)}{M_{irr}(0)} - 1 \quad (4.21)$$

and the equilibrium parameter  $\delta M_{eq} = \delta M(t_{eq})$ . Here  $t_{eq}$  is a time where the mass-increase is complete, and levels off; typically  $\sim 20M$ .

For SKS initial data the behaviour of  $M_{irr}(t)$  is more complex. Within the first few  $M$ ,  $M_{irr}(t)$  shows a rapid, albeit small increase, presumably due to relaxation of the geometry in the immediate vicinity of the black holes. The trend here is similar to the CF initial data, in that larger spins result in a larger increase of  $M_{irr}(t)$ , albeit the magnitude of the increase is about a factor 50 smaller for SKS initial data. Subsequently, starting at  $t \sim 40M$ , the SKS-runs show a second set of features, oscillations with amplitude  $\sim 2 \times 10^{-5}$  lasting about  $60M$ . The features of these oscillations are similar to each other even for runs with different spin  $\chi$ . Therefore, it is likely that these oscillations are caused by features in the initial data set *away* from the black holes.

In Fig. 4.6, curves of  $M_{irr}(t)$  are shown at different spins, at constant  $D = 15M$ , with Conformally flat initial data in the top panel, and SKS initial data in the bottom panel.

There is a clear qualitative between the CF and SKS curves. The CF data evidently forms a increasing sequence of  $\delta_M$  with  $\chi$ , and  $\delta_M$  is clearly well-defined in each case. However, the SKS data exhibits oscillatory behaviour that is relatively spin independent, and there is not a clear way to define  $\delta_M$ . The scale of the oscillations is on the order of  $10^{-5}$ . Our conclusion is that these are numerical oscillations and the contribution from junk radiation is not directly measurable, and we do not seek to characterize their parameter space dependence any further.

Figures 4.7 and 4.8 show convergence tests for one of the spin-values shown in Fig. 4.6. ( $D = 15M$ ,  $\chi = 0.3$ ). The top panels of Figs. 4.7 and 4.8 show  $M_{\text{irr}}(t)$  of one black hole computed at different numerical resolutions, and the bottom panels show differences in  $M_{\text{irr}}(t)$  computed at neighbouring resolutions. Note that our parameter space studies presented in Sec. 4.6 were usually performed on resolution “N3”; we have run “N4” only for select cases to test convergence. The CF initial data shows rapid convergence and the features in the upper panel of Fig. 4.6 are well resolved. For the SKS data, Fig. 4.8 indicates convergence, albeit much more slowly.

The magnitude of the change of  $M_{\text{irr}}(t)$  is much smaller for SKS initial data than for CF initial data ( $\sim 10^{-5}$  vs.  $\sim 5 \times 10^{-4}$ ). The changes in  $M_{\text{irr}}(t)$  for SKS initial data approach our numerical truncation error, and are furthermore ambiguous due to the extra features apparent in Fig. 4.6. Therefore, we shall not attempt to quantify them in detail, beyond giving upper bounds of the change on  $M_{\text{irr}}$  for SKS data.

### Spin Decrease

Our third and final quantification of junk radiation comes from the black hole’s spin  $S(t)$ . At early times in each simulation –seen in Fig. 4.9, the spin of each black hole decreases and oscillates rapidly. Eventually, at some time  $t_{eq}$ , the spin reaches some approximately constant value, which is lower than the initial spin,  $S(0)$ . This effect can be interpreted as angular momentum being carried away from the system by junk radiation. Note that

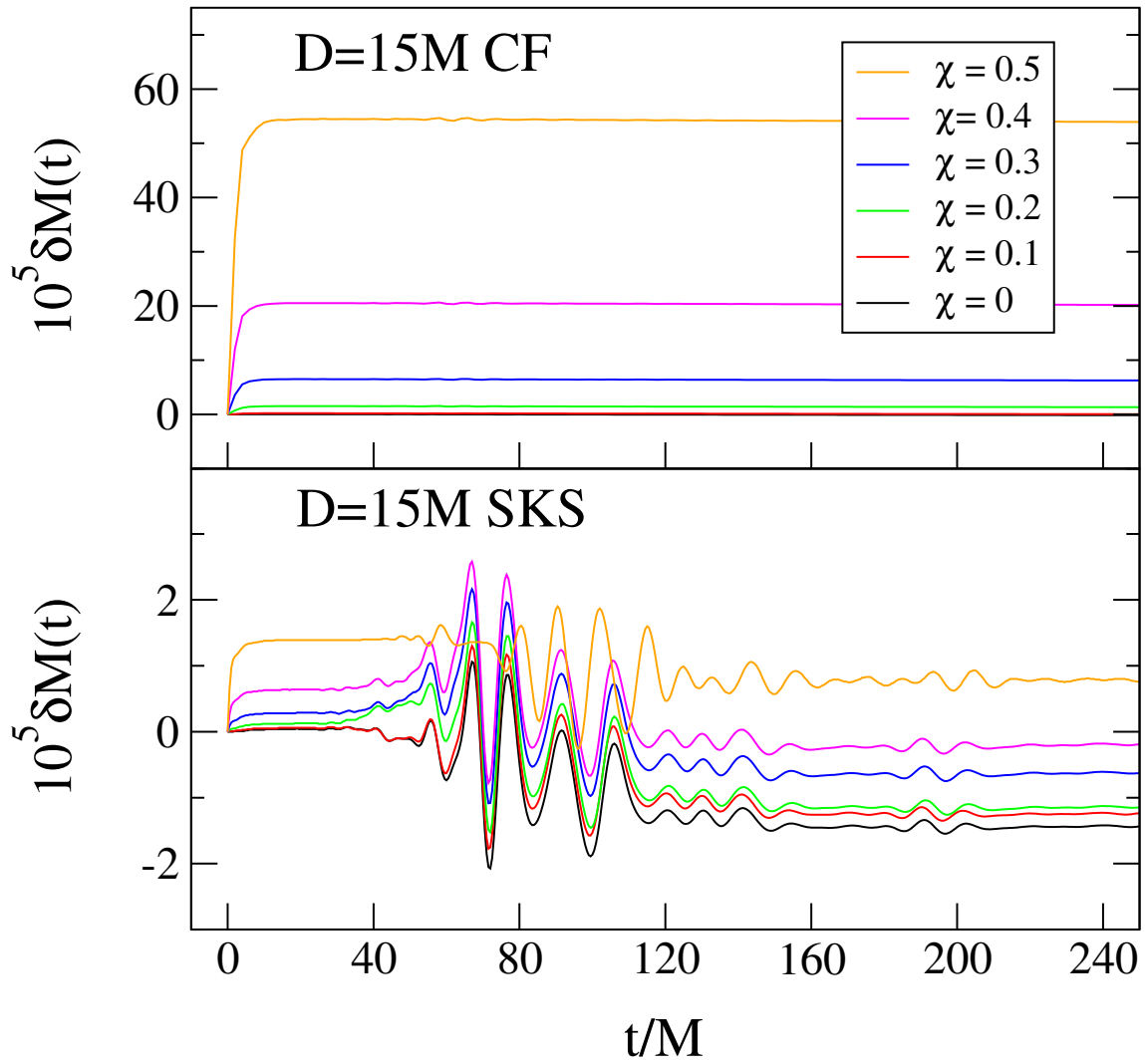


Figure 4.6: Normalized irreducible mass curves for CF data (top panel) and SKS data (bottom panel) for all of the different spins in the covered parameter space and  $D = 15M$  remaining constant.

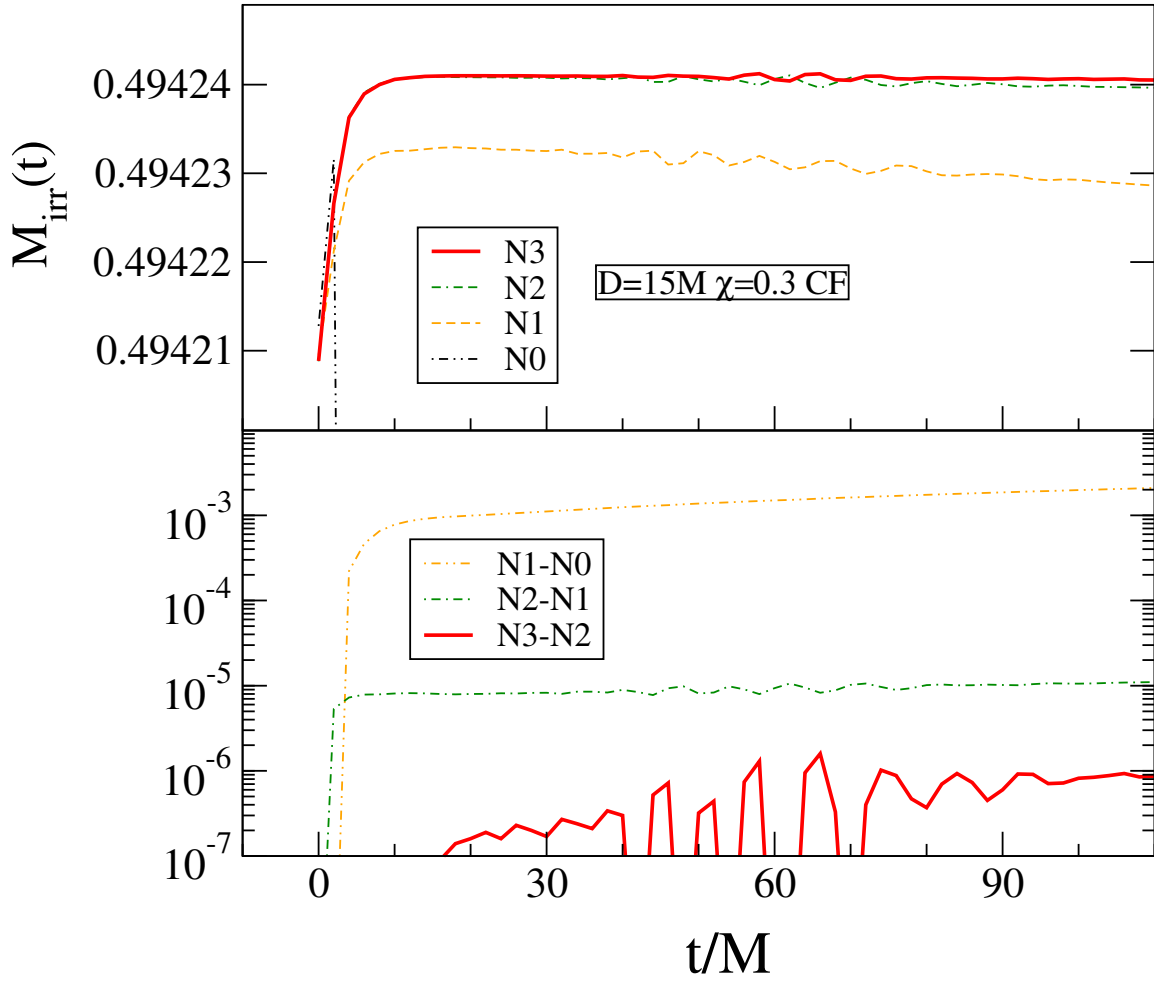


Figure 4.7: Convergence test of  $M_{irr}(t)$  for CF initial data in the case  $D15 = M$ ,  $\chi = 0.3$ . The top panel shows  $M_{irr}(t)$  at different resolutions, and the bottom panel shows the difference between consecutive resolutions.



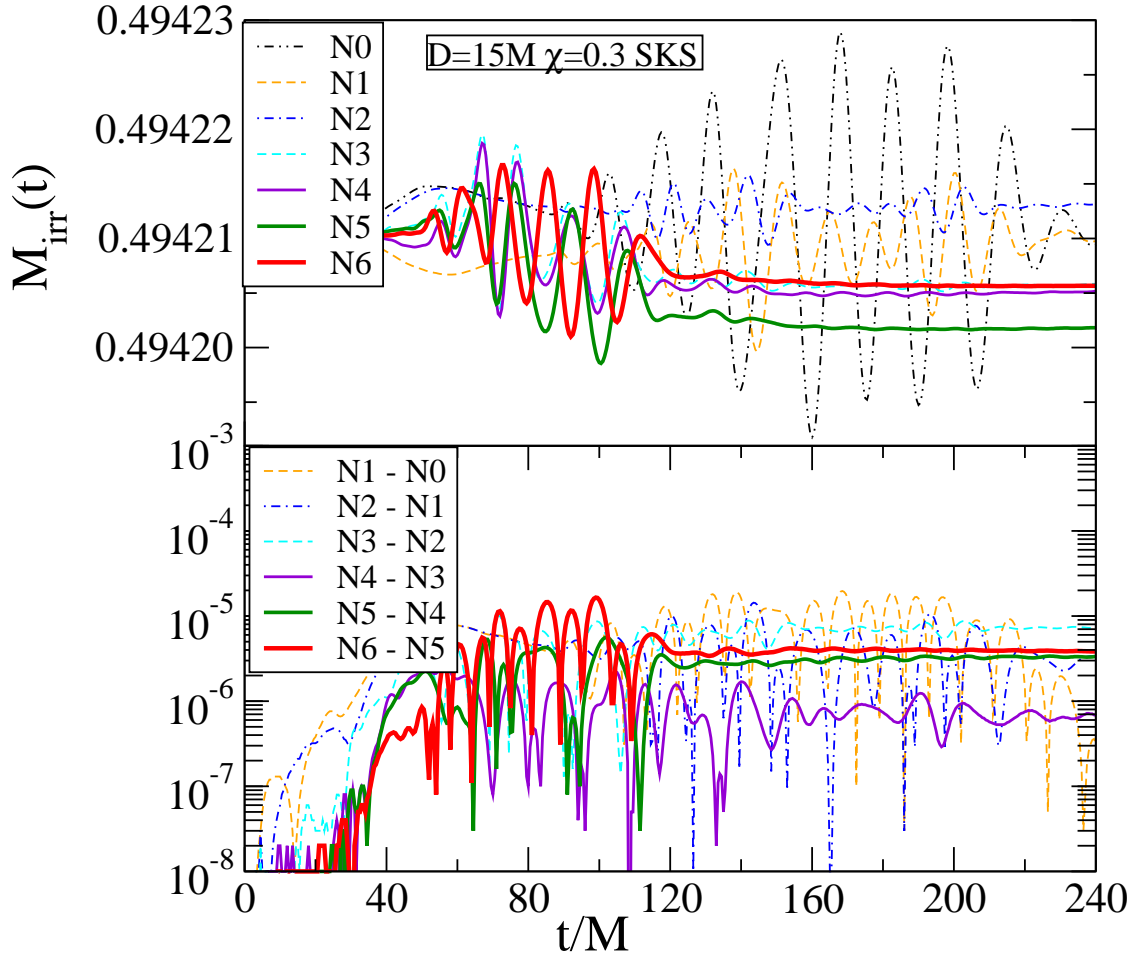


Figure 4.8: Convergence test of  $M_{irr}(t)$  for SKS initial data in the case  $D15 = M$ ,  $\chi = 0.3$ . The top panel shows  $M_{irr}(t)$  at different resolutions, and the bottom panel shows the difference between consecutive resolutions.

we use the dimension-ful quasi-local angular momentum, measured with approximate Killing vectors as described in Lovelace et al. (2008). We use  $S$  rather than  $\chi = S/M^2$  to de-couple the change in spin from the change in mass.

Analogous to  $\delta M(t)$ , we can define the parameter  $\delta S(t)$  as the fractional spin decrease of the black hole:

$$\delta S(t) = \frac{S(t)}{S(0)} - 1 \quad (4.22)$$

and the equilibrium parameter  $\delta S_{eq} = \delta S(t_{eq})$ , where  $t_{eq}$  the time when  $\delta S(t)$  has reached some nearly constant value. In practice, we compute  $\delta S_{eq}$  as the average value of  $\delta S(t)$  over some suitable interval around  $t_{eq}$ .

Analogous to Figs. 4.7 and 4.8, Figs. 4.10 and 4.11 demonstrate convergence tests for  $\delta S(t)$ , again for the case  $D = 15M, \chi = 0.3$ . Similar to what was seen in the convergence test for  $M_{irr}(t)$ , the CF data convergences rapidly, while we see no clear convergence in the SKS data going up to N6.

## 4.6 Results

### 4.6.1 Energy in Junk Radiation

Figure 4.12 shows the energy in the pulse of junk radiation, for all of our runs, as a function of spin. It is clear that within the uncertainty of our simulations,  $E_J$  has virtually no dependence on the spins of the black holes. The only exception may be that for conformally flat data,  $E_J$  seems to increase as  $\chi \rightarrow 0.5$ . This is most visible in the  $D = 12M$  case. Perhaps the dependence of  $E_J$  on  $\chi$  could become important for  $\chi > 0.5$  if this trend continues.

Because, as we've shown in Fig. 4.12, there is virtually no dependence of  $E_J$  on  $\chi$ , in looking at the dependence of  $E_J$  on  $D$ , we can use a fixed  $\chi$ ; we use  $\chi = 0$ . Figure 4.13 shows  $E_J$  as a function of  $D$  for CF and SKS data. Both cases are good fits to power

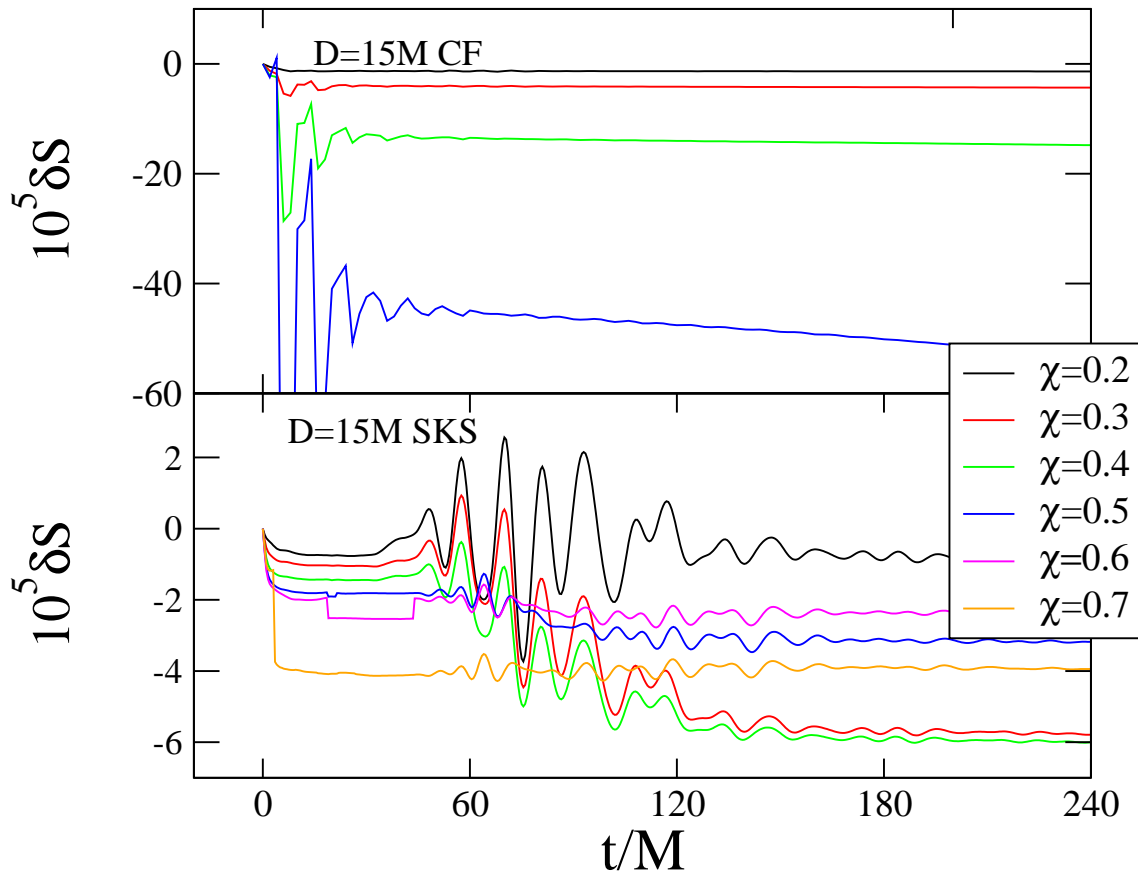


Figure 4.9: Fractional change in spin relative to  $t = 0$ ,  $\delta S = S(t)/S(t = 0) - 1$ . The top panel shows conformally flat initial data and the bottom panel SKS data (note the different scale). All simulations at distance  $D = 15M$ .

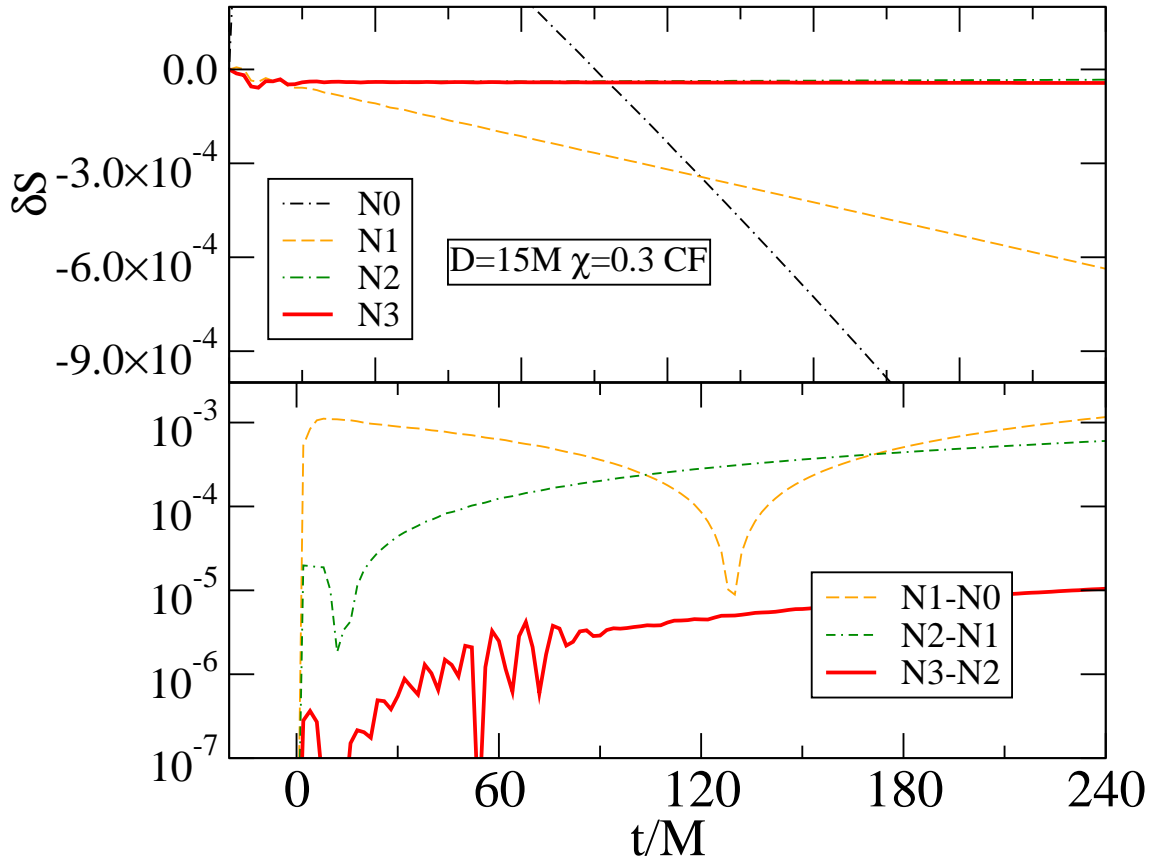


Figure 4.10: Convergence test of  $\delta S(t)$  for CF initial data in the case  $D = 15M$ ,  $\chi = 0.3$ . The top panel shows  $\delta S(t)$  at different resolutions and the bottom panel shows the differences between consecutive resolutions

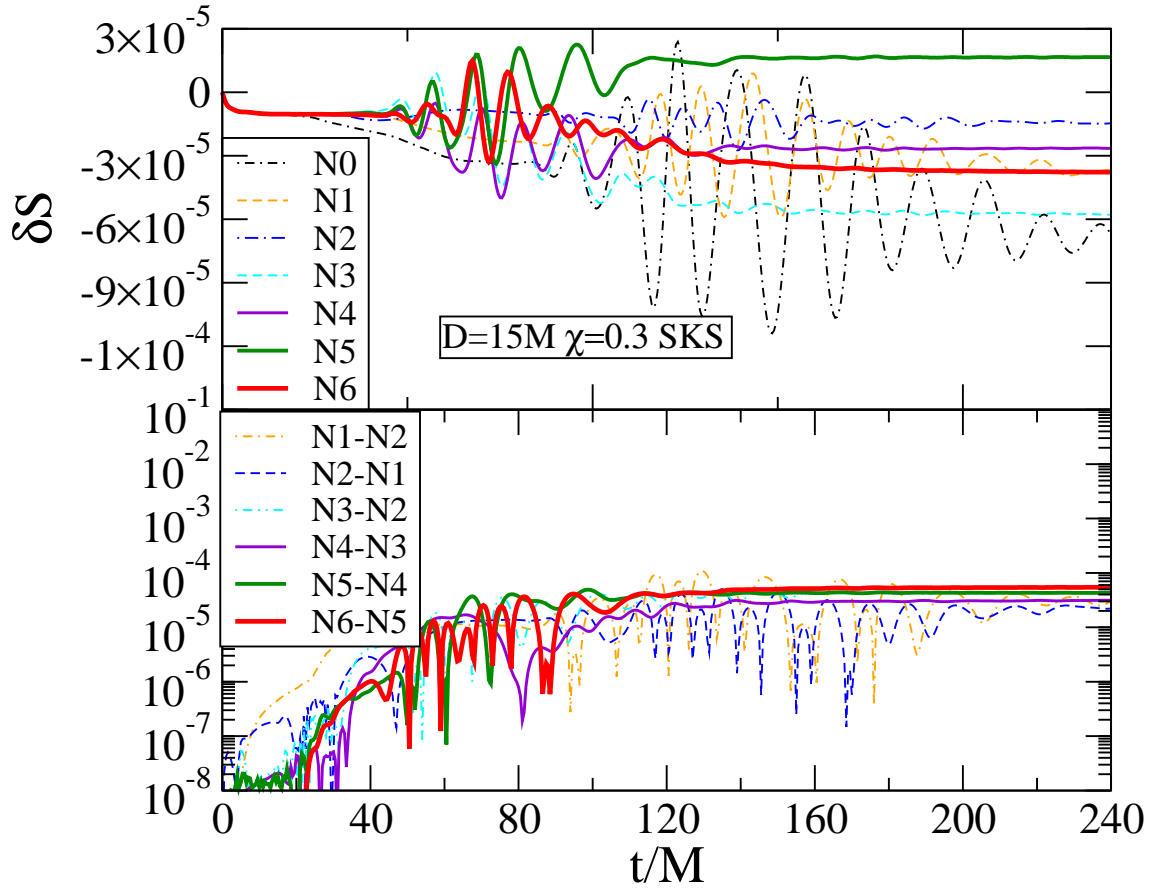


Figure 4.11: Convergence test of  $\delta S(t)$  for SKS initial data in the case  $D = 15M$ ,  $\chi = 0.3$ . The top panel shows  $\delta S(t)$  at different resolutions and the bottom panel shows the differences between consecutive resolutions

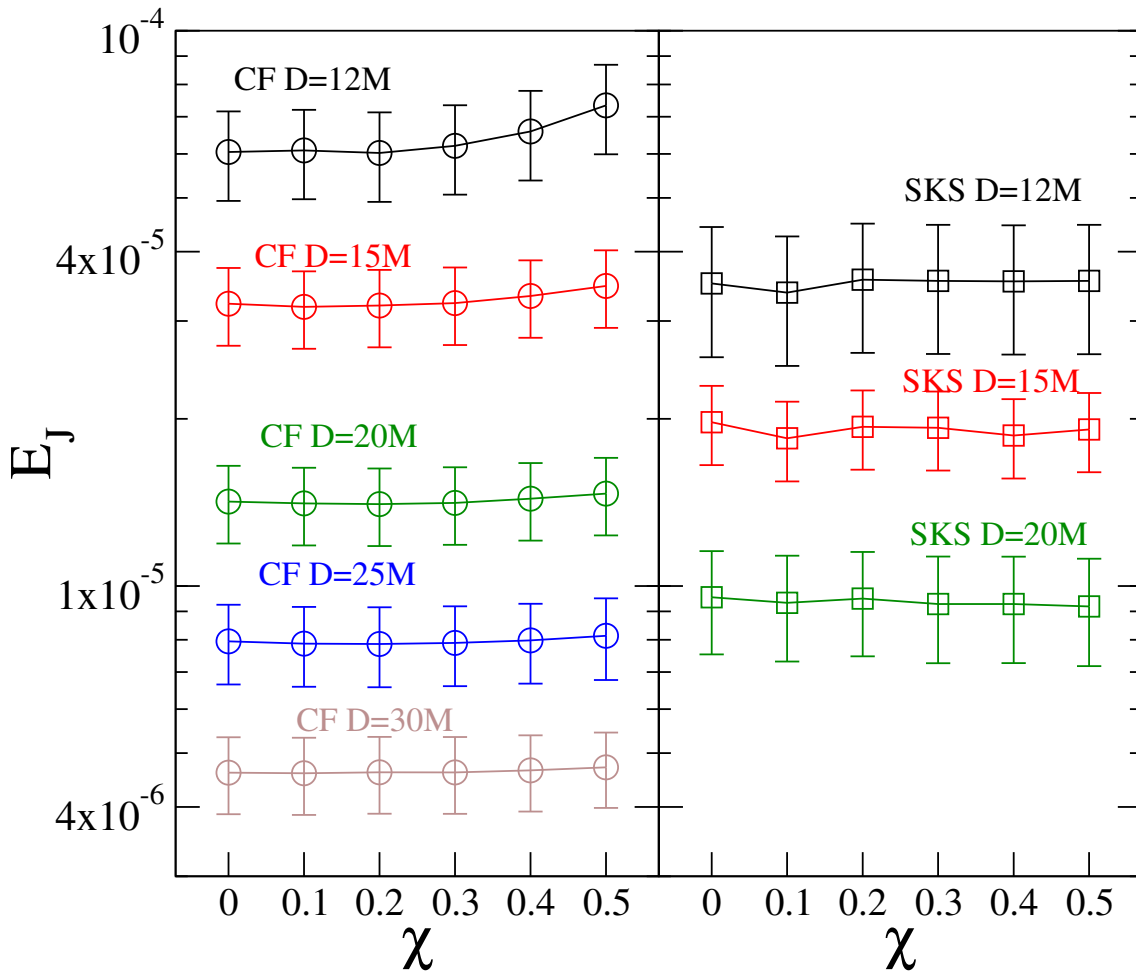


Figure 4.12: Energy in junk radiation as a function of  $\chi$  at various initial separations, for conformally flat initial data (left panel) and SKS initial data (right panel). Within the uncertainty limit, there is virtually no dependence of  $E_J$  on  $\chi$

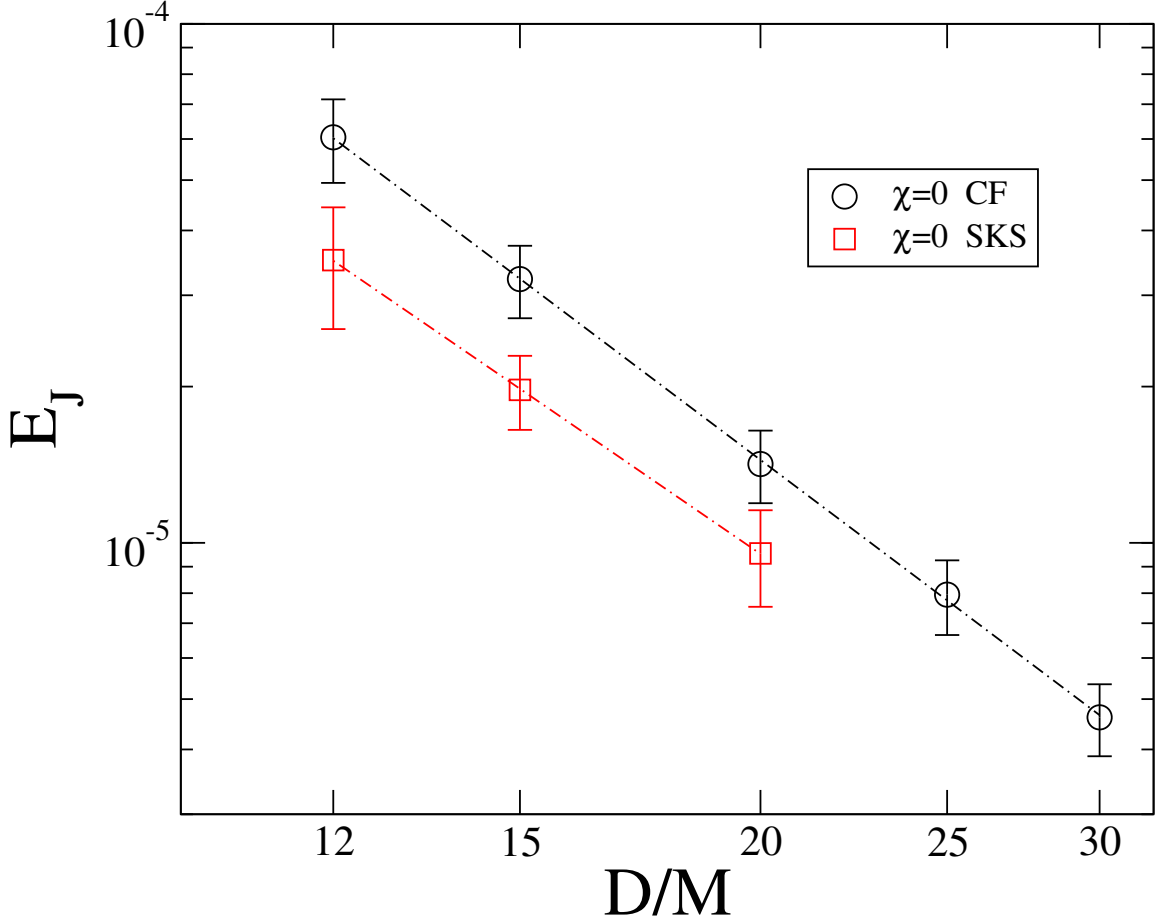


Figure 4.13: Log-log plot of the energy in junk radiation as a function of initial separation for binaries where  $\chi = 0$ . The black circles and red squares denote conformally flat and SKS initial data, respectively. The dotted lines are power law fits, with indices of  $\sim -2.79$  and  $\sim -2.55$  respectively.

laws. For conformally flat data,

$$E_J^{\text{CF}} \sim 0.06225 \left( \frac{D}{M} \right)^{-2.7933}. \quad (4.23)$$

and for SKS data

$$E_J^{\text{SKS}} \sim 0.019576 \left( \frac{D}{M} \right)^{-2.5464}, \quad (4.24)$$

however the latter is just a fit to three data points.

### 4.6.2 Mass Increase

As discussed earlier, we only attempt to quantify the transient quantities for CF data, due to the non-convergence of SKS data. We begin by looking at the dependence of  $\delta M_{eq}$  on separation. In Fig. 4.14, we plot it for curves of constant  $\chi^2$ .

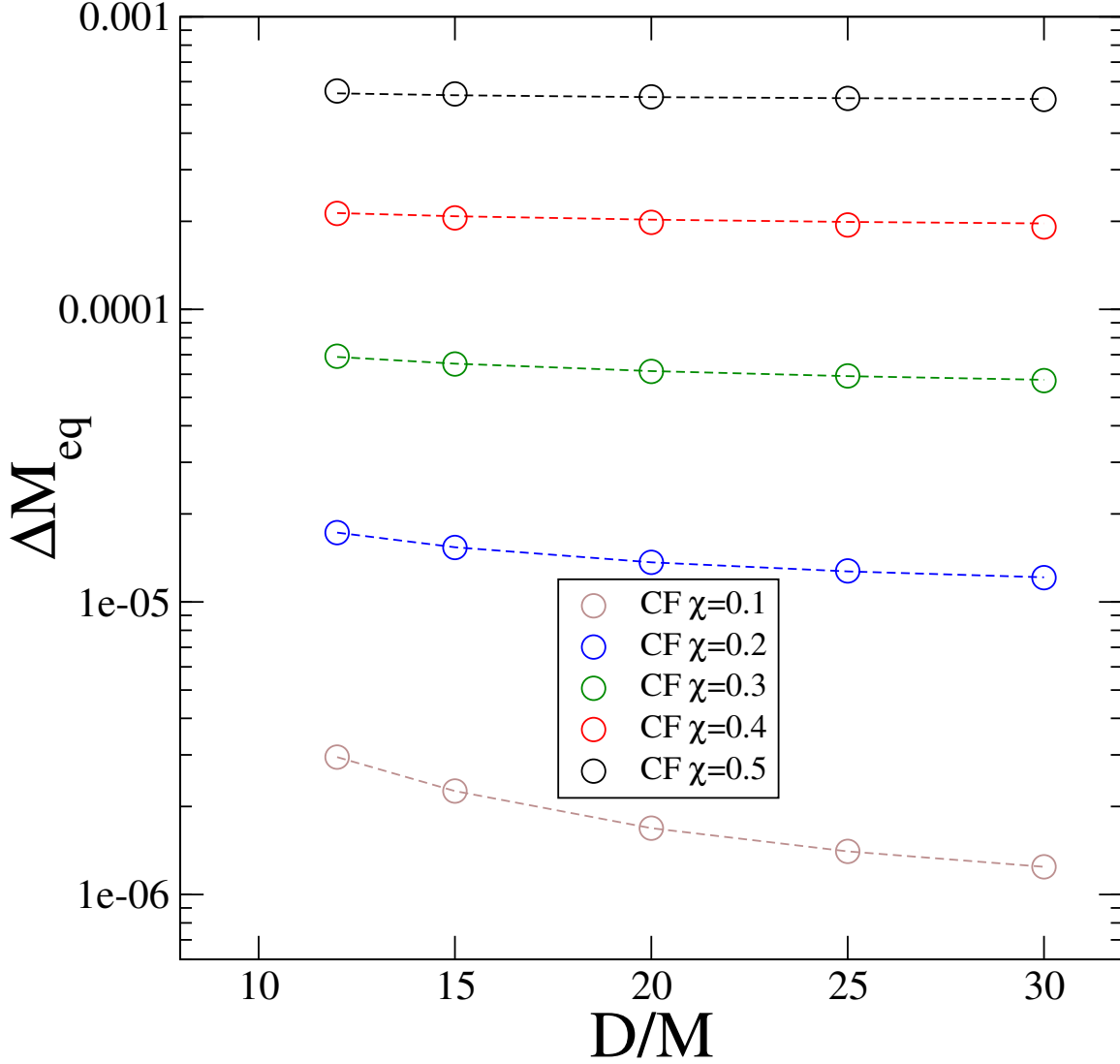


Figure 4.14:  $\delta M_{eq}$  as a function of initial separation for CF initial data. The dotted lines are the best fits to a power law plus a constant offset.

The data are nearly independent of distance at high spin, while there is a clear

---

<sup>2</sup>we omit  $\chi = 0$  because the data is too noisy



dependence at lower spin. In each case, we fit the data to a power law plus a constant offset. The fits are

$$\begin{aligned}
\delta M_{\text{eq}}^{\chi=0.1} &= 0.000170 (D/M)^{-1.76} + 8.194 \times 10^{-7} \\
\delta M_{\text{eq}}^{\chi=0.2} &= 0.000209 (D/M)^{-1.36} + 1.007 \times 10^{-5} \\
\delta M_{\text{eq}}^{\chi=0.3} &= 0.000146 (D/M)^{-0.75} + 4.60 \times 10^{-5} \\
\delta M_{\text{eq}}^{\chi=0.4} &= 0.000262 (D/M)^{-0.87} + 1.83 \times 10^{-4} \\
\delta M_{\text{eq}}^{\chi=0.5} &= 0.000470 (D/M)^{-0.99} + 5.08 \times 10^{-4}
\end{aligned}$$

In Fig. 4.15, the dependence of  $\delta M_{\text{eq}}$  is shown. In general we find that  $\delta M_{\text{eq}}$  grows rapidly with  $\chi$  and the dependence is nearly exponential at each separation.

### 4.6.3 Spin Decrease

As with the mass increase, we only attempt to calculate  $\delta S_{\text{eq}}$  for CF data, as it was found to not be convergent for SKS data. In Fig. 4.16 we plot  $\delta S_{\text{eq}}$  vs.  $D$  for curves of constant  $\chi^3$ . The data are similar to those in Fig. 4.14, although there is a stronger dependence on separation.

In each case, we fit the data to a power law plus a constant offset. The fits are

$$\begin{aligned}
\delta S_{\text{eq}}^{\chi=0.2} &= 0.000154 (D/M)^{-0.966} + 5.836 \times 10^{-8} \\
\delta S_{\text{eq}}^{\chi=0.3} &= 0.000340 (D/M)^{-0.836} + 6.025 \times 10^{-6} \\
\delta S_{\text{eq}}^{\chi=0.4} &= 0.00136 (D/M)^{-1.189} + 8.348 \times 10^{-5} \\
\delta S_{\text{eq}}^{\chi=0.5} &= 0.00261 (D/M)^{-1.133} + 3.445 \times 10^{-4}
\end{aligned}$$

In figure 4.17,  $\delta S_{\text{eq}}$  is plotted as a function of  $\chi$ , at different separations. In each case, the data is a good fit to an exponential; at  $D = 15M$ ,

$$\delta S_{\text{eq}} \sim 1.563 \times 10^{-6} e^{11.546\chi} \quad (4.25)$$

---

<sup>3</sup>we omit  $\chi = 0$  because  $\delta S_{\text{eq}}$  is not well-defined, and we omit  $\chi = 0.1$  because the data is too noisy

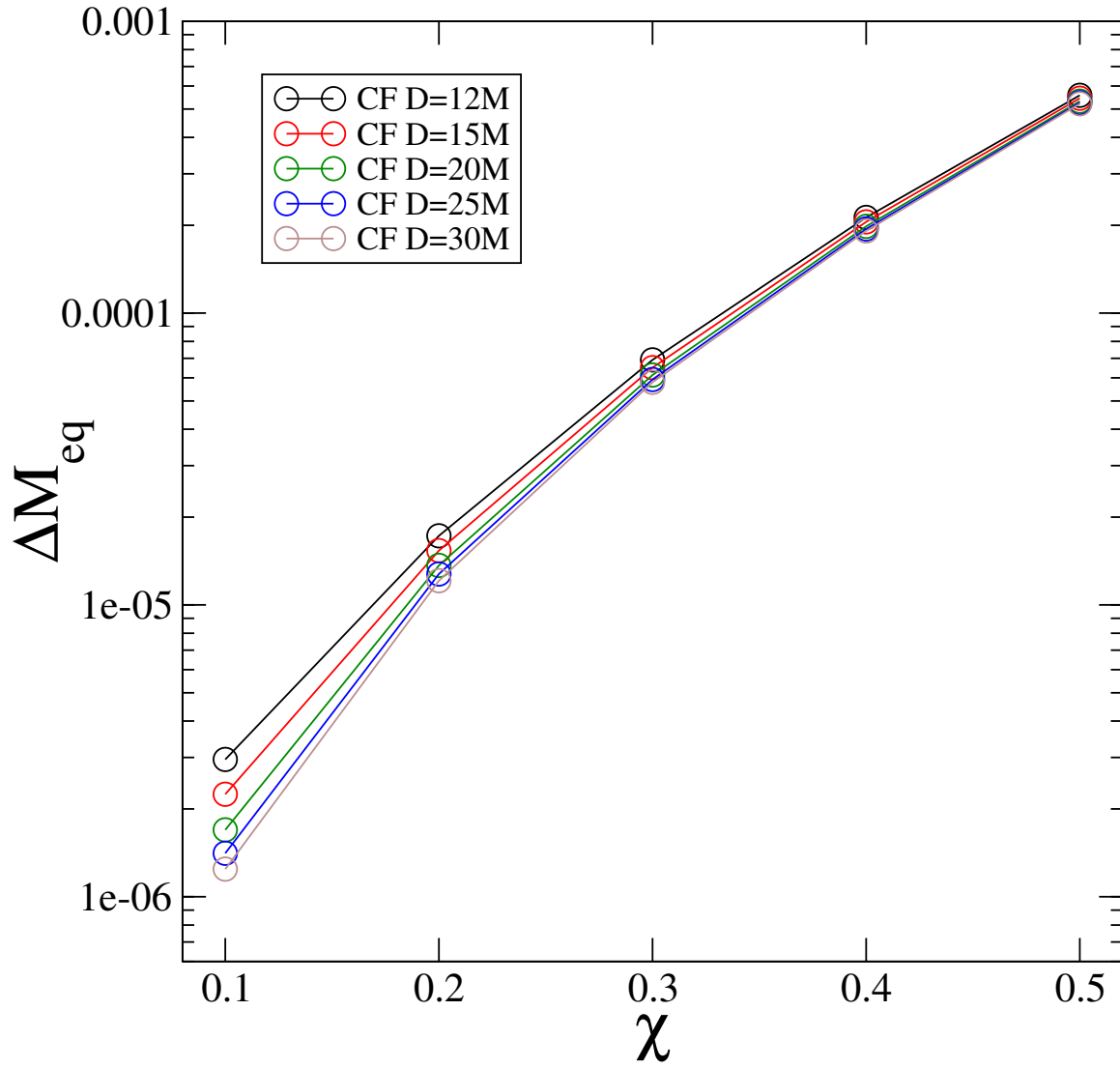


Figure 4.15:  $\delta M_{eq}$  as a function of black hole spin  $\chi$  for CF initial data, evaluated at each different initial separation.

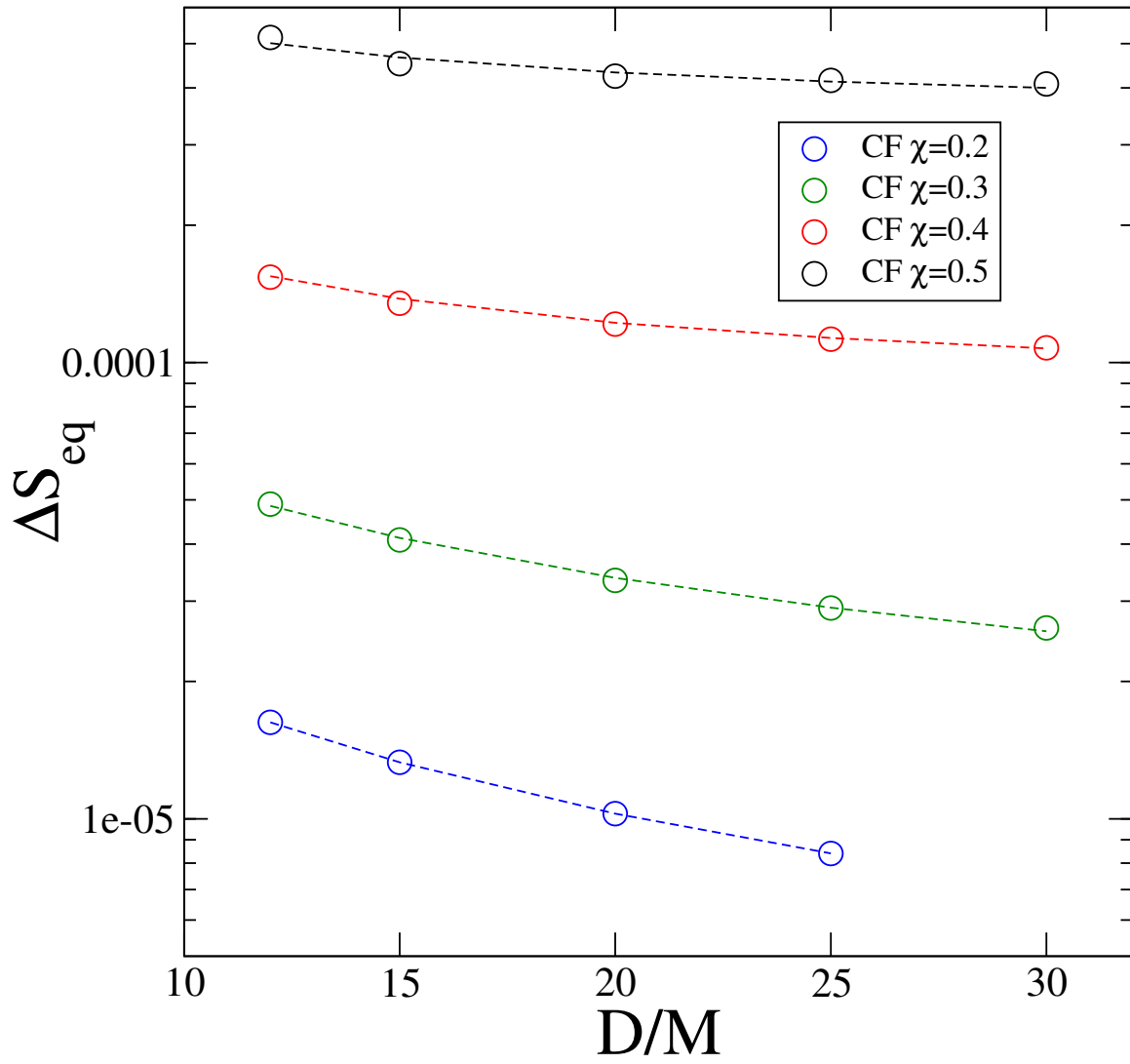


Figure 4.16:  $\delta S_{\text{eq}}$  vs.  $D$  for CF initial data. The dotted curves are the best fit power law plus constant offsets.

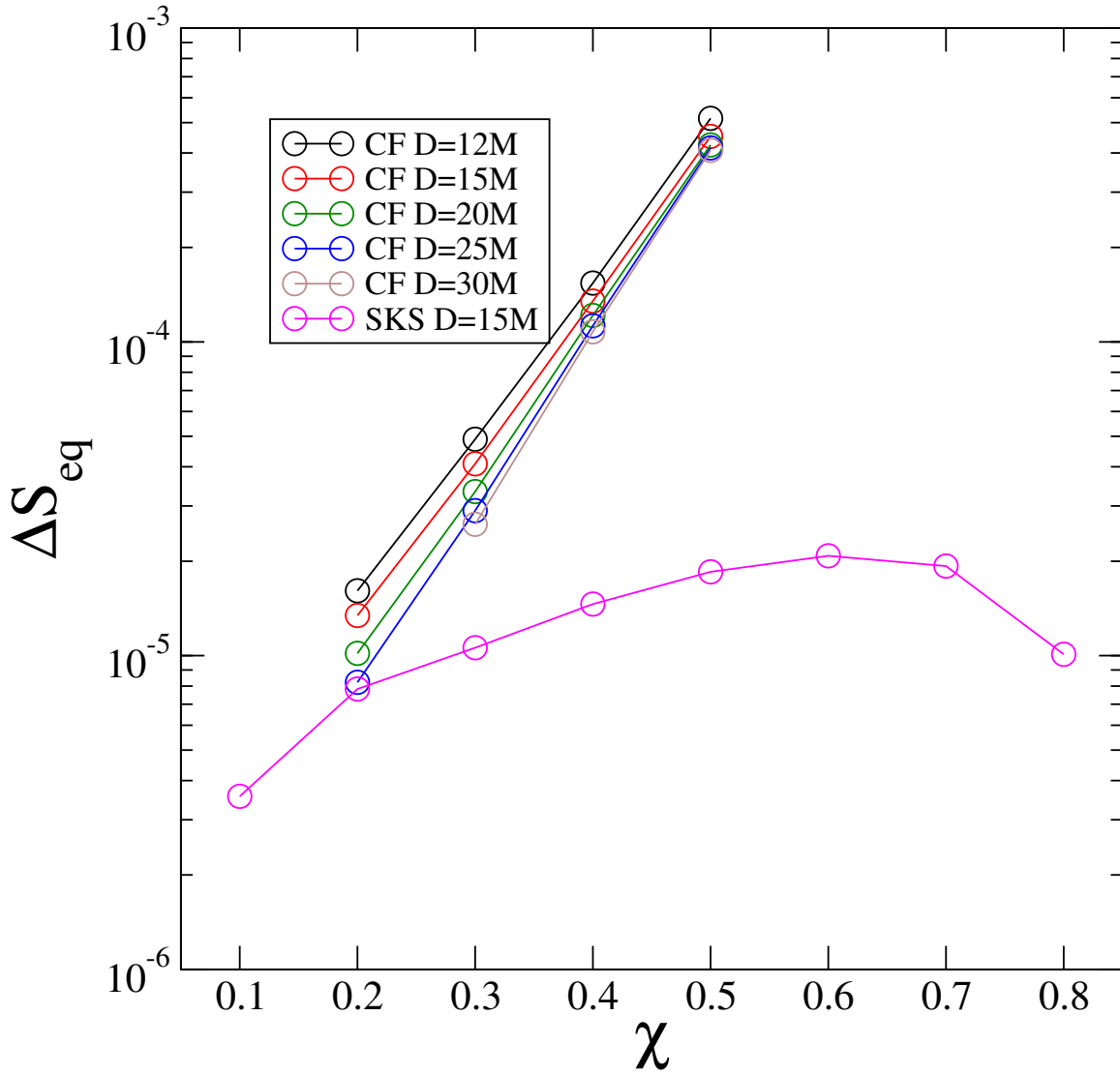


Figure 4.17: Semi-log plot of  $\delta S_{\text{eq}}$  as a function of  $\chi$  for CF data. The dotted lines are the best fit exponentials.

## 4.7 Summary

My Summary.

# Chapter 5

## Conclusions & Future Work

### 5.1 Conclusions

My Conclusions

### 5.2 Future Work and Directions

My Future Work and Directions.

# Bibliography

????, Simulating eXtreme Spacetimes, <http://www.black-holes.org/>

A. Harten, P. D. Lax, B. v. L. 1983, SIAM Rev., 25, 35

Aasi, J., et al. 2015, Class. Quant. Grav., 32, 074001

Abadie, J., et al. 2010a, Class. Quant. Grav., 27, 173001, arXiv:1003.2480

—. 2010b, Class. Quant. Grav., 27, 173001

Abbott, B. P., et al. 2016a, Phys. Rev. Lett., 116, 241103

—. 2016b, Phys. Rev. Lett., 116, 061102

Acernese, F., et al. 2006, Class. Quantum Grav., 23, S635

—. 2015, Class.Quant.Grav., 32, 024001

Agathos, M., Meidan, J., Pozzo, W. D., Li, T. G. F., Tompitak, M., Veitch, J., Vitale, S., & Broeck, C. V. D. 2015, ArXiv:1503.05405

Ajith, P. 2011, Phys. Rev. D, 84, 084037

Ansorg, M., Kleinwachter, A., & Meinel, R. 2003, Astron.Astrophys., 405, 711

Arnowitt, R., Deser, S., & Misner, C. W. 1962, in Gravitation: An Introduction to Current Research, ed. L. Witten (New York: Wiley), 227–265

- Ashtekar, A., Beetle, C., & Lewandowski, J. 2001, *Phys. Rev. D*, 64, 044016
- Ashtekar, A., & Krishnan, B. 2003, *Phys. Rev. D*, 68, 104030
- Baiotti, L., Damour, T., Giacomazzo, B., Nagar, A., & Rezzolla, L. 2010, *Phys. Rev. Lett.*, 105, 261101
- Baiotti, L., Damour, T., Giacomazzo, B., Nagar, A., & Rezzolla, L. 2011, *Phys. Rev. D*, 84, 024017
- Barish, B. C., & Weiss, R. 1999, *Phys. Today*, 52, 44
- Baumgarte, T. W., O’Murchadha, N., & Pfeiffer, H. P. 2007, *Phys. Rev. D*, 75, 044009
- Baumgarte, T. W., & Shapiro, S. L. 2009, *Phys.Rev.*, D80, 064009
- Benacquista, M. J., & Downing, J. M. 2013, *Living Rev.Rel.*, 16, 4
- Bernuzzi, S., Dietrich, T., Tichy, W., & Bruegmann, B. 2014, *Phys. Rev. D*, 89, 104021
- Bernuzzi, S., Nagar, A., Dietrich, T., & Damour, T. 2015, *Phys.Rev.Lett.*, 114, 161103
- Berti, E., et al. 2015
- Bildsten, L., & Cutler, C. 1992, *Astrophys. J.*, 400, 175
- Blanchet, L. 2006, *Living Rev.Rel.*, 9, 4
- Bode, T., Shoemaker, D., Herrmann, F., & Hinder, I. 2008, *Phys. Rev. D*, 77, 44027
- Boyle, M., Brown, D. A., Kidder, L. E., Mroué, A. H., Pfeiffer, H. P., Scheel, M. A., Cook, G. B., & Teukolsky, S. A. 2007, *Phys. Rev. D*, 76, 124038
- Boyle, M., Buonanno, A., Kidder, L. E., Mroué, A. H., Pan, Y., et al. 2008, *Phys. Rev. D*, 78, 104020
- Brown, D. A., Harry, I., Lundgren, A., & Nitz, A. H. 2012, *Phys.Rev.*, D86, 084017



- Brown, J. D., & York, J. W. 1993, *Phys. Rev. D*, 47, 1407
- Buchman, L. T., Pfeiffer, H. P., Scheel, M. A., & Szilágyi, B. 2012, *Phys. Rev. D*, 86, 084033
- Buonanno, A. 2007, in *Les Houches Summer School - Session 86: Particle Physics and Cosmology: The Fabric of Spacetime* Les Houches, France, July 31-August 25, 2006
- Buonanno, A., & Damour, T. 1999, *Phys. Rev. D*, 59, 084006
- Buonanno, A., Kidder, L. E., Mroué, A. H., Pfeiffer, H. P., & Taracchini, A. 2011, *Phys. Rev. D*, 83, 104034
- Caudill, M., Cook, G. B., Grigsby, J. D., & Pfeiffer, H. P. 2006, *Phys. Rev. D*, 74, 064011
- Chatziioannou, K., Yagi, K., Klein, A., Cornish, N., & Yunes, N. 2015
- Christodoulou, D. 1970, *Phys. Rev. Lett.*, 25, 1596
- Chu, T., Pfeiffer, H. P., & Scheel, M. A. 2009, *Phys. Rev. D*, 80, 124051
- Cook, G. B. 2002, *Phys. Rev. D*, 65, 084003
- Cook, G. B., & Pfeiffer, H. P. 2004, *Phys. Rev. D*, 70, 104016
- Cook, G. B., & Whiting, B. F. 2007, *Phys. Rev. D*, 76, 041501(R)
- Damour, T., Nagar, A., & Villain, L. 2012, *Phys. Rev. D*, 85, 123007
- Del Pozzo, W., Li, T. G. F., Agathos, M., Van Den Broeck, C., & Vitale, S. 2013, *Physical Review Letters*, 111, 071101
- Dietrich, T., Moldenhauer, N., Johnson-McDaniel, N. K., Bernuzzi, S., Markakis, C. M., Bruegmann, B., & Tichy, W. 2015
- Dimmelmeier, H., Stergioulas, N., & Font, J. A. 2006, *Mon.Not.Roy.Astron.Soc.*, 368, 1609

- Duez, M. D., Foucart, F., Kidder, L. E., Pfeiffer, H. P., Scheel, M. A., & Teukolsky, S. A. 2008, Phys. Rev. D, 78, 104015
- East, W. E., Paschalidis, V., & Pretorius, F. 2015
- East, W. E., Ramazanoglu, F. M., & Pretorius, F. 2012, Phys.Rev., D86, 104053
- Fan, X., & Hendry, M. 2015
- Foucart, F. 2012, Phys. Rev. D, 86, 124007
- Foucart, F., Duez, M. D., Kidder, L. E., Scheel, M. A., Szilágyi, B., & Teukolsky, S. A. 2012, Phys. Rev. D, 85, 044015
- Foucart, F., Duez, M. D., Kidder, L. E., & Teukolsky, S. A. 2011, Phys. Rev. D, 83, 024005
- Foucart, F., Kidder, L. E., Pfeiffer, H. P., & Teukolsky, S. A. 2008, Phys. Rev. D, 77, 124051
- Foucart, F., et al. 2013, Phys. Rev. D, 87, 084006
- Garat, A., & Price, R. H. 2000, Phys. Rev. D, 61, 124011
- Gold, R., Bernuzzi, S., Thierfelder, M., Brugmann, B., & Pretorius, F. 2012, Phys.Rev., D86, 121501
- Gourgoulhon, E. 2007, 3+1 Formalism and Bases of Numerical Relativity
- Gourgoulhon, E., Grandclément, P., Taniguchi, K., Marck, J.-A., & Bonazzola, S. 2001, Phys. Rev. D, 63, 64029
- Harry, G. M. 2010, Class.Quant.Grav., 27, 084006
- Hemberger, D. A., Scheel, M. A., Kidder, L. E., Szilágyi, B., Lovelace, G., Taylor, N. W., & Teukolsky, S. A. 2013, Class. Quantum Grav., 30, 115001

- Hinderer, T., Lackey, B. D., Lang, R. N., & Read, J. S. 2010, *Phys. Rev. D*, 81, 123016
- Hinderer, T., et al. 2016, *Phys. Rev. Lett.*, 116, 181101
- Hulse, R. A., & Taylor, J. H. 1975a, *Astrophys. J.*, 195, L51
- . 1975b, *The Astrophysical Journal*, 195, L51
- Jiang, G.-S., & Shu, C.-W. 1996, *Journal of Computational Physics*, 126, 202
- Joshi, B. C. 2013, *Int. J. Mod. Phys.*, D22, 1341008
- Kastaun, W., Galeazzi, F., Alic, D., Rezzolla, L., & Font, J. A. 2013, *Phys.Rev.*, D88, 021501
- Kidder, L. E., Scheel, M. A., Teukolsky, S. A., Carlson, E. D., & Cook, G. B. 2000, *Phys. Rev. D*, 62, 084032
- Kuroda, K., & the LCGT Collaboration. 2010, *Class. Quantum Grav.*, 27, 084004
- Lackey, B. D., Kyutoku, K., Shibata, M., Brady, P. R., & Friedman, J. L. 2012, *Phys. Rev. D*, 85, 044061
- Lee, W. H., Ramirez-Ruiz, E., & van de Ven, G. 2010, *ApJ*, 720, 953
- Lichnerowicz, A. 1944, *J. Math Pures et Appl.*, 23, 37
- Lindblom, L., Scheel, M. A., Kidder, L. E., Owen, R., & Rinne, O. 2006, *Class. Quantum Grav.*, 23, S447
- Liu, X.-D., Osher, S., & Chan, T. 1994, *Journal of Computational Physics*, 115, 200
- Lo, K.-W., & Lin, L.-M. 2011, *Astrophys.J.*, 728, 12
- Lorimer, D. R. 2008, *Living Reviews in Relativity*, 11, 8
- Lovelace, G. 2009, *Class. Quantum Grav.*, 26, 114002

- Lovelace, G., Boyle, M., Scheel, M. A., & Szilágyi, B. 2012, *Class. Quant. Grav.*, 29, 045003
- Lovelace, G., Duez, M. D., Foucart, F., Kidder, L. E., Pfeiffer, H. P., Scheel, M. A., & Szilágyi, B. 2013, *Class. Quantum Grav.*, 30, 135004
- Lovelace, G., Owen, R., Pfeiffer, H. P., & Chu, T. 2008, *Phys. Rev. D*, 78, 084017
- Lovelace, G., Scheel, M. A., & Szilágyi, B. 2011, *Phys. Rev. D*, 83, 024010
- Lyne, A., Burgay, M., Kramer, M., Possenti, A., Manchester, R., et al. 2004, *Science*, 303, 1153
- M. A. Scheel, M. Boyle, T. Chu, L. E. Kidder, K. D. Matthews and H. P. Pfeiffer. 2009, *Phys. Rev. D*, 79, 024003
- Marronetti, P., & Matzner, R. A. 2000, *Phys. Rev. Lett.*, 85, 5500
- Marronetti, P., & Shapiro, S. L. 2003, *Phys.Rev.*, D68, 104024
- Matsushima, T., & Marcus, P. S. ????, *J. Comput. Phys.*, 120, 365
- Matzner, R. A., Huq, M. F., & Shoemaker, D. 1998, *Phys. Rev. D*, 59, 024015
- Metzger, B. D., & Berger, E. 2012, *Astrophys. J.*, 746, 48
- Muhlberger, C. D., Nouri, F. H., Duez, M. D., Foucart, F., Kidder, L. E., et al. 2014, *Phys. Rev. D*, 90, 104014
- Murchadha, N. Ó., & York, Jr., J. W. 1974, *Phys. Rev. D*, 10, 428
- Ossokine, S., Boyle, M., Kidder, L. E., Pfeiffer, H. P., Scheel, M. A., & Szilágyi, B. 2015
- Ossokine, S., Kidder, L. E., & Pfeiffer, H. P. 2013, *Phys. Rev.*, D88, 084031
- Owen, R. 2007, PhD thesis, California Institute of Technology

- Peters, P. C. 1964, *Phys. Rev.*, 136, B1224
- Peters, P. C., & Mathews, J. 1963, *Phys. Rev.*, 131, 435
- Pfeiffer, H. P., Brown, D. A., Kidder, L. E., Lindblom, L., Lovelace, G., & Scheel, M. A. 2007, *Class. Quantum Grav.*, 24, S59
- Pfeiffer, H. P., Cook, G. B., & Teukolsky, S. A. 2002, *Phys. Rev. D*, 66, 024047
- Pfeiffer, H. P., Kidder, L. E., Scheel, M. A., & Teukolsky, S. A. 2003, *Comput. Phys. Commun.*, 152, 253
- Pfeiffer, H. P., & York, J. W. 2003, *Phys. Rev. D*, 67, 044022
- Pfeiffer, H. P., & York Jr., J. W. 2005, *Phys. Rev. Lett.*, 95, 091101
- Postnov, K. A., & Yungelson, L. R. 2014, *Living Rev. Rel.*, 17, 3
- Pretorius, F. 2005, *Phys. Rev. Lett.*, 95, 121101
- . 2006, *Class. Quantum Grav.*, 23, S529
- Read, J. S., Markakis, C., Shibata, M., Uryū, K., Creighton, J. D. E., & Friedman, J. L. 2009, *Phys. Rev. D*, 79, 124033
- Rezzolla, L., Baiotti, L., Giacomazzo, B., Link, D., & Font, J. A. 2010, *Class. Quant. Grav.*, 27, 114105
- Rieth, R. 1997, in *Mathematics of Gravitation. Part II. Gravitational Wave Detection*, ed. A. Królak (Polish Academy of Sciences, Institute of Mathematics, Warsaw), 71–74
- Scheel, M. A., Giesler, M., Hemberger, D. A., Lovelace, G., Kuper, K., Boyle, M., Szilágyi, B., & Kidder, L. E. 2015, *Classical and Quantum Gravity*, 32, 105009
- Scheel, M. A., Pfeiffer, H. P., Lindblom, L., Kidder, L. E., Rinne, O., & Teukolsky, S. A. 2006, *Phys. Rev. D*, 74, 104006

- Shibata, M. 1998, *Phys.Rev.*, D58, 024012
- Shibata, M., & Uryu, K. 2000, *Phys. Rev. D*, 61, 064001
- Somiya, K., & the KAGRA Collaboration. 2012, *Class. Quantum Grav.*, 29, 124007
- Szilágyi, B. 2014, *Int.J.Mod.Phys.*, D23, 1430014
- Szilágyi, B., Lindblom, L., & Scheel, M. A. 2009, *Phys. Rev. D*, 80, 124010
- Tacik, N., et al. 2015, *Phys. Rev.*, D92, 124012
- Taniguchi, K., Baumgarte, T. W., Faber, J. A., & Shapiro, S. L. 2006, *Phys. Rev. D*, 74, 041502
- . 2007, *Phys. Rev. D*, 75, 084005
- Teukolsky, S. A. 1998, *Astrophys.J.*, 504, 442
- The Virgo Collaboration. 2010, *Advanced Virgo Baseline Design*, vIR027A09
- Tichy, W. 2011, *Phys.Rev.*, D84, 024041
- . 2012, *Phys.Rev.*, D86, 064024
- Tsatsin, P., & Marronetti, P. 2013
- Tsokaros, A., Uryū, K., & Rezzolla, L. 2015, *Phys. Rev.*, D91, 104030
- Verkley, W. T. M. 1997, *Journal of Computational Physics*, 136, 100
- Walsh, D. M. 2007, *Class. Quantum Grav.*, 24, 1911
- Worley, A., Krastev, P. G., & Li, B.-A. 2008
- York, J. W. 1999, *Phys. Rev. Lett.*, 82, 1350
- York, Jr., J. W. 1979, in *Sources of Gravitational Radiation*, ed. L. L. Smarr (Cambridge, England: Cambridge University Press), 83–126